CONTROLLABLE GROWTH OF POROUS STRUCTURES FROM

CO-CONTINUOUS POLYMER BLEND

A Dissertation

Presented to

The Academic Faculty

by

Wei Zhang

In Partial Fulfillment

of the Requirements for the Degree

Ph.D. in the

School of Materials Science and Engineering

Georgia Institute of Technology

May, 2011

CONTROLLABLE GROWTH OF POROUS STRUCTURES FROM

CO-CONTINUOUS POLYMER BLEND

Approved by:

Dr. Donggang Yao, Advisor
School of Materials Science & Engineering
Georgia Institute of Technology

Dr. Anselm Griffin
School of Materials Science & Engineering
Georgia Institute of Technology

Dr. Youjiang Wang
School of Materials Science & Engineering
Georgia Institute of Technology

Dr. Jack Zhou, Co-advisor
Department of Mechanical Engineering
and Mechanics
Drexel University

Dr. Karl Jacob
School of Materials Science and
Engineering
Georgia Institute of Technology

Date Approved: March 10, 2011

ACKNOWLEDGEMENTS

I am deeply indebted to my advisors, Dr. Donggang Yao and Dr. Jack Zhou, for their careful guidance, constructive criticism, and consistent support throughout my PhD study at Georgia Tech.

I would thank Dr. Anselm Griffin, Dr. Karl Jacob, and Dr. Youjiang Wang for serving in the dissertation committee and providing valuable comments and advices.

I would like to thank Dr. Meisha L. Shofner and her research group at Georgia Tech for using their batch mixer. I also want to thank faculty and staff members at School of Polymer, Textile, and Fiber Engineering (currently part of School of Materials Science and Engineering) for their support.

I sincerely cherish the contributions from Ms. Min Li on many aspects of my dissertation research, especially on projects related to compression molding and hot embossing with in-mold annealing of co-continuous polymer blend.

I want to thank my group members-Dr. Pratapkumar Nagarajan, Dr. Ruihua Li, Dr. Jun Jia, Dr. Ramasubramani Kuduva-Raman-Thanumoorthy, Sarang Deodhar, Kathryn Abbott, Ian Winterss, Tom Wyatt, Yutong Pan, and Pan Dai-for their help and encouraging discussions during the Ph.D. study.

I would like to thank my collaborators at Drexel University: Dr. Peter I. Lelkes, Dr. Qingwei Zhang, Fubo Kung, Sean Devlin, and Jephte Augustin.

I also deeply thank my friends at Georgia Tech for their trust, support and dedication over these years.

Last but most certainly not the least, I want to acknowledge National Science

Foundation for financial support of this research.

TABLE OF CONTENT

LIST OF TABLES

LIST OF FIGURES

SUMMARY

Because of the large accessible surface area, microporous materials have been employed in various fields such as tissue engineering, catalytic reaction, Li-ion battery, filtration, and others. The rapid progress in these related fields brings numerous opportunities and also many technical challenges to this type of materials. Among these technical challenges, creation of organized porous material was chosen to be the main topic of this PhD research as it was expected to have a broad impact on many technical applications as well as to provide scientific insights into fundamental processing-structure relations. To enable controllable generation of porous structures, a set of new fabrication techniques utilizing the annealing kinetics of co-continuous polymer blends were proposed and investigated.

As the first step towards the creation of an organized porous material, a new technique based on regulating the thermal boundary conditions to controllably grow gradient porous structures was developed. In this technique, specially designed thermal boundaries were used to generate a well-defined temperature field inside a co-continuous polymer blend with fine phase structure. Because of the temperature dependency of zero-shear viscosity and its influence on phase coarsening rate, a graded phase size distribution was generated by this temperature field. After one component was selectively dissolved, a gradient porous structure was produced. To demonstrate the versatility of this technique, three different gradient porous structures were created.

After the effectiveness of thermal boundary condition in developing organized

porous materials was verified, the possibility of utilizing kinematic and dynamic boundary conditions to obtain extra controllability was investigated. Two types of kinematic boundary conditions, no-slip wall and 1D hard wall confinement were tested separately. It was found that no-slip wall could greatly slow down the phase coarsening rate of the nearby polymer blend. When a no-slip wall and a fully slip wall were applied at each side of a molten co-continuous blend, a pore size gradient was generated in the direction perpendicular to the wall surface with smaller pores near the no-slip wall. One directional hard wall confinement formed by a pair of fully slip parallel walls led to the formation of an aligned phase structure oriented in the vertical direction to the walls. Experiments regarding the effect of dynamic boundary condition were conducted by imposing different chemical potentials at the surface of molten blend. Fully dense surface and completely open surface were generated when high energy metallic surface and low energy PTFE (polytetrafluoroethylene) were applied respectively.

In addition to the creation of polymeric porous materials, the generation of organized porous nanocomposite with high nanoparticle loading was also explored to incorporate unique properties seldom appearing in polymeric materials. The influence of blending procedure was first studied to secure the required co-continuous phase morphology for making porous nanocomposite. It was found that one had to simultaneously introduce all ingredients for mixing to minimize the change in viscosity ratio and produce the initial co-continuous structures. Because of the high nanoparticle loading, most of the formed pores were crowded with aggregates from particles

originally located in the dissolved phase. To obtain the desired high permeability, a technique based on small strain oscillation was developed to facilitate rapid migration of these nanoparticles out of the sacrificial component. The effectiveness of this method was confirmed by a parametric experimental study. In addition, it was found that the migration rate of the nanoparticle could be predicted by combining the Einstein-Stokes diffusion model with the Cox-Merz rule.

To create porous material with desired geometries for different application needs, a new molding technique capable of creating precise micropatterned porous structures was developed and examined. In this new technique, hot embossing and in-mold quiescent annealing were applied successively to a co-continuous polymer blend to pattern the blend into expected geometries and in the same time produce the desired bulk microstructures. The effectiveness of this molding protocol was confirmed by experimental results in which devices with different micropatterns, average pore sizes, pore size distributions, and pore alignments were created. For cases where fully open surface is required, a criterion for choosing a proper molding condition was provided.

Other than these experimental efforts, a new numerical simulation approach was developed to obtain better control for growing complex gradient porous structures. First, rheological characterization was combined with CFD (computational fluid dynamics) to simulate the quiescent annealing process. According to experimental results from other researchers, there is a simple relation between 2D and 3D coarsening rates for a co-continuous polymer blend. If a similar relation could be obtained

between 2D and 3D simulation, the computational cost could be greatly reduced. To verify the existence of the aforementioned relation, the 2D and 3D coarsening rates were calculated through simulation on a simplified 3D model. With 2D simulation, both the initiation linear growth region and the later stage plateau were predicted, and these findings agreed with experimental results from literature. Non-isothermal temperature field was also incorporated in the model to predict the phase size distribution. Finally, the experimental conditions used in the creations of 1D and 2D gradient porous structures were applied in numerical simulations. The simulation results closely matched the experimental results.

CHAPTER 1

INTRODUCTION

1.1   Introduction

A polymer blend by definition is a mixture of two or more polymers which may have different physical and/or chemical properties. Because of the large number of repeat units existing in a polymer chain, even minor difference in physical and/or chemical properties can make two polymers immiscible with each other. [1-3] The immiscibility tends to induce phase separation in the blend. Since polymers normally have a much higher viscosity comparing with common low molecular weight species such as air and water, the phase separation process can be slow enough to be "frozen" with an easily accessible cooling rate. Based on the concentration ratio, chemical interaction, molecular weight, processing conditions, etc., the frozen polymer blend can have droplet-matrix, matrix-fiber, lamellar, co-continuous phase morphology, or some combination of these elementary phase morphology, as shown in Fig. 1.1. [3, 4] Each of these phase morphology has found its applications in various areas. For example, PS (polystyrene)/PDMS (Polydimethylsiloxane) blend with PDMS forming a droplet phase has been successfully used to improve the impact strength of PS. [5, 6] Sun and coworkers [7, 8] utilized blends with fibrous morphology to create nanofibers using a traditional melt spinning technique. Polymer blends with laminar phase morphology have been used by researchers to tune the barrier property of materials. [9-13] In this thesis research, however, the focus was placed on polymer blends with

co-continuous phase morphology.

Figure 1.1: Different types of blend morphology from polymer mixing: (a) droplet-matrix structure; (b) matrix-fiber structure; (c) lamellar structure; (d) co-continuous structure. (Reused with permission from the publishers of Potschke 2003 and Zumbrunnen 2001) [3,4]

A co-continuous polymer blend differs from other types of blends for its ability to be transferred into a porous material with interconnected microchannels. [14-17] This unique property comes from the interpenetrating phase structure of a co-continuous polymer blend, as shown in Fig. 1.2. Ideally, the two components inside a co-continuous blend should be indistinguishable by structural analysis. They should

2

be completely identical and complementary to each other spatially. It is not difficult to image that, after one component is removed, the rest of the material will form an interconnected network with an open pore structure inside. Experimentally, the pore formation process is conducted by selectively extracting the sacrificial phase while leaving the structure formation component intact. The resulting porous structure usually has an average pore size in the range of micrometers. The actually value of the pore size is determined by the chemical interaction between the two components and the mixing condition. [3, 6]
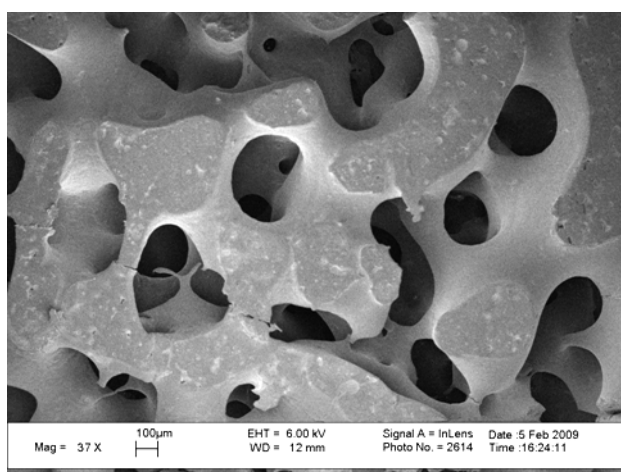
Figure 1.2: Phase morphology of a co-continuous polymer blend after one phase is extracted. [16]

Another property which makes a co-continuous polymer blend special is its tendency to coarsen its phase size during annealing. [18-22] When a co-continuous polymer blend is heated above its flow temperature (melting temperature for semicrystalline polymer and rubber plateau termination temperature for amorphous polymer) the original fine phase structure can become coarser and coarser to minimize the system free energy. [1, 3] In this coarsening process, interfacial tension and viscous stress compete with each other and decide the coarsening rate. Through experiments, researchers have found that the coarsening rate is linearly related with the ratio of interfacial tension coefficient and zero-shear viscosity. [23, 24] A large interfacial tension indicts the two components favor to be separated and naturally leads to a high coarsening rate. On the other hand, higher zero-shear viscosity makes any macro-scale flow more difficult and results in smaller coarsening rate. These factors have been applied by many researchers to produce porous material with desired pore sizes for different applications.[14-17]

Even though co-continuous polymer blend has the aforementioned unique properties, there are several technical issues which need to be addressed to open more opportunities for the application of this material. First, the possibility of generating gradient porous materials from co-continuous polymer blends should be explored. Currently, results appeared in numerous publications are still limited to homogeneous porous material. However, natural functional materials seldom have uniform structures. For example, natural porous materials such as wood, plant seeds, egg shell, bone, skin, etc., typically have a gradient porous structure (GPS), meaning that the porosity is not

uniform. Rather, it is distributed in space so as to maximize the overall performance of the structure. Often, the pore size continuously varies from the skin to the core, as in bone and in egg shell. [25] In bone, regions of dense "cortical" bone neighbor regions of low-density "trabecular" bone. With pore sizes decreasing from the core to the skin, bone is able to maintain a highly permeable core and yet provide an outer wall structural integrity. The increase of stiffness and strength with the reduction in pore size is understandable from both experimental and theoretical perspectives. The above natural materials exemplify the unique capabilities of GPSs, particularly the ability to integrate different functions, often contradictory, and achieve an optimized design. The incorporation of GPSs in synthetic materials may lead to the creation of new functional materials for many innovative applications. This has been the main thrust for the recent development of microcellular polymers for lightweight structural applications. [26-28] However, very few techniques have been reported on the fabrication of synthetic materials with GPSs. These reported techniques typically have a low resolution, prohibiting the creation of fine GPSs, and are limited to simple part geometries and shapes. Creation of a continuously varying and spatially controlled gradient in porosity with interconnected open pores represents an additional challenge for these processing steps.

Another technical challenge for co-continuous polymer blend is the incorporation of a large amount of solid particles. These particles are added to introduce properties which do not exist in the structure forming polymer materials. [29-36] For instance, the polymers used in the fabrication of biomedical scaffolds are mostly

bio-inert. This is desirable as they do not cause any inflammation reaction in the surrounding tissue. However, in some cases, bioactivity is needed to accelerate the tissue regeneration and overall recovery process. For this purpose, bioactive ingredients are added into the system by mixing them with the polymer matrix. [29]

The incorporation of these solid bioactive particles tends to drastically change the shear viscosity of the matrix material and makes the required co-continuous structure very difficult to get. Similar situation happens when one tries to create a conductive porous material using the co-continuous polymer blend approach. In this case, thermal and/or electrical conductive particles such as carbon black particles, CNTs (carbon nanotubes), and metal particles need to be incorporated into the co-continuous blend without sacrificing the co-continuity of the material. [30-36] An effective strategy for the fabrication of co-continuous polymer blend with high solid particle loading needs to be developed for these applications.

Other than the aforementioned material issues, creation of porous structures with well-defined external shapes represents another technical challenge. In contrast to the immense literature in porous material generation, micropatterning of porous devices remains a technical challenge. Most well-known techniques for processing porous materials, such as gas foaming, powder sintering, and solid freeform fabrication, have limited capability due to their relatively poor morphological control and/or low geometrical resolution at smaller sizes. Recently, Wessling and coworkers [37, 38] developed a phase separation micromolding process for generating micropatterns with internal pores down to submicron sizes. They casted a concentrated polymer solution

onto a micropatterned mold and sequentially cooled down the solution to induce the phase separation. Freeze drying was employed after the material was solidified to extract the solvent and form the desired porous structure. This process has been used for generating micropatterned devices, such as microsieves [39, 40] and porous scaffolds [41-46], for filtration and biomedical applications. However, there are some fundamental limitations with this process. The use of a large amount of solvent leads to a slow and environmentally unfriendly process. More critically, the pore size and its distribution from this thermodynamically unstable process are hard to control. The resulting devices also tend to have a dense skin formed which is undesired in filtration and scaffolding applications. A desired process for micropatterning porous devices would be able to in situ control the generation of the porous structure while achieving high geometrical patterning accuracy. One versatile technique for controllable generation of porous structures is through the aforementioned co-continuous polymer blend method [47-50]. By tuning the material properties and the process parameters, one can generate a desired porous structure with well-defined pore size and size distribution. However, the tendency for co-continuous phase structure to be severely deformed in the molding step still limits its application on the device level where precise shapes are essential for the device to function properly.

1.2 Research objectives and technical approaches

The primary objective for this research is to develop techniques for the creation of engineered porous structures from co-continuous polymer blend. To be

more specific, this research is designed to address the aforementioned technical challenges regarding the generation of gradient porous structures, the production of highly particle loaded porous materials, and the fabrication of porous objects with well-defined geometries. Another research objective is to understand the fundamental mechanisms involved in these proposed research topics and provide guidance for future study.

In this study, a new method, utilizing the unique thermal flow behavior of immiscible polymer blends, for controllable generation of polymeric gradient porous structures was investigated. By controllable variation of the temperature distribution in the blend, a spatially varied and controllable gradient in phase structure is created. After dissolution of one of the two phases, the desired porous structure of the remaining polymer is obtained. With a model blend of PLA (poly lactic acid) and PS (polystyrene), three types of gradient porous structures were created, each resulting from a unique temperature field incorporated in the annealing setup. The pore size resulting from these annealing experiments varied from several microns to several hundreds of microns, distributed in the space and interconnected through the original material. The unique gradient in pore size in each case was corrected with a specific temperature field developed in each special annealing setup. A positive temperature gradient resulted in a growth rate gradient in this direction. With deeper understanding of this novel process, more complex porous structures with designed gradient in pore size can be produced.

Other than utilizing thermal boundary condition to generate gradient porous

structure, the possibility of using geometrical confinement to produce gradient or even oriented pore structure has been explored in this research. For a material to be useful, it needs to be molded into a desired shape. For co-continuous polymer blend, this molding step will be followed by an in-mold annealing process to grow the pores into desired size. In this molding and annealing sequence, the blend inevitably needs to contact with the mold wall. It is understood that, due to the so-called boundary effects, the material in contact with the mold wall has different kinematic and dynamic conditions from the inner material. The resulting phase structure near the mold wall may be largely different from that in the bulk. While numerous studies [14-17] have been performed to elucidate the thermal annealing effects on the bulk structure, such boundary effects from geometrical confinement are little understood. In this research, possible effects from geometrical confinement during in-mold annealing were explored. A 50/50 wt% PLA/PS blend was compression molded and annealed between two parallel mold plates. Different conditions for geometrical confinement, including varied gap size and compression ratio, as well as modified surface properties, were employed. Understanding the influences from these boundary effects may lead to the development of more capable processes for innovative porous materials.

To produce a highly particle loaded porous polymer composite, a new processing technique which combines melt blending and after-mixing small-strain oscillation was developed and explored. A particular attention was paid to the formation of the initial phase structure so that the desired co-continuous phase morphology can be produced after the blending step. To reach this goal, the blending

step was specially designed to overcome the negative effect caused by the drastic change in shear viscosity after the addition of solid particles. As a case study, this technique was used to generate a highly HA (hydroxyapatite) loaded PLGA (poly (lactic-co-glycolic)) nanocomposite with an interconnected microporous structure. The mechanisms underneath the experimental observations, particularly on the enhanced particle migration under oscillatory shear, were discussed, and strategies for producing highly particle loaded biopolymers with interconnected microporous structures were proposed. Even though the example was for biomedical applications and the particle shape was close to sphere, the discussion about the mechanism of particle migration might be extended to other applications and particles with non-spherical shapes.

SEM (scanning electron microscopy) observation, rheological characterization, and experimental data from literature were integrated with numerical modeling to deepen the understanding about the coarsening process of co-continuous polymer blends. Through modeling the isothermal annealing process for objects with different dimensions, an empirical relation of coarsening rates between 2D and 3D modeling was proposed and compared with experimental results. Beyond isothermal annealing, numerical simulation was applied in designing gradient porous structures. For this kind of simulation, data collected from experimental measurements were fitted with the WLF (Williams-Landel-Ferry) model to predict the values of zero-shear viscosity at various annealing temperatures. In the meantime, the temperature distribution inside a blend was calculated according to a particular thermal boundary condition and the assumption that the blend had uniform thermal conductivity. These two sets of data

were then fed into the Cahn-Hilliard model to simulate the non-isothermal annealing process for this thermal boundary condition. Matching between experimental results and the simulation results demonstrated the feasibility of utilizing numerical simulation to guide the design of proper thermal boundary conditions for generating porous materials with various pore size gradients.

1.3   References

1. Paul DR and Barlow JW, Polymer blends (or alloys), Journal of Macromolecular Science-Reviews in Macromolecular Chemistry and Physics, 1980. C18(1): p. 109-168.

2. Potschke P and DR Paul, Detection of co-continuous structures in SAN/PA6 blends by different methods. Macromolecular Symposia, 2003. 198: p. 69-81.

3. Potschke P and Paul DR, Formation of co-continuous structures in melt-mixed immiscible polymer blends, J. Macromole. Sci.-Polymer Reviews, C 43, 87-141, 2003.

4. Zumbrunnen DA and Inamdar S, Novel sub-micron highly multi-layered polymer films formed by continuous flow chaotic mixing, Chemical Engineering Science, 56, 3893–3897, 2001.

5. Lyngaae-Jorgensen, J, Structuring of interface-modified polymer blends. International Polymer Processing, 1999. 14(3): p. 213-220.

6. Maric, M and Macosko CW, Block copolymer compatibilizers for polystyrene/poly(dimethylsiloxane) blends. Journal of Polymer Science Part B-Polymer Physics, 2002. 40(4): p. 346-357.

7. Wang, D, et al., Controllable fabrication and properties of polypropylene nanofibers. Polymer Engineering and Science, 2007. 47(11): p. 1865-1872.

8. Xiang, B, et al., Novel poly(ethylene-co-acrylic acid) nanofibrous biomaterials for peptide synthesis and biomedical applications. Journal of Biomedical Materials Research Part A, 2010. 95A (1): p. 245-255.

9. Huang, CH, et al., Morphological, thermal, barrier and mechanical properties of LDPE/EVOH blends in extruded blown films. Journal of Polymer Research, 2004. 11(1): p. 75-83.

10. Jang, JS and Lee DK, Oxygen barrier properties of biaxially oriented polypropylene/polyvinyl alcohol blend films. Polymer, 2004. 45(5): p. 1599-1607.

11. Jarus, D, Hiltner A, and Baer E, Barrier properties of polypropylene/polyamide blends produced by microlayer coextrusion. Polymer, 2002. 43(8): p. 2401-2408.

12. Kwon, O and D.A. Zumbrunnen, Production of barrier films by chaotic mixing of plastics. Polymer Engineering and Science, 2003. 43(8): p. 1443-1459.

13. Yeo, JH, et al., Rheological, morphological, mechanical, and barrier properties of PP/EVOH blends. Advances in Polymer Technology, 2001. 20(3): p. 191-201.

14. Yuan, ZH and Favis BD, Macroporous poly(L-lactide) of controlled pore size derived from the annealing of co-continuous polystyrene/poly(L-lactide) blends. Biomaterials, 2004. 25(11): p. 2161-2170.

15. Yuan ZH and Favis BD, Influence of the Efficacy of Interfacial Modification on the Coarsening of Cocontinuous PS/HDPE Blends During Quiescent Annealing, J. Polym. Sci. Part B: Polym Phys, 44, 711-721, 2006.

16. Yao DG, Zhang W, and Zhou JG, Controllable Growth of Gradient Porous Structures, Biomacromolecules, 10, 1282–1286, 2009.

17. Zhang W, Deodhar S, and Yao DG, Geometrical confining effects in compression molding of co-continuous polymer blends, Annals of Biomedical Engineering, 38(6), 1954–1964, 2010.

18. Galloway JA, et al., Block copolymer compatibilization of cocontinuous polymer blends. Polymer, 2005. 46(1): p. 183-191.

19. Lopez-Barron CR and Macosko CW, Direct Measurement of Interface Anisotropy of Bicontinuous Structures via 3D Image Analysis. Langmuir, 2010. 26(17): p. 14284-14293.

20. Lopez-Barron CR and Macosko mCW, Characterizing Interface Shape Evolution in Immiscible Polymer Blends via 3D Image Analysis. Langmuir, 2009. 25(16): p. 9392-9404.

21. Maric M and Macosko CW, Block copolymer compatibilizers for polystyrene/poly(dimethylsiloxane) blends. Journal of Polymer Science Part B-Polymer Physics, 2002. 40(4): p. 346-357.

22. Pyun A, et al., Synchrotron X-ray microtomography for 3D imaging of polymer blends. Macromolecules, 2007. 40(6): p. 2029-2035.

23. Lopez-Barron CR and Macosko CW, A new model for the coarsening of cocontinuous morphologies. Soft Matter, 2010. 6(12): p. 2637-2647.

24. Yuan ZH and Favis BD, Coarsening of immiscible co-continuous blends during quiescent annealing. Aiche Journal, 2005. 51(1): p. 271-280.

25. Zhang J Z, Wang JG, Ma J J, Journal of Zhejiang University Science 2005, 6A, 1095–1099.

26. Kumar V, Celluar Polymers 1993, 12, 207–223.

27. Suh NP, Macromolecular Symposia 2003, 201, 187–201.

28. Gong S, Yuan M, Chandra A, Winardi A, Osorio A, Turng LS, International Polymer Processing 2005, 20, 202–214.

29. Zhang W, et al., Fabrication of interconnected microporous biomaterials with high hydroxyapatite nanoparticle loading. Biofabrication, 2010. 2(3).

30. Potschke P, Fornes TD, and Paul DR, Rheological behavior of multiwalled carbon nanotube/polycarbonate composites. Polymer, 2002. 43(11): p. 3247-3255.

31. Koysuren O, Yesil S, and Bayram G, Effect of Solid State Grinding on Properties of PP/PET Blends and Their Composites with Carbon Nanotubes. Journal of Applied Polymer Science, 2010. 118(5): p. 3041-3048.

32. Laredo E, et al., AC Conductivity of Selectively Located Carbon Nanotubes in Poly(epsilon-caprolactone)/Polylactide Blend Nanocomposites. Biomacromolecules, 2010. 11(5): p. 1339-1347.

33. Shukla S, et al., Polymeric Nanocomposites Involving a Physical Blend of IR Sensitive Quantum Dots and Carbon Nanotubes for Photodetection. Journal of Physical Chemistry C, 2010. 114(7): p. 3180-3184.

34. Yang QQ and Liang JZ, Electrical Properties and Morphology of Carbon Black-Filled HDPE/EVA Composites. Journal of Applied Polymer Science, 2010. 117(4): p. 1998-2002.

35. Saquing CD, Manasco JL, and Khan SA, CELL 249-Electrospun metal nanoparticle-alginate based polymer blend nanofiber composites for biomedical applications. Abstracts of Papers of the American Chemical Society, 2008. 235: p. 249-CELL.

36. Faghihi M and Shojaei A, Properties of Alumina Nanoparticle-Filled Nitrile-Butadiene-Rubber/Phenolic-Resin Blend Prepared by Melt Mixing. Polymer Composites, 2009. 30(9): p. 1290-1298.

37. Vogelaar L, Barsema JN, Van Rijn CJM, Nijdam W, and Wessling M, Phase separation micromolding, Adv. Mater, 15, 16, 1385-1389, 2003.

38. Vogelaar L, Lammertink RGH, Barsema JN, Nijdam W, Bolhuis-Versteeg LAM, Van Rijn CJM, and Wessling M, Phase separation micromolding: a new generic approach for microstructuring various materials, Small, 1, 6, 645-655, 2005.

39. Girones M, Akbarsyah IJ, Nijdam, W, Van Rijn CJM, Jansen HV, Lammertink RGH, and Wessling M, Polymeric microsieves produced by phase separation micromolding, J. Membrane Science, 283, 411-424, 2006.

40. Bikel M, Culfaz PZ, Bolhuis-Versteeg LAM, Perez JG, Lammertink RGH, and Wessling M, Polymeric microsieves via phase separation microfabrication: process and design optimization, J. Membrane Science, 347, 93-100, 2010.

41. Papenburg BJ, Schuller-Ravoo S, Bolhuis-Versteeg LAM, Hartsuiker L, Grijpma DW, Feijen J, Wessling M, Stamatialis D, Designing porosity and topography of poly(1,3-trimethylene carbonate) scaffolds, Acta Biometerialia, 5, 3281-3294, 2009.

42. Lam MT, Clem WC, Takayama SC, Reversible on-demand cell alignment using reconfigurable microtopography, Biomaterials, 29, 1705-1712, 2008.

43. Isenberg BC, Tsuda Y, Williams C, Shimizu T, Yamato M, Okano T, Wong JY, A thermoresponsive, microtextured substrate for cell sheet engineering with defined structural organization, Biomaterials, 29, 2565-2572, 2008.

44. Yucel D, Kose GT, Hasirci V, Polyester based nerve guidance conduit design, Biomaterials, 31,1596-1603, 2010.

45. Berry CC, Campbell G, Spadiccino A, Robertson M, Curtis ASG, The influence of microscale topography on fibroblast attachment and motility, Biomaterials, 25, 5781-5788, 2004.

46. Sarkar S, Lee GY, Wong JY, Desai TA, Development and characterization of a porous micro-patterned scaffold for vascular tissue engineering applications, Biomaterials, 27, 4775-4782, 2006.

47. Wu GZ, Xu HB, Zhou T, Morphology evolution, crystalline orientation, and thermal expansion of PA6/SEBS blends with nanolayer networks, Polymer, 51, 3560-3567, 2010.

48. Yu W, Zhou W, Zhou CX, Linear viscoelasticity of polymer blends with co-continuous morphology, Polymer, 51, 2091-2098, 2010.

49. Pyun A, Bell JR, Won KH, Weon BM, Seol SK, Je JH, Macosko CW, Synchrotron X-ray Microtomography for 3D Imaging of Polymer Blends, Macromolecules, 40, 2029-2035, 2007.

50. Galloway JA, Koester KJ, Paasch BJ, Macosko CW, Effect of sample size on solvent extraction for detecting cocontinuity in polymer blends, Polymer, 45, 423-428, 2004.

CHAPTER 2

LITERATURE REVIEW

As discussed in Chapter 1, due to the capability of forming interconnected microporous structures, co-continuous polymer blends are promising materials for many emerging applications. However, there are still several major technical challenges needing to be addressed to open up opportunities for practical applications. In this chapter, a comprehensive literature survey on porous materials processing are presented, and the primary technical challenges are discussed. To be more specific, the following topics are reviewed: 1) generation of porous structures; 2) coarsening kinetics of co-continuous polymer blends; 3) polymer blend/nanoparticle complex; and 4) micropatterned porous structures.

2.1 Techniques for generating porous structures

Due to their large internal surface area, porous materials have been widely used in applications where high surface activity is desired. Example applications are extracellular scaffolds for tissue engineering [1, 2], porous substrates for catalytic reaction [4, 5], and permeable media for membrane filtration [6, 7]. Numerous investigations in porous materials processing have been conducted, and different fabricating techniques for making porous structures have been reported. Mikos et al. [8, 9] developed a solvent-casting and particulate-leaching method, in which a highly concentrated and

viscous polymer solution was mixed with sieved salt particles, and use it to produce various porous cell foams from biodegradable polymers. Another widely reported technique for creating porous materials is called TIPS (thermally induced phase separation). This technique has mostly been applied to fabrication of porous scaffolds for tissue engineering. [10-17] Specifically, one started with an organic solution of a polymer and by decreasing the system temperature to induce a phase separation. Depending on the relation between the solvent crystallization temperature and the liquid-liquid transition temperature, TIPS can be divided into solid-liquid phase separation (solvent crystallization temperature higher than the liquid-liquid transition temperature) and liquid-liquid phase separation. [11, 14] In the first case, the generated pores duplicate the shape of the crystals formed by the solvent, as the polymer component is expelled from the solvent crystallization front and stays at the interfaces between the crystal grains. [11, 14] By controlling the type of solvent, the quenching depth, the polymer concentration, and the thermal gradient, Ma et al. [11, 14] formed biodegradable foams with different architectures, as shown in Fig. 2.1
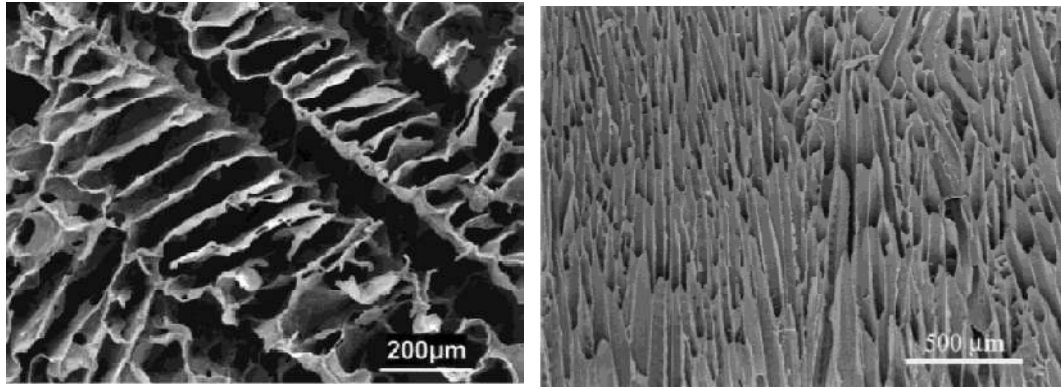
(a)   (b)

Figure 2.1: Thermally induced solid-liquid phase separation: (a) SEM micrograph of a PLLA scaffold prepared from PLLA-dioxane solution with a thermally induced solid-liquid phase separation (Reused with permission from the publisher of Zhang, 1999) [14]; (b) SEM micrograph of a PLLA scaffold prepared from PLLA-benzene solution with a thermally induced solid-liquid phase separation involving a uniaxial temperature gradient (Reused with permission from the publisher of Ma, 2001)[11].

Compared with solid-liquid phase separation, liquid-liquid phase separation is subject to more complex process kinetics. The liquid-liquid phase transition temperature is higher than the solvent crystallization temperature. Based on the polymer concentration, the solvent type, the quenching depth, and the crystallinity of the polymer, liquid-liquid phase separation can lead to different phase structures including droplet-matrix phases (between binodal and spinodal lines), bicontinuous patterns (under spinodal line), and gel structures (with semicrystal polymer), as shown in Fig. 2.2 [17]. After sublimation by freeze drying, one can obtain a nano-fibrous network from a biodegradable polymer through thermally induced gelation. The fiber can have diameter in the range from 50 to 500 nm, making the matrix morphologically

very similar to type I collagen, the organic matrix in natural bones. Experimentally, a better cell attachment is achieved in the nano-fibrous matrix, comparing with the traditional non-fibrous scaffold. [18] And this difference was attributed to the high surface-to-volume ratio of the nano-fibrous matrix. Another advantage of this thermally induced gelation method is its ability to be combined with other scaffold fabrication techniques. For example, by combining with the particulate-leaching method, one can introduce nano-fibrous walls to scaffolds with interconnected spherical macropores. Likewise, by combining with solid freeform fabrication, scaffolds with well-defined complex 3D structures can be produced. The resulting compound scaffold structures in these two cases are shown in Fig.2.3. [19, 20]
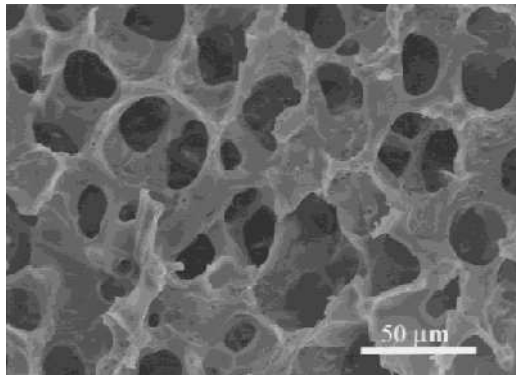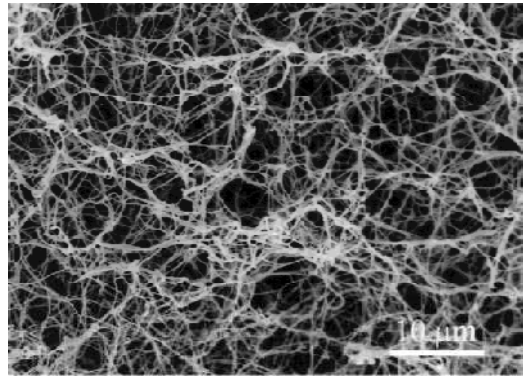
(a)   (b)

Figure 2.2: Thermally induced liquid-liquid phase separation: (a) SEM micrographs of PLGA scaffold prepared with a thermally induced liquid-liquid phase separation; (b) SEM micrographs of PLLA nano-fibrous network prepared from PLLA/THF solution with a thermally induced gelation process (Reused with permission from the publisher of Ma, 1999) [17].
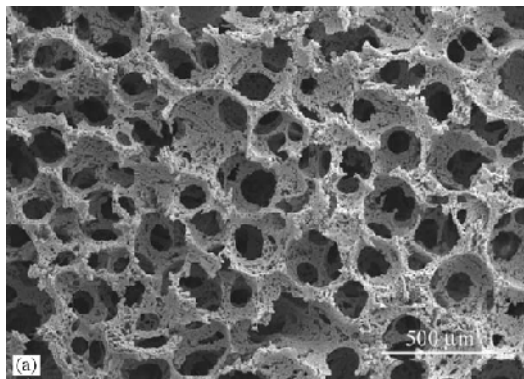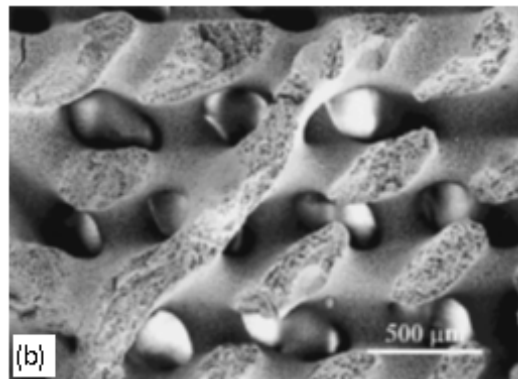
Figure 2.3: Thermally induced phase separation combined with other pore-forming technique: (a) SEM micrographs of a nano-fibrous PLLA scaffold with interconnected spherical macropores prepared by combining a paraffin sphere-leaching technique and a thermally induced gelation process (Reused with permission from the publisher of Chen, 2004) [19]; (b) SEM micrographs of PLLA nano-fibrous matrix with helicoidal tubular macropore network prepared from PLLA/THF solution and a helicoidal sugar fiber assembly (Reused with permission from the publisher of Zhang, 2000) [20].

Gas foaming is another popular method for making polymeric scaffolds for tissue engineering applications. This method is particularly useful for the fabrication of highly porous polymeric scaffolds (95% porosity) to transfer cells and growth factors. The gas foaming process begins with the exposure of the polymer to high-pressure (e.g. 800 psi) carbon dioxide or nitrogen. After the polymer is saturated with gas, the high pressure is suddenly released. The pressure difference between the inside and the outside causes formation of gas bubbles in the polymer matrix. [21] Probably caused by the depletion of CO_2 in the region between the growing pores, the structure obtained from gas foaming normally contains closed pores. [21] To facilitate the exchange of nutrition and waste throughout the scaffold, the pores in the scaffold should be interconnected. Special techniques have been developed to introduce connections among closed cells. For example, Wang et al. [22, 23] combined solid-state foaming with ultrasonic vibration to make porous structures with interconnected channels.

Another method worth mentioning is solid freeform fabrication (SFF). SFF originally was used to fabricate prototype engineering parts and that was why "rapid prototyping" has been used exchangeably as SFF in the literature. Since 1987 when the first commercial SFF machine was introduced into the market, more SFF technologies have been developed. [20] Basically, they differentiated from each other through how the layers are laid down, solidified, and attached to previous layers. Some of these SFF technologies have been modified specially for biomedical tissue engineering, such as three-dimensional printing (3DP) [26, 27], fused deposition modeling (FDM) [28-30, 43-45], ink-jet printing and indirect casting (IC) [24, 31-35], stereolithography (SL) [36-39], and

selective laser sintering (SLS) [40-42]. All these SFF techniques differ from the aforementioned solving leaching and phase separation techniques for being able to precisely produce complex 3D geometries, as shown in Fig. 2.5.
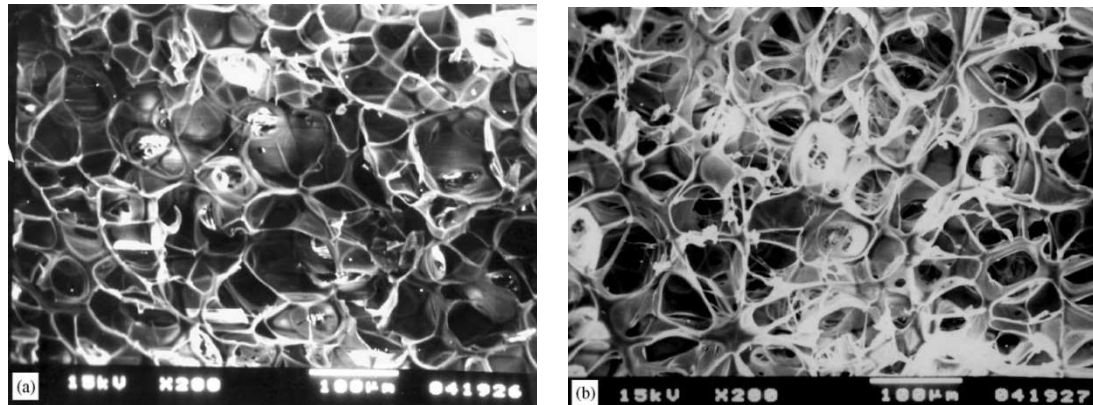
Figure 2.4: The effect of ultrasound: (a) PLA foam before ultrasound exposure and (b) after ultrasound exposure, showing a porous structure with enhanced inter-pore connectivity. (Reused with permission from the publisher of Wang, 2006) [22]

<center>(a)   (b)</center>
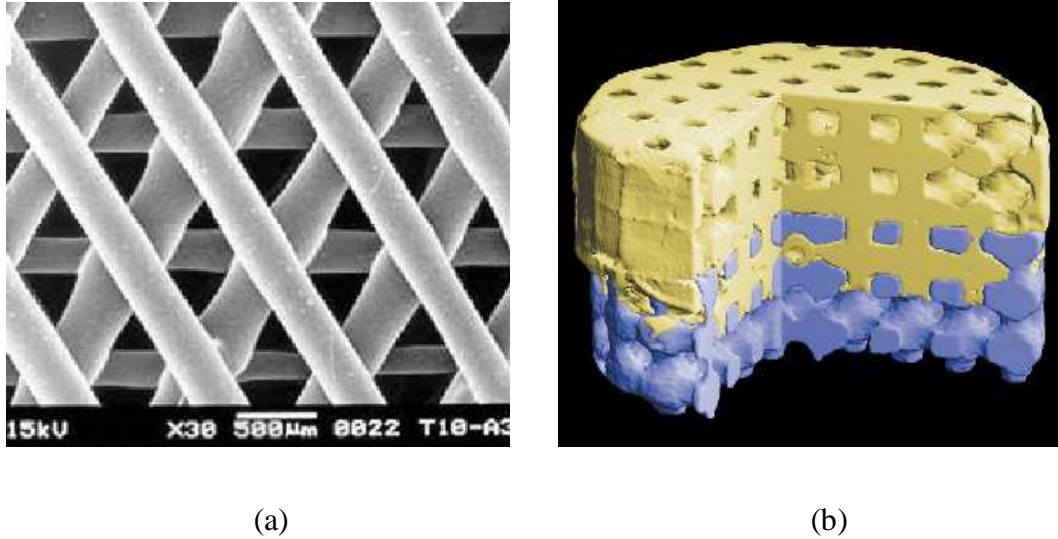
Figure 2.5: Solid freeform fabrication: (a) SEM image of cut surface of PCL scaffold fabricated using T10 tip, sample group (Reused with permission from the publishers of Zein, 2002) [24]; (b) Colorized µCT of biphasic PLA/HA ceramic scaffold (top=PLA, yellow=PLA, blue=HA). Globally, PLA pores are 600 µm and HA pores are 500 µm (Reused with permission from the publisher of Taboas, 2003) [25].

2.2   Coarsening kinetics of co-continuous polymer blends

The superior properties of co-continuous polymer blend come from its unique phase morphology. [1, 46] Unlike other phase morphologies, the complex and intertwinding phase structure inside a co-continuous polymer blend makes it difficult to be described with only one characteristic length scale. Such an interpenetrating phase structure can undergo phase coarsening when it is kept at a temperature higher than the flow temperature of both components. It is known for a long time that the main contributing factors for both the initial structure formation process and the following annealing process are interfacial tension and viscoelastic stress. [48-52] However, an effective model which can predict the coarsening kinetics by combining the two well-known dynamic factors with a set of geometric parameters is still a topic under investigation. For

<center>26</center>

instance, McMaster proposed a model in which the Tomotika's model was employed to describe the breakup and attraction of thin regions inside a co-continuous blend. [53] In the original work of Tomokita, the system was consisted of a cylindrical thread of liquid A immerged in a continuous matrix of liquid B. [54] The competition between interfacial tension and viscous stress decided the breakup of the cylindrical thread with diameter a. By assuming an exponential growth rate of the sinusoidal disturbances at the thread surface, the evolution of the dominant instability wave can be expressed as:

$$\alpha = \alpha_0 e^{qt} \tag{2.1}$$

where α_0 is the initial amplitude of the dominant instability and q is expressed as:

$$q = \frac{\Gamma \Omega}{2a\eta_m} \tag{2.2}$$

where Γ is the interfacial tension coefficient, Ω is the Tomotika's function, η_m is the viscosity of the matrix, and a is the filament radius. From Eq. (2.1) and Eq. (2.2), the initial growth rate of the dominant instability is governed by

$$\left.\frac{d\alpha}{dt}\right|_{t=0} = \frac{\alpha_0}{2a}\Omega\frac{\Gamma}{\eta_m} \quad . \tag{2.3}$$

Starting from the relation defined in Eq. (2.3) and the assumption that the coarsening rate of a co-continuous polymer blend is determined by the breakup of the necking region, McMaster [53] proposed the equivalence between the phase coarsening rate and the instability growth rate. This leads to a linear growth rate as also experimentally observed in many co-continuous polymer blends at their initial annealing stages.

Similar linear growth rate of the phase size has been predicted by Siggia [55] using scaling arguments for late stage spinodal decomposition in concentrated mixture. Actually, the concentration of Siggia's mixture has to be above the percolation threshold. At this concentration, a material with phase morphology very close to that of co-continuous polymer blend will be formed at the late stage of the spinodal decomposition. Even though the formation of a co-continuous polymer blend during melt mixing arises from intensive mechanical mixing and is different from that of Siggia's material, the major competing forces for both systems are interfacial tension and viscous stress. Therefore, the coarsening processes in these systems are expected to share similar kinetics. Such kinetics, in Siggia's model, was related to the interfacial tension driven capillary flow inside interconnected channels. By assuming all channels had cylindrical shapes, the average velocity of the capillary flow was calculated using Poiseuille's equation:

$$v = \frac{a^2}{8\eta} \frac{\Delta P}{\lambda} \qquad (2.4)$$

where a is the average radius of these channels, ΔP is the pressure difference caused by the interfacial tension, η is the zero-shear viscosity of the fluid inside the channel, λ is the characteristic length of the co-continuous structure. In his theory, Siggia employed the Young-Laplace Equation to calculate the pressure difference ΔP:

$$\Delta P = 2\Gamma H = \Gamma(k_1 + k_2) \qquad (2.5)$$

Where $H = 0.5(k_1 + k_2)$ is the mean curvature, and k_1 and k_2 are two principal curvatures of a surface/interface. Siggia further assumed that there is only one characteristic length and one velocity for the kinetics of the coarsening process (i.e. $v = d\lambda/dt$ and $a = \lambda = H^{-1}$). With these assumptions, the combination of Eq. (2.4) and (2.5) leads to the following simple expression for the evolution of the characteristic length:

$$\lambda = c\frac{\Gamma}{\eta}t .\qquad\qquad(2.6)$$

From Eq. (2.6), Siggia's model predicts the same linear growth rate of the characteristic length for a concentrated mixture at its late stage of spinodal decomposition.

Even though both McMaster's model and Siggia's Model can nicely describe the initial linear growth behavior of a coarsening co-continuous structure, they cannot predict the late reduction of the coarsening rate after the characteristic length reaches some critical values. This reduction in coarsening rate has been confirmed by different researching groups with various characterization techniques, including SEM, micro-CT (X-ray microtomography), and mercury porosimetry. [56-59] The first theoretical attempt on describing two-rate coarsening kinetics was conducted by Scholten et al. [58, 59] The most important concept introduced in Scholten's theory is a curvature dependent interfacial tension. To be more specific, Scholten considered the contribution of bending energy to the total interfacial energy. Utilizing Helfrich's elastic model [60], the interfacial tension for a curved interface was written as

$$\Gamma = \Gamma_0 + 2E_B(H - H_0)^2 + E_T K \tag{2.7}$$

in which Γ and Γ_0 are the interfacial tension of a curved and flat interface respectively, H and H_0 are mean curvature and spontaneous mean curvature, E_B is the elastic bending modulus, and E_T is the elastic torsion modulus. With the assumptions that $H_0=0$, $E_T=0$, and $H=1/\lambda$, Eq. (2.7) was transferred into

$$\Gamma = \Gamma_0 + 2\frac{E_B}{\lambda^2}. \tag{2.8}$$

Replacing Γ in Eq. (2.5) with this new expression for the interfacial tension of a curved interface, Scholten extended Siggia's model and obtained the following governing equations for the coarsening rate:

$$\frac{d\lambda}{dt} = \frac{\Gamma_0}{4\eta} + \frac{E_B}{2\eta}H^2 \approx \frac{\Gamma_0}{4\eta} + \frac{E_B}{2\eta}\lambda^{-2}, \tag{2.9}$$

$$\lambda - \sqrt{\frac{2E_B}{\Gamma_0}} \tan^{-1}(\frac{\lambda}{\sqrt{\frac{2E_B}{\Gamma_0}}}) \approx \frac{\Gamma_0}{\eta}t. \tag{2.10}$$

Eq. (2.10) can be further developed based on the value of $x = \lambda / \sqrt{2E_B/\Gamma_0}$ as $\tan^{-1}(y)$ has a value close to $y-y^3$ when $y \ll 1$ and $\pi/2$ when $y \gg 1$. With these asymptotes, Eq. (2.10) yields

$$\lambda \sim (2E_B t/\eta)^{1/3}, \text{ when } x \ll 1, \tag{2.11}$$

$$\lambda \sim \Gamma_0 t/\eta, \text{ when } x \gg 1. \tag{2.12}$$

From the first relation, one can see that, when the characteristic length is very small and the average curvature is sufficiently high, the elastic bending part of interfacial tension dominates and gives a nonlinear coarsening rate. As annealing goes on, the interface becomes flatter and the linear time dependency appears. According to Scholten's model, the kinetics of the coarsening process does have two regions. However, discrepancy was found between Eq. (2.12) and experimental data by Barron et al. [61]

After noticing the discrepancy between experimental results and the prediction of Scholten's model, Barron [61] proposed a new model in which the contribution of interfacial curvature was included into the framework of Siggia's model in a different way to avoid the assumption of $\lambda = H^{-1}$. The reason to remove this assumption was that λ and H^{-1} were comparable only at the early stage of the coarsening process. Following this analysis, Eq. (2.4) becomes

$$\frac{d\lambda}{dt} \propto \frac{\Gamma}{\eta} \lambda H \qquad (2.13)$$

which further leads to

$$\lambda \propto \exp\left[\frac{\Gamma}{\eta} \int H dt\right]. \qquad (2.14)$$

According to Barron's another publication, [56] symmetric immiscible polymer blends have symmetric distribution of mean curvature which centers at zero. Thus, the spatially averaged H in Eq. (2.14) equals zero at any time. To account for the influence of the interfacial curvature, a non-zero function of curvature needs to be used to

replace H is Eq. (2.14). Barron defined a new parameter called curvedness and used it to replace H. The definition of the curvedness, ζ, is provided in Eq. (2.15):

$$\zeta = \sqrt{\frac{k_1^2 + k_2^2}{2}} \qquad (2.15)$$

where k_1 and k_2 are the two principal curvatures for a local curved interface. From definition, k_1 and k_2 can be linked to the mean curvature (H) and the Gaussian curvature (K) through

$$k_1 = H + \sqrt{H^2 - K}, \qquad (2.16)$$

$$k_2 = H - \sqrt{H^2 - K}. \qquad (2.17)$$

The parameters H and K can be calculated using a coordinate transformation method and 3D reconstruction imaging. [56] The resulting relation among ζ, H, and K can be written as

$$\zeta^2 = 2|H|^2 - K. \qquad (2.18)$$

If $K=0$ is assumed, a simpler relation between ζ and the magnitude of the mean curvature H can be obtained. Different from H, the area averaged magnitude of ζ is a non-zero function and can be integrated with Eq. (2.14) to calculate the time dependent characteristic length λ. This new model was found to be able to predict both the early and the late stage coarsening behavior in a co-continuous polymer blend. Other than the prediction of the annealing kinetics, a new form of capillary number was proposed to predict the transition point for the annealing process:

$$Ca = \frac{\eta \dfrac{d \ln \lambda}{dt}}{\Gamma \zeta_A} \qquad (2.19)$$

where ζ_A is the area averaged curvedness defined as

$$\zeta_A = \frac{\displaystyle\sum_{i=1}^{N} \zeta_i A_i}{\displaystyle\sum_{i=1}^{N} A_i} \qquad (2.20)$$

where ζ_i and A_i are the local curvedness and the area of triangle i in a triangular mesh covering the interface. [56] From this model, Barron calculated the "universal" critical value for his newly constructed capillary number to be 0.00325 for all three FLPS (fluorescently labeled polystyrene)/SAN (styrene-acrylonitrile copolymer) symmetric blends.

These theoretical efforts not only deepen our understanding about the kinetics of the coarsening process in a co-continuous polymer blend but also demonstrate the importance of not over-simplifying a 3D problem by directly apply 2D experimental data. Cautiousness has to be given to the interpretation of 2D information for an intrinsically 3D problem. A well-constructed model is needed to recover 3D properties from simply and easily accessible 2D results.

2.3 Polymer blend/nanoparticle complex

Formation of polymer blends has been an effective way to create polymeric materials with balanced properties which are crucial for various applications. [1, 46] While being successfully employed in different areas, polymer blends are challenged with new applications desiring more advanced properties. For instance, in proton-exchange membrane applications, the blend is desired to have a good ionic exchange capacity and sufficient chemical stability. [62] In packaging applications, superior barrier property is indispensible. [9-13] In order for a material to be applicable in fabrication of field emission devices or electronic sensors, it has to be electrically conductive. [68-71] In most cases, however, these desired properties are lacking in common engineering polymeric materials. On the other hand, inorganic materials and/or metals are naturally inherited with these characteristics.

One effective way to modify the material properties of polymer blends is making polymer composites. This topic has attracted interests from many researchers. Hui et al. [72] found that the addition of a small amount of silica-based nanofillers could improve the tensile properties of a LDPE (low density polyethylene)/EVA (ethylene vinyl acetate) blend. The reinforcing effect was attributed to the crystallization along the silica nanofiller. They also found that the mixing sequence was important for the production of high strength composites as it could influence the dispersion quality for nanofillers. Persenaire and coworkers [73] reported synergistic effects of combining organomodified clay and compatibilizer on the morphology and mechanical property of polymer blends. Moreover, they noticed that the interface between the two

components was invariably occupied by clay platelets no matter the extra clay stayed

in the polar or non-polar phase, as shown in Fig. (2.6).
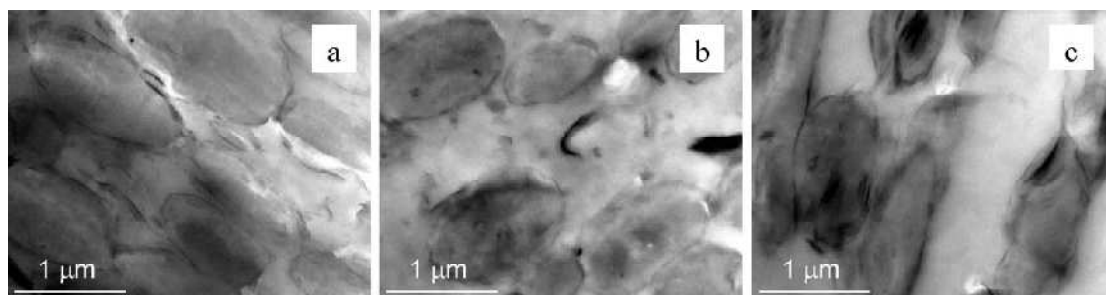
Figure 2.6: TEM microphotographs of cryo-fractured surface of LDPE (low density polyethylene)/PBAT (poly butylene adipate/terephthalate) 40/60 wt% nanocomposites: (a) EVA (ethylene/vinyl acetate copolymer)/MAgPE(maleic-anhydride-grafted polyethylene) 75/25 4wt%, C30 3 wt%; (b) EVA/MAgPE 50/50 4wt%, C30 3 wt%;(c) EVA/MAgPE 25/75 4wt%, C30 3 wt%. (Reused with permission from the publisher of Persenaire, 2010) [73]

In addition to improving the mechanical strength, nanofillers were utilized to

enable other unusual properties. Mohammed et al. [74] utilized the affinity between CB

(carbon black) nanoparticle and polybutadiene segments in SBS

(styrene-butadiene-styrene) to localize CB nanoparticle at the interface of a PP

(polypropylene)/PS (polystyrene) blend, Fig. 2.7. This special spatial arrangement

greatly reduces the percolation threshold concentration of CB. The co-continuous

polymer composite has a drastic increase in conductivity with a CB concentration as

low as 5 vol%.
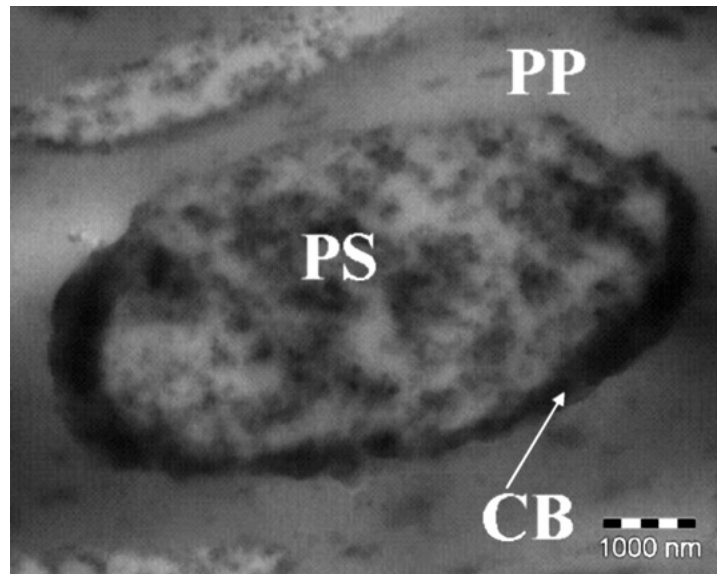
Figure 2.7: TEM micrograph of 1 vol% carbon black filled (70/30) polypropylene/polystyrene blend containing 5 vol% styrene-butadiene-styrene. (Reused with permission from the publisher of Mohammed, 2008) [74]

Another interesting phenomenon was reported by Kelarakis [75] on optical property of a nanoparticle loaded PP/PEO (polyethylene oxide) blend. In the study, the addition of nanoclay prevented the clustering of the dispersed phase and transferred the blend from opaque to transparent, as shown in Fig. (2.8).
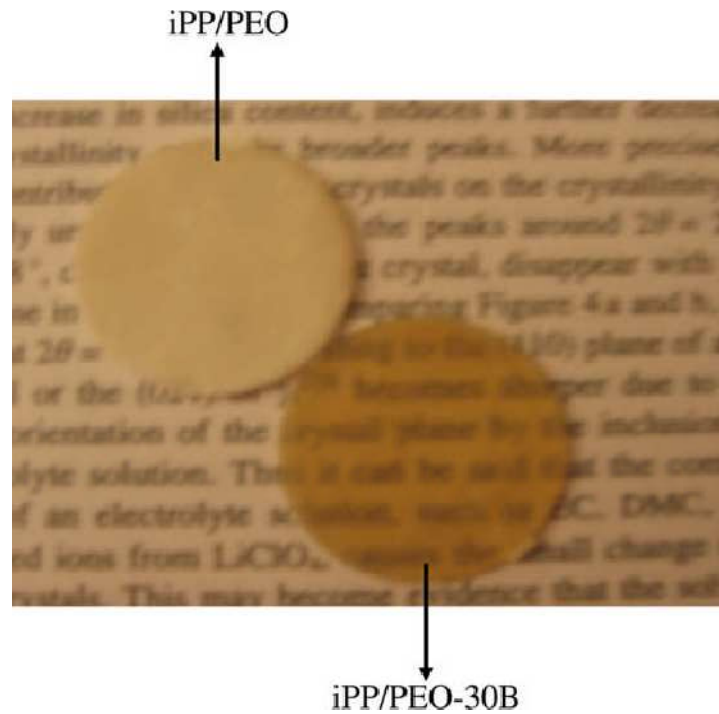
Figure 2.8: photographs of an unfilled blend and the corresponding nanocomposite. (Reused with permission from the publisher of Antonios, 2008) [75]

Nanoparticle was also used to regulate the phase separation kinetics of polymer blend. Elias et al. [76] investigated the morphology and rheology of blends filled with silica nanoparticles and found a significant reduction in phase size caused by the addition of silica nanoparticle. A hundred of nanometers thick interface which was crowded with a large amount of silica nanoparticles was observed in their PP/silica/PS composite system, as shown in Fig. (2.9). Moreover, migration of hydrophilic silica nanoparticle from PP to PS was noticed when pre-mixed silica/PP was employed in the creation of the PP/silica/PS composite.
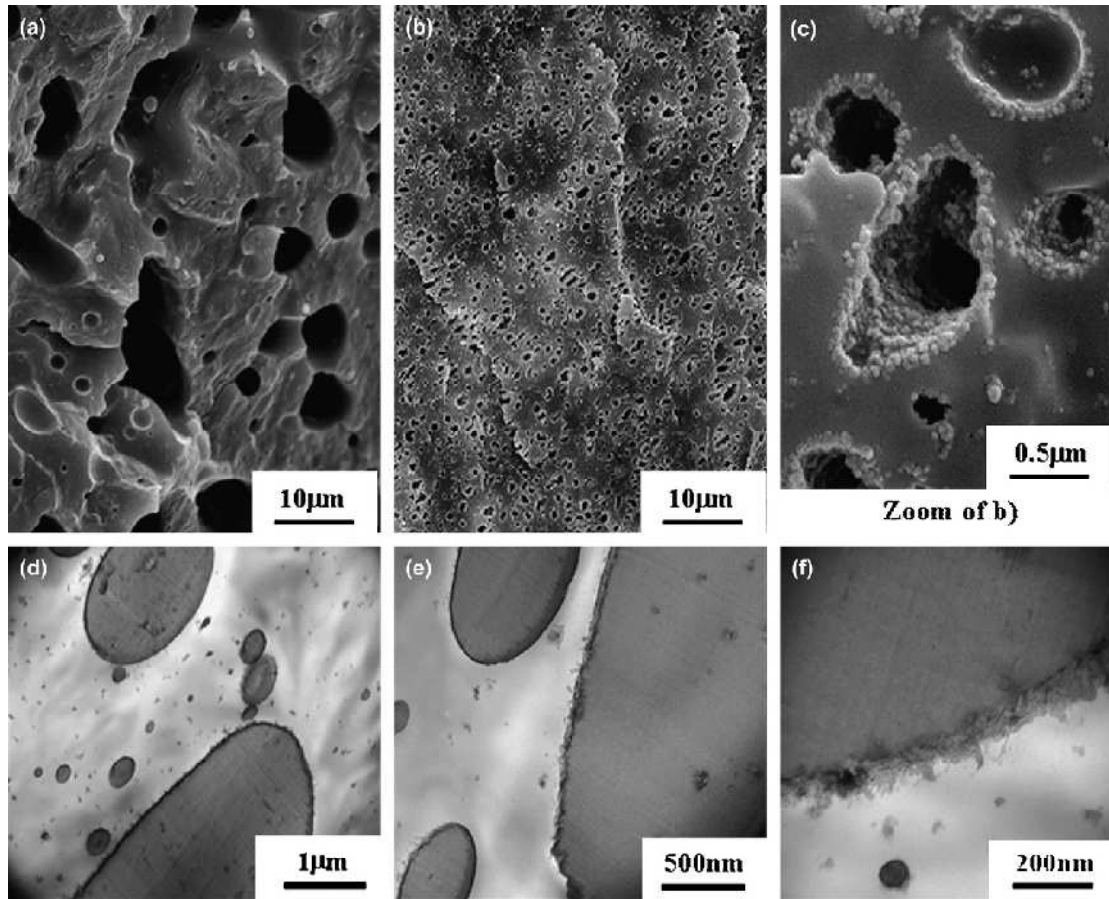
Figure 2.9: Morphology of PP/PS 70/30 blend prepared with blending procedure 1 (the three components added simultaneously in the extruder). (a) PP/PS blend without silica, (b) blend filled with 3 wt% R805 hydrophobic silica, (c) zoom of image (b) and (d)-(f) are TEM images showing the hydrophobic silica in the PP matrixvand located at the PP/PS interface. (Reused with permission from the publisher of Elias, 2007) [76]

The previous examples clearly demonstrate the vast applications that can benefit from the availability of polymer nanocomposites. However, the nanoparticle concentrations in these examples are mostly in the range below 5 wt%. For applications where compression strength is the critical design criterion, a much higher particle concentration is required. On the other hand, most existing methods for

processing porous materials are not suitable for filled/reinforced polymers, and the lack in mechanical strength of the resulting porous materials hinders their load-bearing applications. Particularly for methods dealing with a polymer solution, such as solvent casting and phase separation, one primary difficulty is caused by the segregation of the particles over the required long processing period. For other methods coping with a polymer melt, such as gas forming and melt blending, the extremely high viscosity of the filled polymer, especially at high particle loading, causes a processing difficulty. Even though solid freeform fabrication techniques such as fusion deposition modeling and laser sintering can be used to include inorganic fillers, they have a low resolution, prohibiting the production of finely structured materials. A new processing technique needs to be developed to create microporous material with high concentration of nanoparticles to provide the desired compression strength and, for scaffolding applications, sufficient bioactivity.

2.4 Micropatterned porous structures

In order for a material to be useful on a device level, it needs to be molded into desired shapes. Different from molding its solid counterpart, shaping micro porous materials, if not conducted properly, may lead to severe damage of the inner microstructure and result in loss of the required functions. Furthermore, the molding process tends to render the formation of a dense skin layer which makes the inner micropores not reachable. [37, 38]
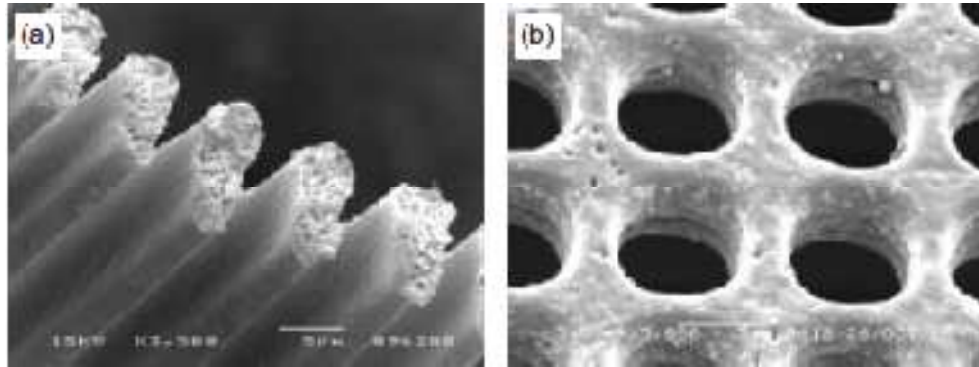
Figure 2.10: Microstructures fabricated by phase separation micro molding. (a) line pattern of 2.5 µm wide lines, made of PES (polyethersulfone). (b) microsieve made of polyimide. Both materials have a porous inner microstructure and a fully dense surface. (Reused with permission from the publisher of Vogelaar, 2003) [38]

Despite these technical difficulties, more experimental evidences have shown the superiority of micropatterned material to its flat-surface counterpart. For instance, researchers in the field of tissue engineering have found that micropatterned scaffolds are more powerful on boosting cell adhesion, proliferation, and differentiation which give cells the desired biological functions to be part of a specific tissue. Up to now, the positive effect of micropatterned scaffolds has been reported for many body tissues, such as muscle tissue [79-82], nerve tissue [83], vascular tissue [84, 85], etc. Other than desires from the field of tissue engineering, microporous materials with well-defined topography and porosity may find applications in renewable energy [86-92], microfluidics [93-95], and environment-friendly lighting sources [96, 97], as well.

To address the aforementioned technical difficulties and meet numerous application needs, researchers have yet started to explore possible solutions for the creation of high quality micropatterned porous structures. Among these proposed techniques, the phase separation micromolding method developed by Wessling and coworkers [37, 38] is one of the most popular approaches for generating micropatterned porous materials with internal pores down to submicron sizes. They cast a concentrated polymer solution onto a micropatterned mold and employed freeze drying or coagulation for extracting the solvent and forming the desired porous structure. The detailed fabricating sequence is illustrated in Fig. (2.11). This process has been used for generating micropatterned devices, such as microsieves [98, 99] and porous scaffolds [100-105], for filtration and biomedical applications. However, there are some fundamental limitations with this process. The use of a large amount of solvent leads to a slow and environmentally unfriendly process. More critically, the pore size and its distribution from this thermodynamically unstable process are hard to control. The resulting devices also tend to have a dense skin formed which is undesired in filtration and scaffolding applications.
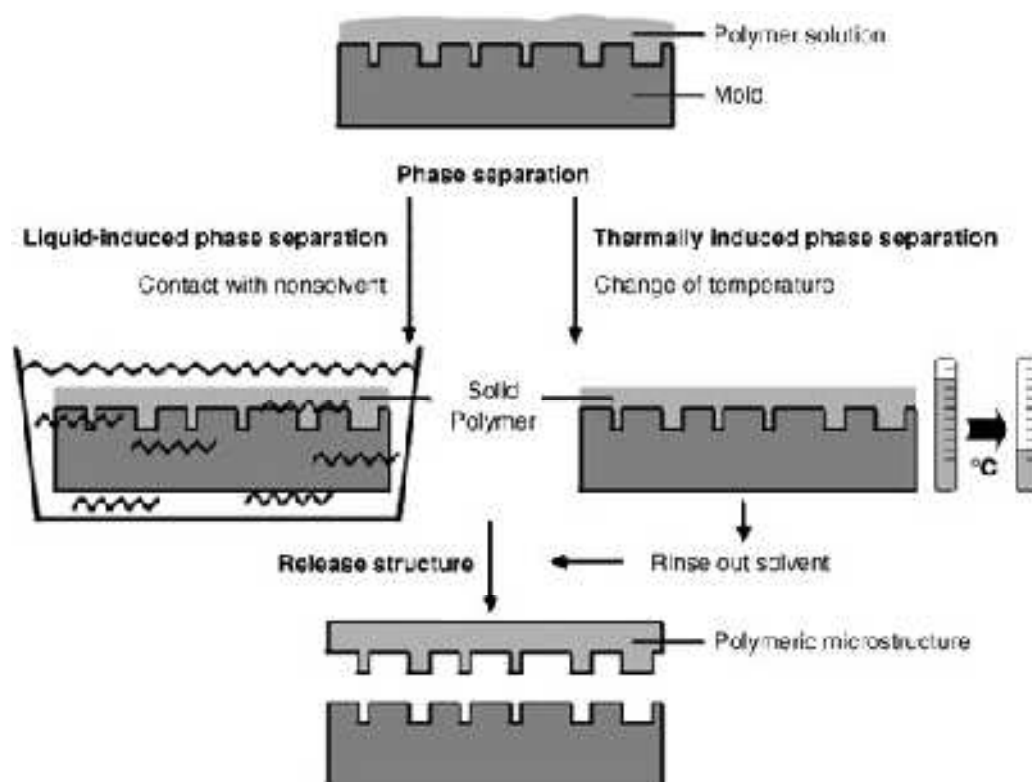
Figure 2.11: Schematic representation of the phase separation micromolding process. A layer of polymer solution is applied to a mold having a micrometer-sized relief profile on the surface. The polymer solution is solidified by either thermally induced (change of temperature of the solution) or liquid-induced phase separation (immersion in a nonsolvent). During the solidification the polymer assimilates the profile of the mold. The polymer microstructure is easily released from the mold. (Reused with permission from the publisher of Vogelaar, 2003) [37]

A desired process for creating micropatterned porous devices would be able to *in situ* control the generation of the porous structure while achieving high geometrical patterning accuracy. One versatile technique for controllable generation of a porous structure is to extract the sacrificial component from a co-continuous polymer blend. [106-114] By tuning the material and process parameters, one can generate a desired porous structure with well-defined pore size and distribution. Particularly, Yao and

coworkers [115, 116] have developed techniques for controllable growth of gradient porous structures by regulating the boundary conditions during an in-mold annealing process. In the meantime, there has also been extensive work on precision micropatterning of polymers [117, 118]. It would therefore be interesting to explore the feasibility of combining co-continuous polymer blending with precision micropatterning for creating micropatterned porous devices.

2.5 References

1. Virgilio N, Sarazin P, Favis BD, Towards ultraporous poly(L-lactide) scaffolds from quaternary immiscible polymer blends, *Biomaterials*, 31, 5719-5728, 2010.

2. Xiang ZY, Sarazin P, Favis BD, Controlling Burst and Final Drug Release Times from Porous Polylactide Devices Derived from Co-continuous Polymer Blends, *Biomacromolecules*, 10, 2053–2066, 2009.

3. Cao Y, Yin FP, Feng J, Rayatpisheh S, Chan V, Chan-Park MB, Regulating orientation and phenotype of primary vascular smooth muscle cells by biodegradable films patterned with arrays of microchannels and discontinuous microwalls, *Biomaterials*, 31, 6228-6238, 2010.

4. Sun CY, Liu SX, Liang DD, Shao KZ, Ren YH, and Su ZM, Highly stable crystalline catalysts based on a microporous metal-organic framework and polyoxometalates, *JACS*, 31, 5, 1883-1888, 2009.

5. Selvam P and Mohapatra SK, Synthesis, characterization and catalytic properties of mesoporous TiHMA molecular sieves: selective oxidation of cycloalkanes, *Microporous and mesoporous materials*, 7, 3, 137-149, 2004.

6. Girones M, Akbarsyah IJ, Nijdam, W, Van Rijn CJM, Jansen HV, Lammertink RGH, and Wessling M, Polymeric microsieves produced by phase separation micromolding, *J. Membrane Science*, 283, 411-424, 2006.

7. Bikel M, Culfaz PZ, Bolhuis-Versteeg LAM, Perez JG, Lammertink RGH, and Wessling M, Polymeric microsieves via phase separation microfabrication: process and design optimization, *J. Membrane Science*, 347, 93-100, 2010.

8. Mikos, A. G., Thorsen, A. J., Czerwonka, L. A., Bao, Y., Langer, R., Winslow, D. N., and Vacanti, J. P., Prearation and characterization of poly (L-lactic acid) foams, Polymer, 35, 1068-1077, 1994.

9. Mikos, A. G., Sarakinos, G., Leite, S. M., Vacanti, J. P., and Langer, R., Laminated three-dimensional biodegradable foams for use in tissue engineering, Biomaterials, 14, 323-330, 1993.

10. Zhang, R. Y., and Ma, P. X., Synthetic nano-fibrillar extracellular matrices with predesigned macroporous architectures, J. Biomed. Mater. Res., 52, 430-438, 2000.

11. Ma, P. X., and Zhang, R. Y., Microtubular architecture of biodegradable polymer scaffolds, J. Biomed. Mater. Res., 56, 469-477, 2001.

12. Zhang, R. Y., and Ma, P. X., Processing of polymer scaffolds: phase separation, *Methods of Tissue Engineering*, Atala, A., and Lanza, R. P., eds., Academic Press, San Diego, pp. 715-724, 2002.

13. Lo, H., Ponticiello, M. S., and Leong, K. W., Fabrication of controlled release biodegradable foams by phase separation, Tissue Eng., 1, 15-28, 1995.

14. Zhang, R. Y., and Ma, P. X., Poly(alpa-hydroxyl acids) hydroxyapatite porous composites for bone-tissue engineering. I. Preparation and morphology, J. Biomed. Mater. Res., 44, 446-455, 1999.

15. Schugens, C., Maquet, V., Grandfils, C., Jerome, R., and Teyssie, P., Polyactide macroporous biodegradable implants for cell transplantation 2. Preparation of Polyactide foams by liquid-liquid phase separation, J. Biomed. Mater. Res., 30, 449-461, 1996.

16. Zhang, R. Y., and Ma, P. X., Porous poly(L-lactic acid)/apatite composites created by biomimetic process, J. Biomed. Mater. Res., 45, 285-293, 1999.

17. Ma, P. X., and Zhang, R. Y., Synthetic nano-scale fibrous extracellular matrix, J. Biomed. Mater. Res., 46, 60-72, 1999.

18. Woo, K. M., Chen, V. J., and Ma, P. X., Nano-fibrous scaffolding architecture selectively enhances protein adsorption contributing to cell attachment, J. Biomed. Mater. Res., 67A, 531-537, 2003.

19. Chen, V. J., and Ma, P. X., Nano-fibrous poly(L-lactic acid) scaffolds with interconnected spherical macropores, Biomaterials, 25, 206-2073, 2004.

20. Zhang, R. Y., and Ma, P. X., SEM micrographs of PLLA nano-fibrous matrix with helicoidal tubular macropore network prepared from PLLA/THF solution and a helicoidal sugar fiber assembly., J. Biomed. Mater. Res., 52, 430-438, 2000.

21. Mooney, D. J., Baldwin, D. F., Suh, N. P., Vacanti, J. P., and Langer, R., Novel approach to fabricate porous sponges of poly(D, L-lactic-co-glycolic acid) without the use of organic solvents, Biomaterials, 17, 1417-1422, 1996.

22. Wang, X. X., Li, W., and Kumar, V., A method for solvent-free fabrication of porous polymer using solid-state foaming and ultrasound for tissue engineering applications, Biomaterials, 27, 1924-1929, 2006.

23. Wang, H., and Li, W., Selective ultrasonic foaming of polymer for biomedical applications, Journal of Manufacturing Science and Engineering, 130, 021004-1-021004-9, 2008.

24. Iwan Zein, Dietmar W. Hutmacher, Kim Cheng Tan, and Swee Hin Teoh, Fused deposition modeling of novel scaffold architectures for tissue engineering applications, Biomaterials,22, 1169-1185, 2002.

25. Taboas, J. M., Maddox, R. D., Krebsbach, P. H., and Hollister, S. J., Indirect solid free form fabrication of local and global porous, biomimetic and composite 3D polymer-ceramic scaffolds, Biomaterials, 24, 818-194, 2003.

26. Sherwood, J. K., Riley, S. L., Palazzolo, R., Brown, S. C., Monkhouse, D. C., Coates, M., Griffith, L.G., Landeen, L. K., and Ratcliffe, A., A three-dimensional osteochondral composite scaffold for articular cartilage repair, Biomaterials, 23(24), 4739-4751, 2002.

27. Roy, T. D., Simon, J. L., Rekow, E. D., Thompson, V. P., and Parsons, J., Performance of degradable composite bone repair products made via three-dimensional fabrication techniques, J. Biomed. Mater. Res., 66A(2), 283-291, 2003.

28. Zein, I., Hutmacher, D. W., Tan, K. C., and Teoh, S. H., Fused deposition modeling of novel scaffold architectures for tissue engineering applications. Biomaterials, 23(4),1169-1185, 2002.

29. Hutmacher, D. W., Schantz, T., Zein, I., Ng, K. W., Teoh, S. H., and Tan K. C., Mechanical properties and cell cultural response of polycaprolactone scaffolds designed and fabricated via fused deposition modeling, J. Biomed. Mater. Res., 55(2), 203-216, 2001.

30. Hutmacher, D. W., Ng, K. W., Kaps, C., Sitttinger, M., and Klaring, S., Elastic cartilage engineering using novel scaffold architectures in combination with a biomimetic cell carrier, Biomaterials, 24, 4445-4458, 2003.

31. Chu, T. M., Halloran, J. W., Hollister, S., and Feinberg, S. E., Hydroxyapatite implants with designed internal architecture, J. Mater, Sci.: Mater. Med., 12,471-478, 2001.

32. Chu, T. M., Brady, G. A., Micao, W., Halloran, J. W., Hollister, S., and Brei, D., Ceramic SFF by direct and indirect stereolithography, Materials Research Society Symposium, Materials Research Society, Pittsburgh, PA, 119-123, 1999.

33. Limanuphap, S., and Derby, B., Manufacture of biomaterials by a novel printing process, J. Mater. Sci.: Mater. Med., 13, 1163-1166, 2002.

34. Chu, T. M., Orton, D. G., Holliser, S. J., Feinberg, S. E., and Orton, D. G., Manufacturing and Characterization of 3-D hydroxyapatite implants with controlled architecture, Biomaterials,   23(5), 1283-1293, 2002.

35. Chua, C. K., Leong, K. F., and Lim, C. S., Liquid-based rapid prototyping systems, In *Rapid Prototyping-Principles and Applications,* World Scientific Publishing Co., Singapore, 35-110, 2003.

36. Levy, R. A., Chu, T. M., Halloran, J. W., Feinberg, S. E., and Hollister, S., CT-generated porous hydroxyapatite orbital floor prosthesis as a prototype bioimplant, AJNR Am. J. Neuooradiol., 18(8), 15222-1525, 1997.

37. Chu, T. M., Hollister, S., Feinberg, S. E., and Halloran, J. W., Manufacturing of biomaterial scaffolds using Image Centered Engineering methods, Keystone Symposium on Tissue Engineering. Copper Mountain, CO, 1998.

38. Porter, N. L., Pilliar, R. M., and Grynpas, M. D., Fabrication of porous calcium polyphosphate implants by solid freeform fabrication: a study of processing parameters and in vitro degradation characteristics, J. Biomed. Mater. Res., 56(4), 504-515, 2001.

39. Cooke, M. N., Fisher, J. P., Dean, D., Rimnac, C., and Mikos, A. G., Use of stereolithography to manufacture critical-sized 3D biodegradable scaffolds for bone ingrowth, J. Biomed. Mater. Res., 64B(2), 65-69, 2003.

40. Chua, C. K., Leong, K. F., and Lim, C. S., Powder-based rapid prototyping systems, In *Rapid Prototyping-Principles and Applications,* World Scientific Publishing Co., Singapore, 173-236, 2003.

41. Tan, k. H., Chua, C. K., Leong, K. F., Cheah, C. M., Cheang, P., Abu Bakar, M. S., and Cha, S. W. Scaffold development using selective laser sintering of polyetheretherketone-hydroxyapatite biocomposite blends, Biomaterials, 24(18),3115-3123, 2003.

42. Das, S., Hollister, S. J., Flanagan, C., Adewunmi, A., Bark, K., Chen, C., Ramaswamy, K., Rose, D., and Widjaja, E., Freeform fabrication of Nylon-6 tissue engineering scaffolds, Rapid Prototyping J., 9(1), 43-49, 2003.

43. Smay, J. E., Cesarano, J. III, and Lewis, J. A., Colloidal inks for directed assembly of 3-D periodic structures, Langmuir, 18, 5429-5437, 2002.

44. Landers, R., Hubner, U., Schmelzeisen, R., and Hulhaupt, R., Rapid prototyping of scaffolds derived from thermoreversible hydrogels and tailored for applications in tissue engineering, Biomaterials,   23(23), 4437-4447, 2002.

45. de Sousa, F., and Evans, J., Sintered hydroxyapatite latticework for bone substitute, J. Am. Ceram. Soc., 86, 517-519, 2003.

46. Potschke P and Paul DR, Formation of co-continuous structures in melt-mixed immiscible polymer blends, J. Macromole. Sci.-Polymer Reviews, C 43, 87-141, 2003.

47. Paul, D.R. and J.W. Barlow, POLYMER BLENDS (OR ALLOYS). Journal of Macromolecular Science-Reviews in Macromolecular Chemistry and Physics, 1980. C18(1): p. 109-168.

48. Pyun A, Bell JR, Won KH, Weon BM, Seol SK, Je JH, Macosko CW, Synchrotron X-ray Microtomography for 3D Imaging of Polymer Blends, Macromolecules, 40, 2029-2035, 2007.

49. Lopez-Barron, C.R. and C.W. Macosko, A new model for the coarsening of cocontinuous morphologies. Soft Matter, 2010. 6(12): p. 2637-2647.

50. H. Veenstra, J. V. Dam and A. P. D. Boer, Polymer, 2000, 41, 3037–3045.

51. Yuan, Z.H. and B.D. Favis, Coarsening of immiscible co-continuous blends during quiescent annealing. Aiche Journal, 2005. 51(1): p. 271-280.

52. Doi, M. and T. Ohta, DYNAMICS AND RHEOLOGY OF COMPLEX INTERFACES .1. Journal of Chemical Physics, 1991. 95(2): p. 1242-1248.

53. L. P. McMaster, Adv. Chem., 1975, 142, 43–65.

54. S. Tomotika, Proc. R. Soc. London, Ser. A, 1935, 150, 322–337.

55. E. D. Siggia, Phys. Rev. A: At., Mol., Opt. Phys., 1979, 20, 595–605.

56. Lopez-Barron, C.R. and C.W. Macosko, Characterizing Interface Shape Evolution in Immiscible Polymer Blends via 3D Image Analysis. Langmuir, 2009. 25(16): p. 9392-9404.

57. Pyun, A., et al., Synchrotron X-ray microtomography for 3D imaging of polymer blends. Macromolecules, 2007. 40(6): p. 2029-2035.

58. E. Scholten, L. M. C. Sagis and E. van der Linden, J. Phys. Chem. B, 2004, 108, 12164–12169.

59. E. Scholten, L. M. C. Sagis and E. van der Linden, Macromolecules, 2005, 38, 3515–3518.

60. W. Helfrich, Z Naturforsch, 1973, 28, 693–703.

61. Lopez-Barron, C.R. and C.W. Macosko, A new model for the coarsening of cocontinuous morphologies. Soft Matter, 2010. 6(12): p. 2637-2647.

62. Lavorgna, M., et al., Polymer blend for fuel cells based on SPEKK: Effect of cocontinuous morphology on water sorption and proton conductivity. Journal of Polymer Science Part B-Polymer Physics, 2007. 45(4): p. 395-404.

63. Huang, C.H., et al., Morphological, thermal, barrier and mechanical properties of LDPE/EVOH blends in extruded blown films. Journal of Polymer Research, 2004. 11(1): p. 75-83.

64. Jang, J.S. and D.K. Lee, Oxygen barrier properties of biaxially oriented polypropylene/polyvinyl alcohol blend films. Polymer, 2004. 45(5): p. 1599-1607.

65. Jarus, D., A. Hiltner, and E. Baer, Barrier properties of polypropylene/polyamide blends produced by microlayer coextrusion. Polymer, 2002. 43(8): p. 2401-2408.

66. Kwon, O. and D.A. Zumbrunnen, Production of barrier films by chaotic mixing of plastics. Polymer Engineering and Science, 2003. 43(8): p. 1443-1459.

67. Yeo, J.H., et al., Rheological, morphological, mechanical, and barrier properties of PP/EVOH blends. Advances in Polymer Technology, 2001. 20(3): p. 191-201.

68. Al-Saleh, M.H. and U. Sundararaj, Nanostructured carbon black filled polypropylene/polystyrene blends containing styrene-butadiene-styrene copolymer: Influence of morphology on electrical resistivity. European Polymer Journal, 2008. 44(7): p. 1931-1939.

69. Gao, J.-F., et al., Large-scale fabrication and electrical properties of an anisotropic conductive polymer composite utilizing preferable location of carbon nanotubes in a polymer blend. Composites Science and Technology, 2010. 70(13): p. 1973-1979.

70. Goldel, A., G. Kasaliwal, and P. Potschke, Selective Localization and migration of multiwalled carbon nanotubes in blends of polycarbonate and poly(styrene-acrylonitrile). Macromolecular Rapid Communications, 2009. 30(6): p. 423-429.

71. Gubbels, F., et al., Selective localization of carbon black in immiscible polymer blend- a useful tool to design electrical conductive composites. Macromolecules, 1994. 27(7): p. 1972-1974.

72. Hui, S., T.K. Chaki, and S. Chattopadhyay, Effect of silica-based nanofillers on the properties of a low-density polyethylene/ethylene vinyl acetate copolymer based thermoplastic elastomer. Journal of Applied Polymer Science, 2008. 110(2): p. 825-836.

73. Persenaire, O., et al., Tailoring of Co-Continuous Polymer Blend Morphology: Joint Action of Nanoclays and Compatibilizers. Macromolecular Chemistry and Physics, 2010. 211(13): p. 1433-1440.

74. Al-Saleh, M.H. and U. Sundararaj, Nanostructured carbon black filled polypropylene/polystyrene blends containing styrene-butadiene-styrene copolymer: Influence of morphology on electrical resistivity. European Polymer Journal, 2008. 44(7): p. 1931-1939.

75. Kelarakis, A. and K. Yoon, Optical transparency in a polymer blend induced by clay nanofillers. European Polymer Journal, 2008. 44(12): p. 3941-3945.

76. Elias, L., et al., Morphology and rheology of immiscible polymer blends filled with silica nanoparticles. Polymer, 2007. 48(20): p. 6029-6040.

77. Vogelaar L, Barsema JN, Van Rijn CJM, Nijdam W, and Wessling M, Phase separation micromolding, Adv. Mater, 15, 16, 1385-1389, 2003.

78. Vogelaar L, Lammertink RGH, Barsema JN, Nijdam W, Bolhuis-Versteeg LAM, Van Rijn CJM, and Wessling M, Phase separation micromolding: a new generic approach for microstructuring various materials, Small, 1, 6, 645-655, 2005.

79. Cao Y, Yin FP, Feng J, Rayatpisheh S, Chan V, Chan-Park MB, Regulating orientation and phenotype of primary vascular smooth muscle cells by biodegradable films patterned with arrays of microchannels and discontinuous microwalls, Biomaterials, 31, 6228-6238, 2010.

80. Papenburg BJ, Schuller-Ravoo S, Bolhuis-Versteeg LAM, Hartsuiker L, Grijpma DW, Feijen J, Wessling M, Stamatialis D, Designing porosity and topography of poly(1,3-trimethylene carbonate) scaffolds, Acta Biometerialia, 5, 3281-3294, 2009.

81. Lam MT, Clem WC, Takayama SC, Reversible on-demand cell alignment using reconfigurable microtopography, Biomaterials, 29, 1705-1712, 2008.

82. Isenberg BC, Tsuda Y, Williams C, Shimizu T, Yamato M, Okano T, Wong JY, A thermoresponsive, microtextured substrate for cell sheet engineering with defined structural organization, Biomaterials, 29, 2565-2572, 2008.

83. Yucel D, Kose GT, Hasirci V, Polyester based nerve guidance conduit design, Biomaterials, 31,1596-1603, 2010.

84. Berry CC, Campbell G, Spadiccino A, Robertson M, Curtis ASG, The influence of microscale topography on fibroblast attachment and motility, Biomaterials, 25, 5781-5788, 2004.

85. Sarkar S, Lee GY, Wong JY, Desai TA, Development and characterization of a porous micro-patterned scaffold for vascular tissue engineering applications, Biomaterials, 27, 4775-4782, 2006.

86. Zhang Y, Lu J, Shimano S, Zhou H, Maeda R, Development of MEMS-based direct methanol fuel cell with high power density using nanoimprint technology, Electrochemistry Communications, 9, 1365-1368, 2007.

87. Lozano A, Barreras F, Valino L, Marin C, Imaging of gas flow through a porous medium from a fuel cell bipolar plate by laser-induced fluorescence, Exp. Fluids, 42, 301-310, 2007.

88. Zhang Y, Lu J, Zhou HS, Itoh T, Maeda R, Application of Nanoimprint Technology in MEMS-Based Micro Direct-Methanol Fuel Cell (μ-DMFC), J. Miroelectromech. Syst., 17(4), 1020-1028, 2008.

89. Ishizuka M, Houjou H, Motokawa S, Mizuno J, Momma T, Osaka T, Shoji S, Metallization on Three Dimensions Microstructures Using Photoresist Spray Coating for Microdirect Methanol Fuel Cell, Jpn. J. Appl. Phys, 45(10A), 7944-7948, 2006.

90. Taylor AD, Lucas BD, Guo LJ, Thompson LT, Nanoimprinted electrodes for micro-fuel cell applications, J. Power Sources, 171, 218-223, 2007.

91. Kim HT, Reshentenko TV, Kweon HJ, Microstructured membranee assembly for direct methanol fuel cell, J. Electrochem. Soc., 154, 10, B1034-B1040, 2007.

92. Jang HS, Cho MW, Park DS, Micro fluidic channel machining on fused silica glass using powder blasting, Sensors, 8, 700-710, 2008.

93. Song YA, Batista C, Sarpeshkar R, Han Jongyoon, Rapid fabrication of microfluidic polymer electrolyte membrane fuel cell in PDMS by surface

patterning of perfluorinated ion-exchange resin, J. Power Sources, 183, 674-677, 2008.

94. Mekaru H, Fukushima E, Hiyama Y, Takahashi M, Thermal roller imprint on surface of Teflon perfluoroalkoxy inlet tube, J. Vac. Sci. Technol. B 27(6), 2814-2819, 2009.

95. Choi HW, Bong S, Farson DF, Lu CM, Lee LJ, Femtosecond laser micromachining and application of hot embossing molds for microfluid device fabrication, J. Laser Appl., 21, 196-204, 2009.

96. Kang MG, Guo LJ, Nanoimprinted Semitransparent Metal Electrodes and Their Application in Organic Light-Emitting Diodes, Adv. Mater., 1391-1396, 2007.

97. Rao J, L. Keeney RW, Moth-eye-structured light-emitting diodes, Optics Communications 283, 2446–2450, 2010.

98. Girones M, Akbarsyah IJ, Nijdam, W, Van Rijn CJM, Jansen HV, Lammertink RGH, and Wessling M, Polymeric microsieves produced by phase separation micromolding, *J. Membrane Science*, 283, 411-424, 2006.

99. Bikel M, Culfaz PZ, Bolhuis-Versteeg LAM, Perez JG, Lammertink RGH, and Wessling M, Polymeric microsieves via phase separation microfabrication: process and design optimization, *J. Membrane Science*, 347, 93-100, 2010.

100. Papenburg BJ, Schuller-Ravoo S, Bolhuis-Versteeg LAM, Hartsuiker L, Grijpma DW, Feijen J, Wessling M, Stamatialis D, Designing porosity and topography of poly(1,3-trimethylene carbonate) scaffolds, *Acta Biometerialia*, 5, 3281-3294, 2009.

101. Lam MT, Clem WC, Takayama SC, Reversible on-demand cell alignment using reconfigurable microtopography, *Biomaterials*, 29, 1705-1712, 2008.

102. Isenberg BC, Tsuda Y, Williams C, Shimizu T, Yamato M, Okano T, Wong JY, A thermoresponsive, microtextured substrate for cell sheet engineering with defined structural organization, *Biomaterials*, 29, 2565-2572, 2008.

103. Yucel D, Kose GT, Hasirci V, Polyester based nerve guidance conduit design, *Biomaterials*, 31,1596-1603, 2010.

104. Berry CC, Campbell G, Spadiccino A, Robertson M, Curtis ASG, The influence of microscale topography on fibroblast attachment and motility, *Biomaterials*, 25, 5781-5788, 2004.

105. Sarkar S, Lee GY, Wong JY, Desai TA, Development and characterization of a porous micro-patterned scaffold for vascular tissue engineering applications, *Biomaterials*, 27, 4775-4782, 2006.

106. Wu GZ, Xu HB, Zhou T, Morphology evolution, crystalline orientation, and thermal expansion of PA6/SEBS blends with nanolayer networks, *Polymer*, 51, 3560-3567, 2010.

107. Yu W, Zhou W, Zhou CX, Linear viscoelasticity of polymer blends with co-continuous morphology, *Polymer*, 51, 2091-2098, 2010.

108. Pyun A, Bell JR, Won KH, Weon BM, Seol SK, Je JH, Macosko CW, Synchrotron X-ray Microtomography for 3D Imaging of Polymer Blends, *Macromolecules*, 40, 2029-2035, 2007.

109. Galloway JA, Koester KJ, Paasch BJ, Macosko CW, Effect of sample size on solvent extraction for detecting cocontinuity in polymer blends, *Polymer*, 45, 423-428, 2004.

110. Zhang W, Yao DG, Zhang QW, Zhou JG, Leikes PI, Fabrication of interconnected microporous biomaterials with high hydroxyapatite nanoparticle loading, *Biofabrication*, 2, 035006, 2010.

111. Steinmann S, Gronski W, Friedrich C, Quantitative rheological evaluation of phase inversion in two-phase polymer blends with cocontinuous morphology, *Rheologica acta*, 41, 77 -86, 2002.

112. Lopez-Barron CR, Macosko CW, Characterizing Interface Shape Evolution in Immiscible Polymer Blends via 3D Image Analysis, *Langmuir*, 25(16), 9392-9404, 2009.

113. Li JM, Ma PL, Favis BD, The Role of the Blend Interface Type on Morphology in Cocontinuous Polymer Blends, Macromolecules, 35, 2005-2016, 2002.

114. Yuan ZH, Favis BD, Influence of the Efficacy of Interfacial Modification on the Coarsening of Cocontinuous PS/HDPE Blends During Quiescent Annealing, *J. Polym. Sci. Part B: Polym Phys*, 44, 711-721, 2006.

115. Yao DG, Zhang W, Zhou JG, Controllable Growth of Gradient Porous Structures, *Biomacromolecules*, 10, 1282–1286, 2009.

116. Zhang W, Deodhar S, and Yao DG, Geometrical confining effects in compression molding of co-continuous polymer blends, *Annals of Biomedical Engineering*, 38(6), 1954–1964, 2010.

117. Heckele M and Schomburg WK, Review on micro molding of thermoplastic polymers, *J. Micromechanics Microengineering*, 14, R1-R14, 2004.

118. Becker H and Gartner C, Polymer microfabrication methods for microfluidic analytical applications *Electrophoresis*, 21, 12-26, 2000.

CHAPTER 3

GROWTH OF GRADIENT POROUS STRUCTURES

3.1   Introduction

Nature is an excellent producer of multifunctional porous materials, e.g., wood, plant seeds, egg shell, bone, skin, etc. These natural porous materials typically have a gradient porous structure (GPS), meaning that the porosity is not uniform. Rather, it is distributed in space so as to maximize the overall performance of the structure. Often, the pore size continuously varies from the skin to the core, as in bone and in egg shell.[1] In bone, regions of dense "cortical" bone neighbor regions of low-density "trabecular" bone. With pore sizes decreasing from the core to the skin, bone is able to maintain a highly permeable core and yet provide an outer wall structural integrity. The increase of stiffness and strength with the reduction in pore size is understandable from both experimental and theoretical perspectives. This has been the main thrust for the recent development of microcellular polymers[2–4] for lightweight structural applications. Similarly, the avian egg shell utilizes a GPS to achieve desired mechanical performance and in the meantime a necessary permeability. From inside to outside, the pore size varies from several 100 nm to a couple of microns.[1,5] These graded pores serve for the exchange of matter between the outside and inside of the eggshell while having enough strength to prevent the shell from cracking caused by collision or impact.

The above natural materials exemplify the unique capabilities of GPSs,

particularly the ability to integrate different functions, often contradictory, and achieve an optimized design. The incorporation of GPSs in synthetic materials may lead to the creation of new functional materials for many innovative applications. In fact, a number of authors have already discussed the potential use of gradient porous structures for selective applications, including porous bearing,[1] tissue engineering scaffolds,[6,7] medical implants,[8–10] graded membranes for enhanced filtration,[11–13] graded porous beams for structural applications,[14] and functional coating materials.[15] However, very few techniques have been reported on the fabrication of synthetic materials with GPSs. Kinemuchi et al.[16] disclosed a centrifugal sintering process for creating grading porous ceramics. The grading porosity is caused by enhanced sintering using centrifugal force, which increases linearly along the radius of rotation. Centrifugal forces were also used in casting processes with powder-liquid suspensions. In particular, Biesheuvel and coworkers[11,17,18] incorporated centrifugal forces in ceramic suspension casting and created a graded porosity along the radius of rotation. Harley et al.[7] used a similar technique to cast collagen suspension in acetic acid under spinning conditions and formed a graded porosity along the spinning radius. Compared with centrifugal processing, layered approaches received more attentions.[6,8,10,13–15] Placement of layers with different porosity can be carried out by coating/deposition processes[13–15] or by layered stereolithographic methods.[8] The materials used in these processes can be powders with variable sizes,[10,13] fibers with different diameters and spacing,[6] or other layered materials with variable pore sizes.

The above known techniques for creating GPSs, however, typically have a

low resolution, prohibiting the creation of fine GPSs, and are limited to simple part geometries and shapes. In particular, the centrifugal methods are mostly suitable for cylindrical part shapes. The feeding materials in most of these processes are also limited to powders, either in dry form or in suspension. Creation of a continuously varying and spatially controlled gradient in porosity with interconnected open pores represents an additional challenge for these processing steps. In this study, a new method for controllable generation of polymeric gradient porous structures was investigated, utilizing the unique thermal flow behavior of immiscible polymer blends. By controllable variation of the temperature distribution in the blend, a spatially varied and controllable gradient in phase structure is created. After dissolution of one of the two phases, the desired porous structure of the remaining polymer is obtained. Furthermore, with this approach, continuous porous structures with interconnected open pores can be generated with appropriate selection of polymers and processing conditions.

3.2 Experimental

3.2.1 Materials

The materials used in this study were two polymers, poly(lactic acid) (PLA) and polystyrene (PS). The PLA polymer was in an extrusion grade, 4032D from Natureworks LLC. It is a semicrystalline polymer, with a glass transition temperature at 60°C and a melting temperature at 170°C, as measured by differential scanning calorimetry (DSC). The PS polymer is of an atactic grade, from Dow Chemical, with a

glass transition temperature at approximately 108°C, measured by DSC. Both polymers have a thermal degradation temperature above 300°C in the nitrogen environment, judged by thermal gravimetric analysis (TGA). The number average molecular weights for the two polymers were estimated from melt viscosities; they are 330,000 g/mol and 590,000 g/mol, for PLA and PS, respectively. Both polymers were obtained in a pellet form from the suppliers.

3.2.2 *Blending*

The PLA/PS mixture (50% by 50% in weight) was blended in a Brabender Intelli-Torque Rheometer. The torque Rheometer head was mounted with Sigma blades capable of tumbling and distributive mixing. A compounding temperature of 200°C and a mixing speed of 60 rpm were used during the blending process. A mixing time of 10 min was employed to ensure a uniform chamber temperature prior to blending. The achievement of homogenous blend morphology inside the chamber was established by the development of a constant blending torque**.** A homogenous PLA/PS blend was obtained at the end of 10 min. The as-mixed blend was immediately scraped out of the chamber in molten state and quenched in tap water.

3.2.3 *Annealing with temperature gradients*

In this exploratory study, three different types of thermal boundary conditions were used to generate three different types of temperature gradient during annealing, as shown in Fig. 3.1. In the first case, a temperature difference is imposed between upper and lower platens, between which a polymer blend is annealed. In the second case, a temperature gradient is applied around a corner of a blend sample with a square cross-section. In the third case, a heated pin of a diameter of 1 mm is inserted into a room-temperature blend disk to create a radial temperature gradient. All these annealing experiments were conducted on a hydraulic press with heated platens. In all three cases, the hot platen was set to 200°C and the cold platen was left at room temperature with tap water cooling. The free surfaces on the samples were exposed to natural air convection in the ambient environment. During annealing, some blend material was squeezed out in the lateral direction. Only a small amount of contact force was applied in order to minimize the lateral out-squeeze.
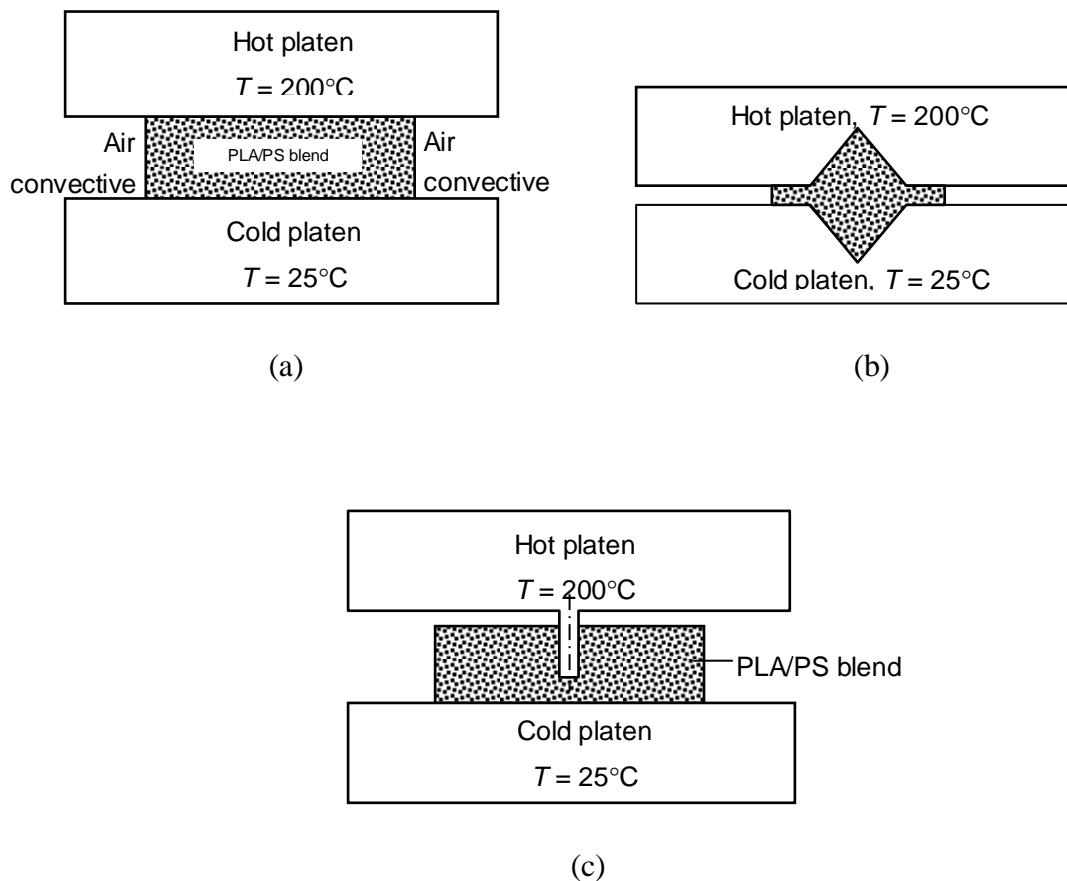
Figure 3.1: Different thermal boundary conditions for creation of different thermal gradients in annealing: (a) temperature difference between two flat surfaces, (b) temperature gradient around a sharp corner, and (c) temperature gradient around a hole on the blend.

3.2.4 Characterizations

The rheological properties of the two polymers were characterized on a rotational rheometer (Model: AR2000EX, TA Instruments). The thermal properties were characterized on a DSC unit (Model: Q200, TA Instruments) and a TGA unit (Model: Q5000-IR, TA Instruments). After blending and controlled annealing, the sample was quenched in tap water. The polystyrene phase in the cooled blend was extracted with

cyclohexane performed in a solvent bath for 7 days. The weight loss was measured to calculate the extent of continuity of the PS phase. The cross-sections of the remaining porous samples were sputter-coated with gold and then imaged using scanning electron microscopy (SEM) on a Hitachi S-800 SEM unit.

3.3 Results and Discussion

Two highly immiscible polymers can form a co-continuous blend structure under appropriate materials and processing conditions. One most frequently used empirical relation for predicating the onset of phase inversion were first proposed by Paul and Barlow[20] and later generalized by Miles and Zurek[21]:

$$\frac{\phi_1}{\phi_2} = \frac{\eta_1(\dot{\gamma})}{\eta_2(\dot{\gamma})}, \tag{3.1}$$

where $\eta_i(\dot{\gamma})$ is the viscosity of component i at blending conditions and ϕ_i is its volume fraction at which phase inversion occurs. For binary blends, the onset for forming a co-continuous phase structure is in a range of approximately 15-20% volume concentration of minor component. However, for blends with relatively low interfacial tension, this onset could be significantly low if a fibrous morphology can be formed. More complex criteria for phase inversion considering not only the viscosity ratio but also interfacial tension and mixing conditions have also been proposed[22]. These models suggested that co-continuous phase structures can be formed in a highly immiscible

polymer blend under a wide range of materials and processing conditions.

Due to the presence of interfacial tension, the co-continuous phase structure of an immiscible binary blend coarsens upon quiescent annealing at a temperature above the melting temperatures of both polymer components. Experimental studies[23, 24] indicated that the phase size growth rate is constant at a constant annealing temperature, irrespective of the phase size. Generally speaking, the phase size growth rate is related to the volume fraction, the initial phase structure, the interfacial tension, and the zero-shear viscosity of the blend. From dimensional analysis, it can be shown that this growth rate, k, should be linearly dependent on the ratio of interfacial tension to blend viscosity,

$$k \sim \frac{\gamma}{\eta_e},$$

(3.2)

where γ is interfacial tension and η_e is equivalent blend viscosity. A similar relation has been derived by Yuan and Favis.[24] Since the polymer blend viscosity is sensitive to temperature changes, the phase size growth rate is expected to be strongly dependent on the annealing temperature. For example, the experimental results by Yuan and Favis showed that average phase size growth rate of a PS/PE blend increased by more than two folds when the annealing temperature increased from 180°C to 200°C.[24]
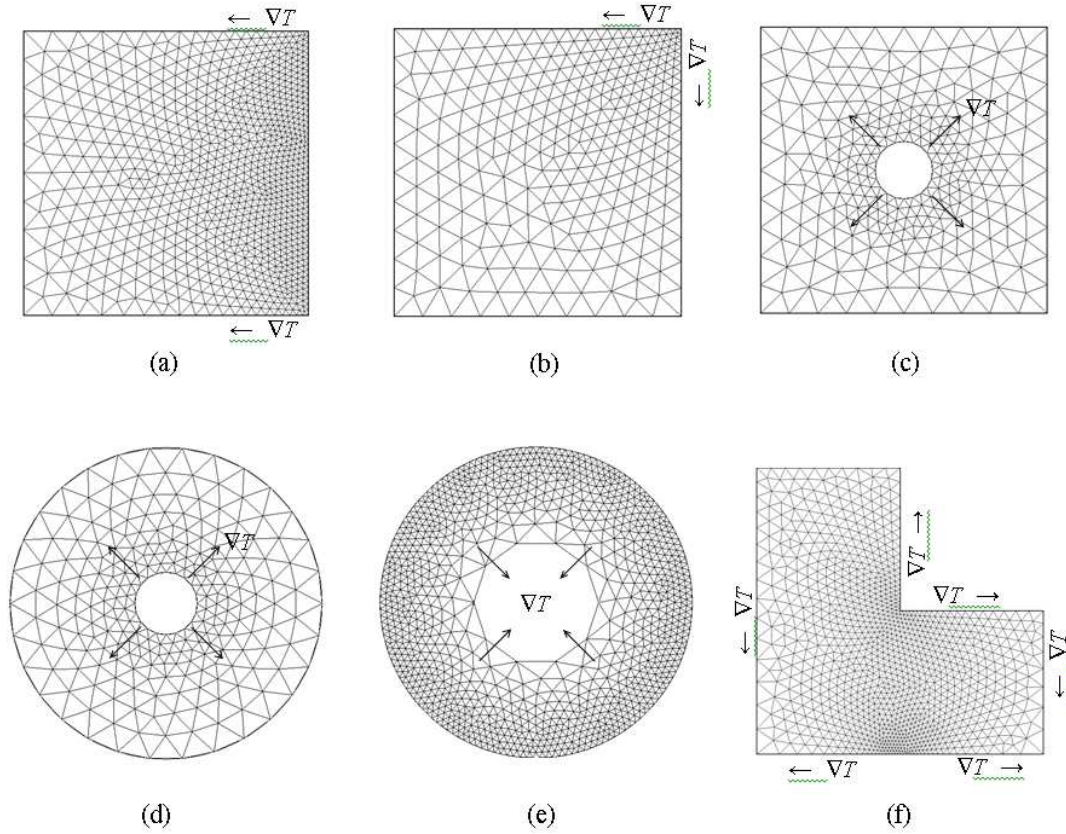
Figure 3.2: Gradient porous structures created from different thermal gradients: (a) thermal gradient in one direction, (b) thermal gradient in two directions, (c) converging thermal gradient in a 2-D square domain, (d) converging thermal gradient in an axisymmetric domain, (e) diverging thermal gradient in an axisymmetric domain, and (f) spatially distributed thermal gradient.

Since the phase size growth rate predominately depends on the annealing temperature, one can produce a spatially varied phase structure if a spatially varied thermal field can be created during annealing. This means that a gradient temperature distribution during annealing can lead to a gradient phase structure. A few examples are illustrated in Fig. 3.2. ∇T is a temperature gradient. Arrows denote the directions in which a positive temperature gradient is imposed; that is, the temperature increases along the arrow direction. For example, in Fig. 3.2.a, the temperature increases along

the arrow direction from right to left. This gives rise to an increased phase size growth rate along the same direction. Therefore, the phase structure coarsens more on the left side than on the right side, resulting in a gradient phase structure. Other examples of gradient thermal fields and gradient phase structures are shown in Fig. 3.2.b-3.2.f. These different thermal fields result in different phase structures, but all with a gradient in phase size. Note that these gradient thermal fields can be realized by establishing appropriate thermal boundary conditions on the material to be annealed. For example, the thermal field in Fig. 3.2.d can be created by applying a lower temperature on the inner circular boundary and a higher temperature on the outer circular boundary. In reality, such boundary conditions can be readily established during annealing experiments. For the same sample geometry, the boundary conditions can also be readily adjusted if a different phase structure is needed. For example, the sample shown in Fig. 3.2.e has the same overall sample geometry as that in Fig. 3.2.d. However, the gradient of thermal field is reversed, thus creating a different pore size gradient. Note that such a versatility typically lacks in existing methods for porous material processing. In particular, the methods based on centrifugal forces results in one type of phase structure gradient. Further these known methods are mostly limited to axisymmetric sample geometries.

The rotational rheometry was operated under the small-strain oscillatory shear mode with a strain amplitude of 0.01. Fig3.3 shows the dependency of the complex viscosity of PLA and PS on the angular frequency at two different testing temperatures. Using the well-known Cox-Merz rule[18] for shear viscosity, one can convert angular

frequency equivalently to shear rate. From the resulting shear rate dependency, it is clearly seen that both polymers are highly pseudoplastic, with viscosity decreasing with increase of shear rate. Two types of viscosity are important in the current study. First, the viscosities and their ratio at the processing shear rate during batch mixing are major factors affecting the phase structure of the blend. For example, the phase inversion can be related to the viscosity ratio.[20,21] Second, the zero-shear viscosities determine the coarsening rate during annealing; in general, the phase size growth rate is inversely proportional to the equivalent viscosity of the blend.[22,24] The batch mixing step was performed at a mixing speed of 60 rpm and a temperature of 200°C. The shear rate at this mixing speed with a rotor diameter of 35.5 mm was estimated to be 95 s^{-1}. The viscosity ratio of PLA over PS in this case is 0.7, calculated from the data in Fig. 3.3. For a 50/50 wt% PLA/PS blend used in this study, this viscosity ratio would result in a co-continuous phase morphology. Different from mixing under external forces, phase coarsening during annealing is a spontaneous process, driven by the interfacial tension. The deformation rate involved in annealing is typically much smaller than in mixing. Thus, the zero-shear viscosity is the relevant viscosity for predicting the phase coarsening process. From Fig. 3.3, it is seen that the zero-shear viscosity for both PLA and PS is sensitive to temperature changes. When temperature changes from 200 to
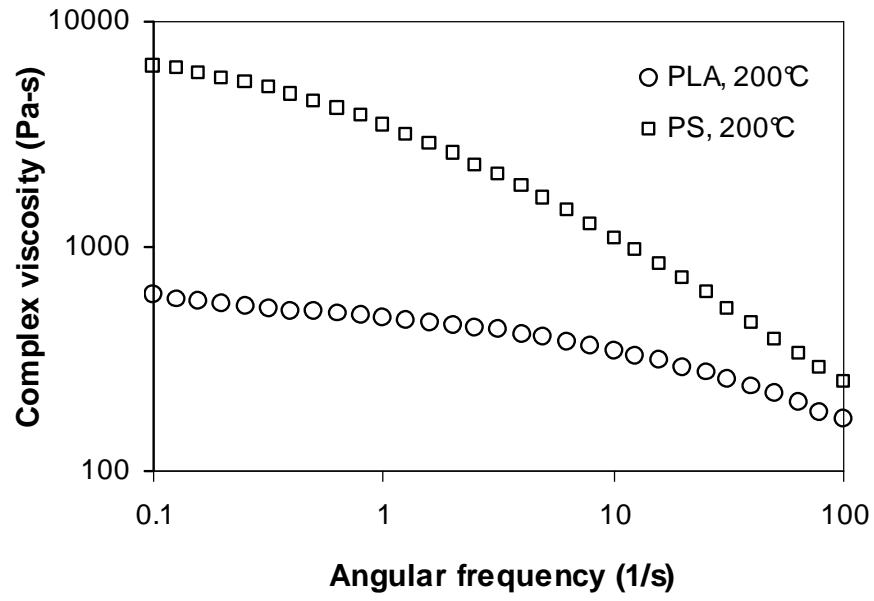
(a)
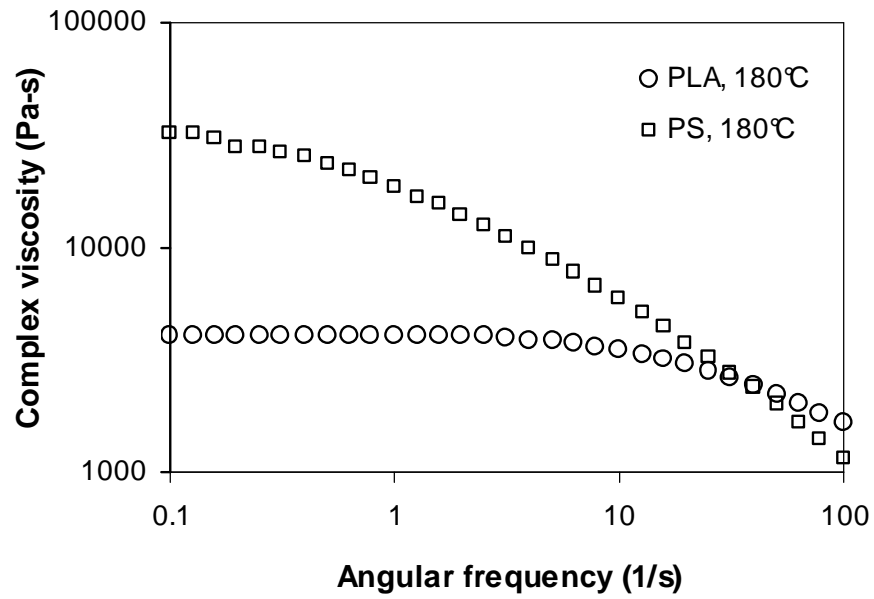
(b)

Figure 3.3: Complex viscosity of PLA and PS at different temperatures: (a) 200°C and (b) 180°C.

180°C, the zero-shear viscosity increased by a factor of 6.5 for PLA and a factor of 5 for

PS. This strong dependency on temperature indicates that the phase size coarsening rate can be effectively varied by applying a relatively small temperature gradient during annealing.

Fig. 3.4 compares the phase structures before and after isothermal annealing at 180°C for 2 min. In both cases, the PS phase was solvent extracted, leaving a porous PLA structure. Before solvent extraction, the samples were smoothly cut with a sharp blade. This left a flat surface in the final porous structure, making it easier for phase size comparison. In both cases, a well-defined continuous porous PLA structure can be clearly seen in the SEM micrograph. Comparison of the sample weight before and after solvent dissolution showed that nearly 100% PS was extracted, suggesting the existence of a continuous PS phase in both cases. Therefore, the blend before and after annealing both had a co-continuous phase structure. Aside from these findings, the comparison more importantly shows the significant effect of the annealing temperature. After annealing for only 2 min, the phase size grew much coarser, at least twice larger than the original phase size. Fig. 3.5 shows a porous PLA structure formed after more extensive annealing at 180°C for 30 min. The sample was brittle fractured after extraction of the PS phase. The phase size resulting from this prolonged annealing was more than 20 times larger than the original one. It is noteworthy to report that, at this large phase size, a well-defined continuous porous PLA structure still persisted.

(a)   (b)
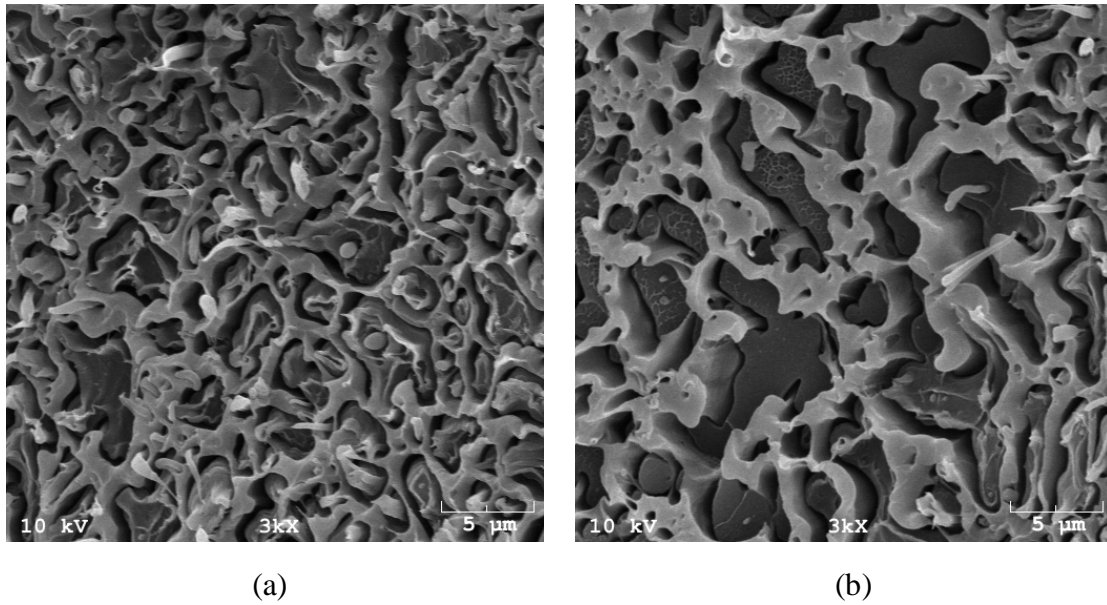
Figure 3.4: Phase structures before and after annealing: (a) after mixing and (b) after annealing for 2 min at 180°C.
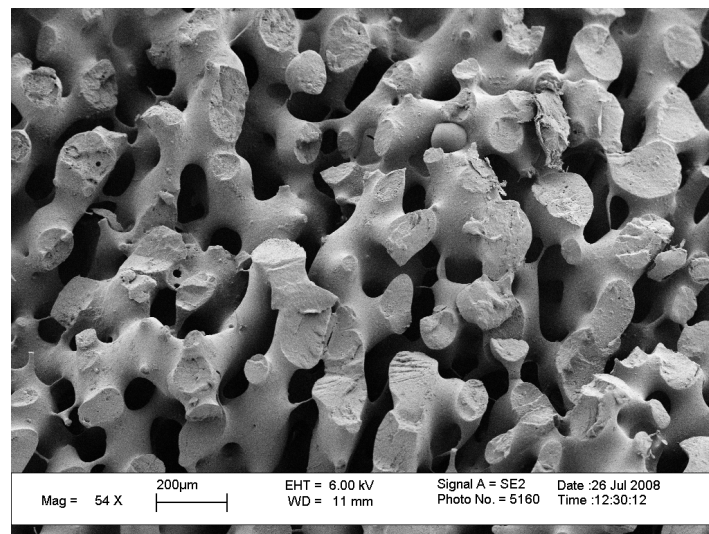
Figure 3.5: Porous PLA structures formed from an immiscible PS/PLA blend after annealing at 180°C for 30 min.

The gradient porous structures created from the non-isothermal annealing experiments, as described in Fig. 3.1, with controlled thermal boundary conditions are

shown in Fig. 3.6-3.8. At each thermal boundary condition, the experiment was repeated for at least three times. The obtained morphology was found to be consistent from run to run. The structure shown in Fig. 3.6 was obtained from the annealing experiment of a 6 mm thick blend plate between two parallel platens with an imposed temperature difference. Three different locations are indicated in Fig. 3.6.a, and the resulting cross-sectional structures along the direction perpendicular to the temperature gradient are given in Fig. 3.6.b-6.d. After an annealing time of 30 min, large pores with a size around 200 μm were formed on the hot platen side (left side in Fig. 3.6), while the pore size on the cold platen side were left unchanged, with the same phase size around several microns as that in the as-mixed blend. In between the two platens, a gradient in phase size
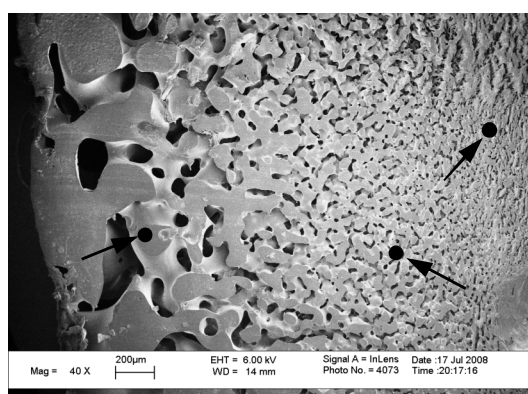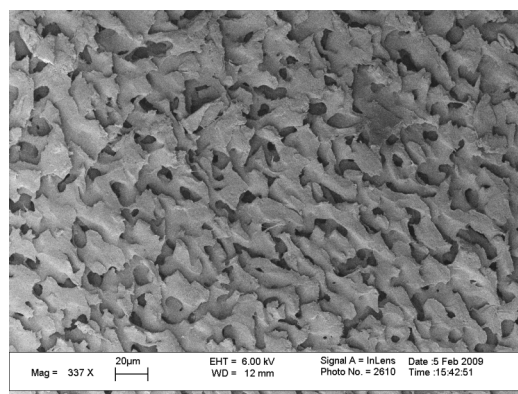
(a)   (b)
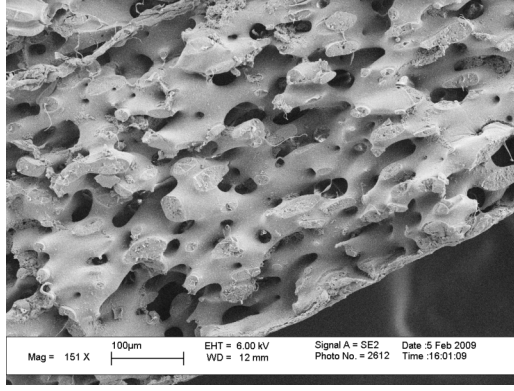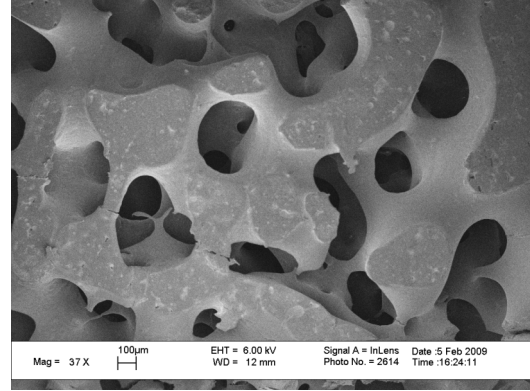
(c)   (d)

Figure 3.6: Gradient porous structure from 1-D thermal gradient: (a) overall structure, (b) cross-sectional structure at location A, (C) cross-sectional structure at location B, and (d) cross-sectional structure at location C.

can be clearly seen. For this simple 1-D case, the distribution of pore size can be well correlated to the temperature distribution. The melting temperature of the PLA component is 170°C, below which no coarsening effect would occur during annealing. The distance from the hot platen corresponding to this temperature can be analytically calculated to be $0.17H$, where H is the plate thickness. In the current case, this distance would be 1 mm; that is, after a distance of 1 mm from the hot platen, no significant coarsening effect would be expected. This calculation, in general, agrees with the experimental observation in Fig. 3.6.

200 µm
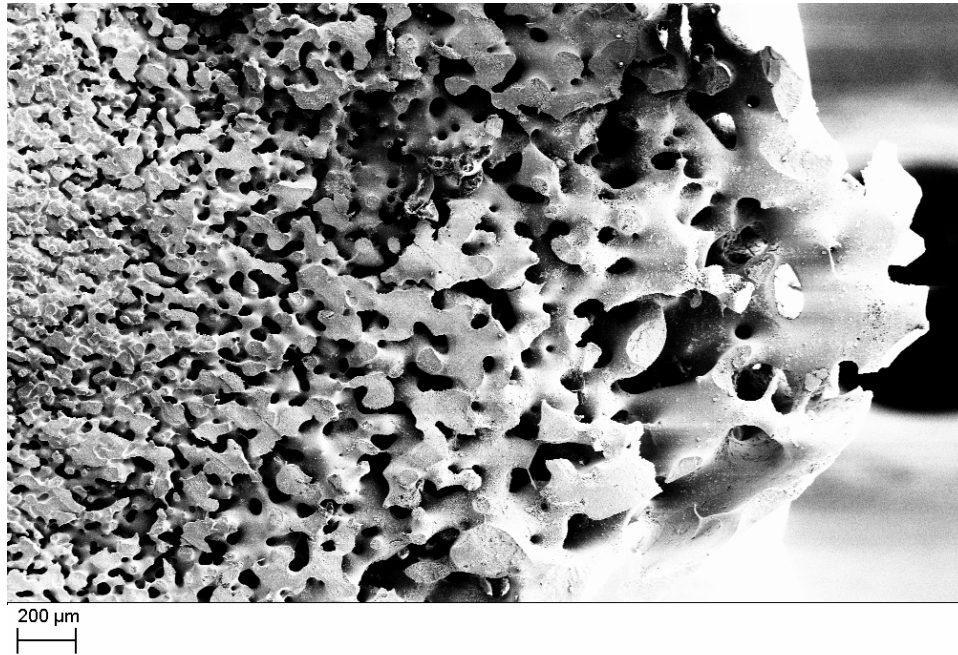
Figure 3.7: Pore gradient in two directions around an exterior corner.

The structure in Fig. 3.7 was obtained from the annealing condition described in Fig. 1.b. For this more complex case, an analytical solution of temperature field would be difficult to obtain, but a 2-D distribution of phase size can be clearly seen in the experimental phase structure. The largest pores were present right at the corner, where the highest temperature, close to the hot platen temperature, was expected. Away from the corner, the pore size decreased along both edges with a relatively large gradient in pore size. This again can be qualitatively related to the unique temperature distribution in the vicinity of the corner in this annealing experiment.

1 mm
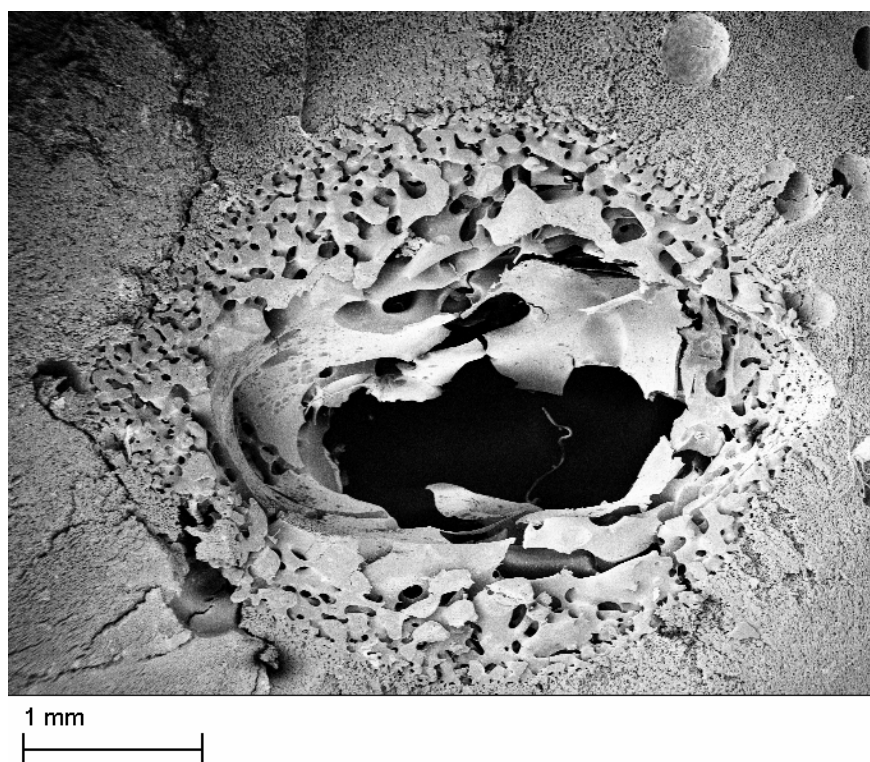
Figure 3.8: Gradient of pore size toward a center hole.

Similarly, the gradient structure shown in Fig. 3.8 can be correlated with the unique temperature field resulting from the annealing setup in Fig. 1.c. The high-temperature pin attached to the hot platen gave rise to a negative temperature gradient in the radial direction. This, in turn, resulted in the decrease in the coarsening rate in the radial direction and consequently a radial gradient structure. The porosity and interconnectivity of pores in the above porous structures were evaluated by weighing the samples before and after solvent extraction of the sacrificial phase. The results showed that nearly 100% PS was removed after solvent extraction, indicating that interconnected pores were presented in the gradient porous structure.

3.4   Conclusions

This exploratory study demonstrated the feasibility of producing gradient porous structures via controllable nonisothermal annealing of immiscible polymer blends under designed thermal boundary conditions. With a model blend of PLA and PS, three types of gradient porous structure were created, each resulting from a unique temperature field incorporated in the annealing setup. The pore size resulting from these annealing experiments varied from several microns to several hundreds of microns, distributed in the space and interconnected through a co-continuous structure. The unique gradient in pore size in each case was corrected with the unique temperature field developed in each special annealing setup. A positive temperature gradient resulted in a growth of pore size in this direction. With further understanding of this novel process in a more quantitative manner, involving parametric experiments and modeling of the thermal and two-phase flow problem, more complex porous structures with designed gradient in pore size can be produced.

3.5   References

1. Zhang, J. Z.; Wang J. G.; Ma, J. J. *Journal of Zhejiang University Science* **2005**, *6A*, 1095–1099.

2. Kumar, V. *Celluar Polymers* **1993**, *12*, 207–223.

3. Suh, N. P. *Macromolecular Symposia* **2003**, *201*, 187–201.

4. Gong, S.; Yuan, M.; Chandra, A.; Winardi, A.; Osorio, A.; Turng, L. S. *International Polymer Processing* **2005**, *20*, 202–214.

5. Kitimasak, W.; Thirakhupf, K.; Moll, D. L. *Science Asia* **2003**, *29*, 95–98.

6. Woodfield, T. B. F.; van Blitterswijk, C. A.; de Wijn, J.; Sims, T. J.; Hollander, A. P.; Hollander, A. P. *Tissue Engineering* **2005**, *11*, 1297–1311.

7. Harley, B. A.; Hastings, A. Z.; Yannas, I. V.; Sannino, A. *Biomaterials* **2006**, *27*, 866–874.

8. Wang, H.; Johnston, S. R.; Rosen, D. W. In *The Seventeenth Solid Freeform Fabrication Symposium* **2006**, Austin, TX, pp. 111-123.

9.   Pompe, W.; Worch, H.; Epple, M.; Friess, W.; Gelinsky, M.; Greil, P.; Hempel, U.; Scharnweber, D.; Schulte, K. *Materials Science and Engineering* **2003**, *A362*, 40–60.

10. Beletskii, B. I.; Mastryukova, D. S.; Vlasova, E. B. *Glass and Ceramics* **2003**, *60*, 270–273.

11. Biesheuvel, P. M.; Breedveld, V.; Higler, A. P.; Verweij, A. *Chemical Engineering Science* **2001**, *56*, 3517–3525.

12. Darcovich, K.; Cloutier, C. R. *Journal of the American Ceramic Society* **1999**, *82*, 2073–2079.

13. Meulenberg, W. A.; Mertens, J.; Bram, M.; Buchkremer, H. P.; Stover, D. *Journal of the European Ceramic Society* **2006**, *26*, 449–454.

14. Pollien, A.; Conde, Y.; Pambaguian, L.; Mortensen, A. *Materials Science and Engineering A* **2005**, *404*, 9–18.

15. Schulz, U.; Peters, M.; Bach, F. W.; Tegeder, G. *Materials Science and Engineering* **2003**, *A362*, 61–80.

16. Kinemuchi, Y.; Watari, K.; Uchimura, S. *Acta Materialia* **2003**, *51*, 3225–3231.

17. Biesheuvel, P. M.; Nijmerijer, A.; Verweij, H. *A.I.Ch.E. Journal* **1998**, *44*, 1914–1922.

18. Biesheuvel, P. M.; Verweij, H. *Journal of the American Ceramic Society* **2000**, *83*, 743–749.

19. Cox, W. P.; Merz, E. H. *J. Polym. Sci.* 1958, *28*, 619–622.

20. Paul, D. R.; Barlow, J. W. *Polymer Reviews* **1980**, *18*, 109-168.

21. Miles, I. S.; Zurek, A. *Polym. Eng. Sci.* **1988**, *28*, 796-805.

22. Willemse, R. C.; Posthuma de Boer, A.; van Dam, J.; Gotsis, A. D. *Polymer* **1997**, 39, 5879-5887.

23. Yuan, Z. H.; Favis, B. D. *Biomaterials* **2004**, 25, 2161-2170.

24. Yuan, Z. H.; Favis, B. D. *AIChE Journal* **2005**, 51, 271-280.

CHAPTER 4

GEOMETRICAL CONFINING EFFECTS IN COMPRESSION MOLDING OF CO-CONTINUOUS POLYMER BLENDS FOR SCAFFOLD APPLICATIONS

4.1   Introduction

Porous materials are extensively used as scaffolding templates in tissue engineering. A controllable morphology is highly desired in the scaffold structure for engineering the permeation profile and the biodegradation rate. Various techniques, including solvent casting/particulate bleaching[1-4], fiber bonding (nonwoven meshes)[5-7], phase separation/emulsification[8-12] , gas foaming[13-19], co-continuous melt blending[20-23], and rapid prototyping/solid freeform fabrication[24-28], have been developed to produce porous materials for tissue engineering applications. Among these methods, the polymer melt blending approach[20-23] is an extremely versatile method for producing co-continuous porous structures with controllable pore sizes. In particular, Favis and co-workers[26,27] have used quiescent annealing to coarsen the blend phase and create polymer scaffolds with varied pore sizes for tissue engineering applications. Recently, the authors[25] also demonstrated a method for controlling the pore size distribution through gradient thermal fields.

For biomedical applications, scaffolds with well-defined external shapes are often needed. This requires the blend to be molded into the designed shape and

annealed inside the mold cavity. It is understood that, due to the so-called boundary effects, the material in contact with the mold wall can undergo special kinematic and dynamic conditions. The resulting phase structure near the mold wall may be largely different from that in the bulk. While numerous studies have been performed to elucidate the thermal annealing effects on the bulk structure, such boundary effects from geometrical confinement are little understood. From fundamental point of view, there are several possible physical mechanisms causing special interactions between the polymer blend and the confining boundary surface. First, the individual polymer components may stick to the wall due to the so-called no-slip wall condition. This can reduce the mobility of the polymer components in contact with the mold surface, resulting in a reduced coarsening rate in the vicinity of the wall. Second, the state of the ternary interface among the two polymer components and the mold surface could affect the phase evolution near the wall. This is understandable since the blend annealing process is determined by the competition between the interfacial tension and the viscous stress. These boundary effects are expected to exert more influences as the surface area/volume ratio increases. In particular, strong size effect may arise when the size of the mold cavity reduces to a level comparable to that of the growing polymer domain. The spatial limitation in this case can strongly influence the growth of the phase structure. Besides these aforementioned boundary and size effects, the deformation imposed by the molding step may result in a morphological change of the blend. For example, experimental results have indicated formation of a thin dense layer at the mold surface after compression molding.[29]

In this research, possible effects from geometrical confinement during in-mold annealing were explored. A 50/50 wt% poly(lactic acid)/polystyrene (PLA/PS) blend was compression molded and annealed between two parallel mold plates. Different conditions for geometrical confinement, including varied gap size and compression ratio, as well as modified surface properties, were employed. Understanding the influences from these geometrical and boundary effects may lead to the development of more capable processes for innovative porous materials.

4.2 Materials and Methods

4.2.1 Materials

Poly(lactic acid) (PLA) and polystyrene (PS) were used in this study to form a co-continuous blend for geometrically confined annealing. The PLA is in an extrusion grade, 4032D from Natureworks LLC. It is a semicrystalline polymer, with a glass transition temperature at 60°C and a melting temperature at 170°C, as measured by differential scanning calorimetry (DSC). The PS is of an atactic grade, STYRON® 675 from Dow Chemical, with a glass transition temperature at approximately 108°C, measured by DSC. Both polymers have a thermal degradation temperature above 300°C in the nitrogen environment, judged by thermal gravimetric analysis (TGA). The number average molecular weights for the two polymers were estimated from melt viscosities; they are 330000 g/mol and 590000 g/mol, for PLA and PS, respectively. Both polymers were obtained in a pellet form from the suppliers.

4.2.2 Blending

The PLA/PS mixture (50% by 50% in weight) was blended in a Brabender Intelli-Torque Rheometer. The torque rheometer head was mounted with Sigma blades capable of tumbling and distributive mixing. A compounding temperature of 200°C and a mixing speed of 30 rpm were used during the blending process. The shear rate at this mixing speed with a rotor diameter of 35.5 mm was estimated to be 47.5 s^{-1}. To minimize the hydrolysis of the added PLA under the high compounding temperature, both PLA and PS are dried in an oven at 90°C for 12 hr and blended immediately with nitrogen protection. The achievement of homogeneous blend morphology inside the chamber was established by the development of a constant blending torque. A homogeneous PLA/PS blend was obtained at the end of 10 min. The as-mixed blend was immediately scraped out of the chamber in molten state and quenched in tap water. The cooled blend was dried in an oven at 90°C for 4 hr and stored in a desiccator before next step experiment.

4.2.3 Annealing under Geometric Confinement

In this study, two experimental procedures, contact annealing and compression annealing, were used to study the effects of geometrically confined annealing, as shown in Fig. 4.1. The PLA/PS blends from batch mixing were cut into samples with different thickness from 0.5 mm to 12 mm. In contact annealing (Fig. 4.1.a), the sample was placed between two heated stainless steel plates, with small contact force applied to ensure a full contact between the sample and the plates and yet avoid

significant compression of the sample. The resulting compression ratio, defined by the ratio between the original thickness over the compressed thickness, in this case is nearly one. Different annealing temperatures of 180°C and 200°C and varied gap thicknesses from 0.5 to 2.5 mm were employed in the contact annealing experiment. In compression annealing, a positive compression was applied to the sample, as shown in Fig. 4.1.b. A large compression ratio of 6, obtained by compressing the sample thickness from 12 mm to 2 mm, and a fixed annealing temperature of 200°C were used for all compression annealing experiments.

To separately study the compression effect from the annealing effect, two types of samples were collected and compared. For first type, samples were collected immediately after compression and quenched in tap water. For the second type, samples were allowed to anneal for 20 min between the plates before quenching.
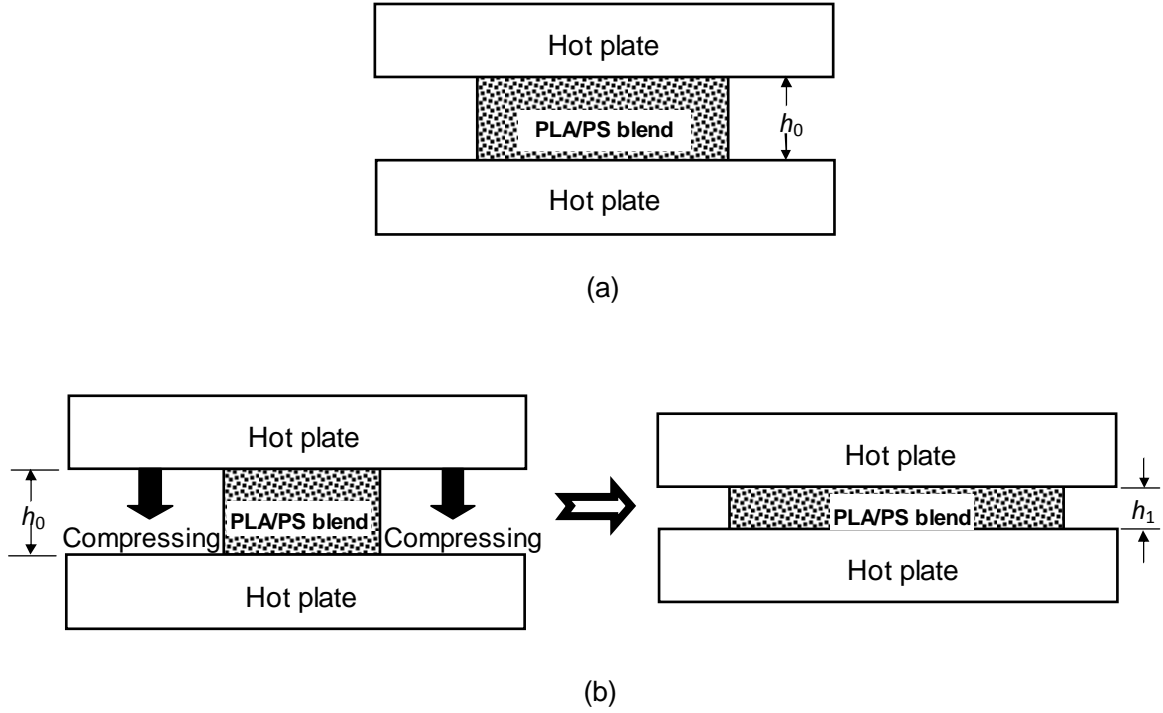
Figure 4.1: Different experimental procedures for geometrically confined annealing: (a) contact annealing with a gap size of h_0; and (b) compression annealing with a compression ratio of h_0/h_1.

To investigate the effects of mold surface properties on the annealing behavior under geometrical confinements, different mold surface materials were used. Besides stainless steel surfaces, poly(tetra fluoroethylene) (PTFE) surfaces were created by placing a thin PTFE film, 50 µm in thickness, over the metallic mold surface. In addition, silicon oil (a low-molecular-weight linear poly(dimethyl siloxane) (PDMS)) was used as a coating material for producing lubricated mold surfaces.

4.2.4   Characterizations

The rheological properties of the two polymers were characterized on a rotational rheometer (Model: AR2000EX, TA Instruments). After blending and controlled annealing, the sample was quenched in tap water. All processed samples were cut with a sharp blade and immersed in cyclohexane for 7 days to selectively extract the PS phase. The remaining porous samples were sputter-coated with gold and then imaged using scanning electron microscopy (SEM) on a LEO 1550 SEM unit. The contact angles of PLA and PS on stainless steel surface were measured with a goniometer at room temperature (Rame-Hart Co., Netcong, NJ).

4.3   Results and Discussion

The parallel plate rheometry was operated under small-strain oscillatory shear mode with strain amplitude of 0.01. Fig. 4.2 shows the dependency of the complex viscosity of PLA and PS on the angular frequency at two different testing temperatures, 180 and 200°C. Using the well-known Cox-Merz rule[30] for shear viscosity, one can convert angular frequency equivalently to shear rate. From the resulting shear rate dependency, it is clearly seen that both polymers are highly pseudoplastic, with viscosity decreasing with increase of shear rate.
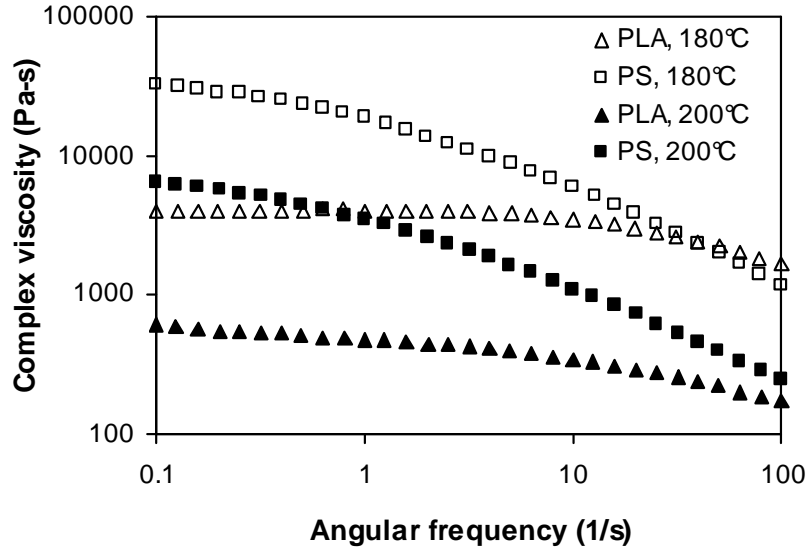
Figure 4.2: Complex viscosity of PLA and PS at 180°C and 200°C.

Two types of viscosity are important in the current study. First, the viscosities and their ratio at the processing shear rate during batch mixing are major factors affecting the phase structure of the blend. For example, the phase inversion can be related to the viscosity ratio.[28] Second, the zero-shear viscosities determine the coarsening rate during annealing; in general, the phase size growth rate is inversely proportional to the equivalent viscosity of the blend.[26,27] Different from mixing under external forces, phase coarsening during annealing is a spontaneous process, driven by the interfacial tension. The deformation rate involved in annealing is typically much smaller than in mixing. Thus, the zero-shear viscosity is the relevant viscosity for predicting the phase coarsening process. From Fig. 4.2, it is seen that the zero-shear viscosity for both PLA and PS is sensitive to temperature changes. When temperature changes from 200 to 180°C, the zero-shear viscosity increased by a factor of 6.5 for PLA

and a factor of 5 for PS. This strong dependency on temperature indicates that the phase

coarsening rate during annealing can be effectively varied by controlling the annealing

temperature.

The processing conditions, including mixing temperature, r.p.m., and mixing

time, were optimized to obtain a 50/50 wt% PLA/PS blend with a co-continuous

structure of a desired pore size. At a given mixing temperature, the r.p.m was found to be

the more important factor affecting the phase size. At 200°C and 30 r.p.m., a continuous

structure with a phase size of 30 μm was obtained. This phase size was considered

appropriate for biomedical applications and was thus adopted in this study. The effect of

r.m.p. on the phase size was found to be consistent with the findings in the previous

study[25] involving the same polymer components. The phase structure produced at 200°C

and 30 r.p.m. was found to be co-continuous. This was verified by weight measurement

before and after extraction of the PS phase; after extraction, the weight of the porous

material was half of the original blend. The formation of a co-continuous phase structure

under these mixing conditions can also be predicted using the phase inversion rule by

Paul and Barlow and later generalized by Miles and Zurek:

$$\frac{\phi_1}{\phi_2} = \frac{\eta_1(\dot{\gamma})}{\eta_2(\dot{\gamma})}, \qquad (4.1)$$

where $\eta_i(\dot{\gamma})$ is the viscosity of component i at blending conditions and ϕ_i is its

volume fraction at which phase inversion occurs. The shear rate at 200C and 30 r.p.m.

with a rotor diameter of 35.5 mm was estimated to be 47.5 s^{-1}. The viscosity ratio of PLA

over PS in this case is 0.6, calculated from the data in Fig. 4.2. For a 50/50 wt% PLA/PS blend used in this study, this viscosity ratio would result in a co-continuous phase morphology.

Due to the presence of interfacial tension, the co-continuous phase structure of an immiscible binary blend coarsens upon quiescent annealing at a temperature above the melting temperatures of both polymer components. Experimental studies[26,27] indicated that the phase size growth rate is constant at a constant annealing temperature, irrespective of the phase size. Generally speaking, the phase size growth rate is related to the volume fraction, the initial phase structure, the interfacial tension, and the zero-shear viscosity of the blend. From dimensional analysis, it can be shown that this growth rate, k, should be linearly dependent on the ratio of interfacial tension to blend viscosity,

$$k \sim \frac{\gamma}{\eta_e},$$
(4.2)

where γ is interfacial tension and η_e is equivalent blend viscosity. A similar relation has been derived by Yuan and Favis[27]. Since the polymer blend viscosity is sensitive to temperature changes, the phase size growth rate is expected to be strongly dependent on the annealing temperature. On the other hand, the temperature dependency of interfacial tension is usually much weaker. Therefore, one can effectively varying the phase coarsening rate by controlling the quiescent annealing temperature. In this study, the characteristic size of the ribs in the co-continuous structure measured by SEM was used to calculate the coarsening rate. At 200°C, the thickness of ribs grew from about 30 μm

to 300 μm in 10 min, yielding a coarsening rate approximately 30 μm/min. The coarsen rate at 180°C was approximately 10 μm/min. Due to the limitation and difficulty in accurate measurement of the average rib size, the above values are estimated values. However, the large reduction in coarsening rate at the lower annealing temperature agrees with the theory by Eq. 4.2.

In geometrically confined annealing, the two polymer components and the mold surface can form a ternary contact. Therefore, the contact properties between the mold surface and each individual polymer component are expected to play an important role in the annealing kinetics. The interfacial tension between the stainless steel mold surface and each polymer melt was determined by contact angle measurement on a goniometer. An equal volume of PLA and PS pellets were melted on the stainless steel plate surface under nitrogen protection. Because the viscosity of a polymer melt is several orders of magnitude higher than that of normal liquids with small molecules, like water, an extremely long experimental time of 2 hr was employed in order to observe the equilibrium behavior of the system. The reach to the equilibrium state was judged by observing the height of the melt droplet on the computer screen of the goniometer every 10 min. After 90 min, no obvious changes in droplet height and contact angle were detected. The contact angles of PLA and PS on the stainless steel surface at 200°C and a testing time of 2 hr are given in Fig. 4.3. Both polymers showed contact angles smaller than 90°, indicating their wettability on the steel surface. However, the contact angle of PLA was much smaller than that of the PS. If a true equilibrium state was achieved in the testing experiment, the smaller contact angle indicated higher wettability of PLA on the

steel surface.

(a)   (b)
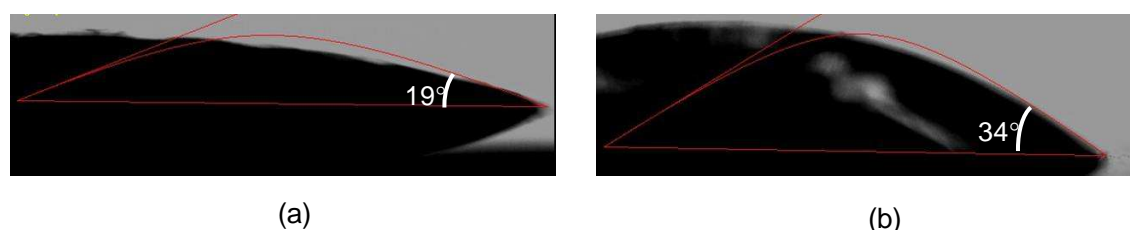
Figure 4.3: Contact angles on the stainless steel plate at 200°C for (a) PLA melt and (b) PS melt.

The phase structures from geometrically confined annealing under different experimental conditions were examined by SEM. To enhance the contrast of SEM imaging, the PS phase was solvent extracted, leaving a porous PLA structure. Before solvent extraction, the samples were smoothly cut with a sharp blade. This left a flat surface in the final porous structure, making it easier for phase size comparison.

Fig. 4.4 compares the phase structures of a 2.5 mm thick sample before and after contact annealing at 180°C for 10 min. The contact annealing experiment was conducted between a PDMS lubricated steel plate (upper) and a bare stainless steel plate (lower). For the as-mixed blend, a nearly uniform phase structure of a domain size about 30 µm is clearly seen in Fig.4. 4. a. After contact annealing, a graded phase structure was generated inside the sample (Fig. 4. 4. b). No visible growth was found on the side in contact with the
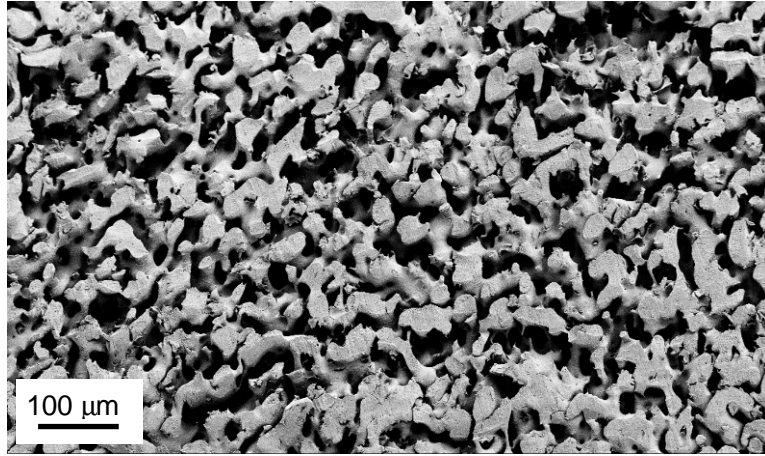
(a)
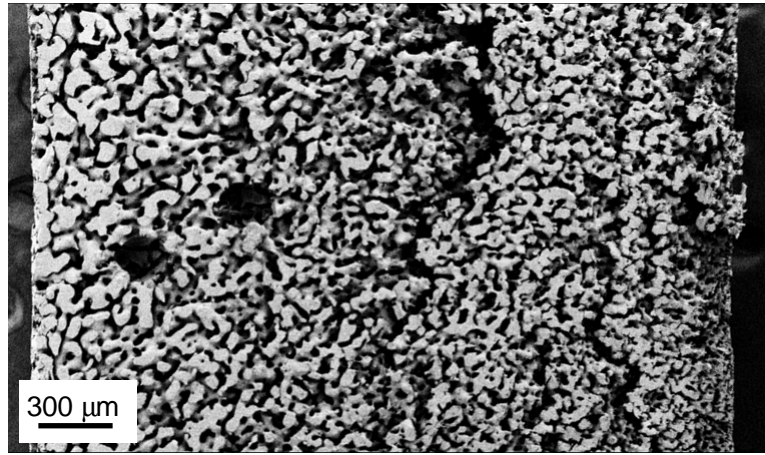
(b)

Figure 4.4: Phase structure before and after contact annealing: (a) as-mixed blend; and (b) after contact annealing at 180°C for 10 min with a gap size of 2.5 mm. In contact annealing, a thin layer of silicone oil was applied on the upper platen, corresponding to the left side of (b).

bare steel surface; however, the phase structure on the other side with PDMS lubrication was able to grow to approximately 100 µm. This larger size is comparable to the characteristic phase size obtained from quiescent annealing for the same annealing temperature and time. The gradient in phase size may be explained using the different boundary conditions employed in this contact annealing experiment. With a lubricated

upper surface, a slip condition is likely to occur. In this case, the phase structure can freely grow during annealing, and therefore a similar coarsening rate as in quiescent annealing was obtained. In contrast, when the bare stainless steel was used, the mobility of the polymer components at the mold surface would be lower than in quiescent annealing due to the so-called no-slip wall condition. In the extreme case when a fully no-slip wall should exist, the phase structure would be anchored at the mold surface, resulting in a zero growth rate.
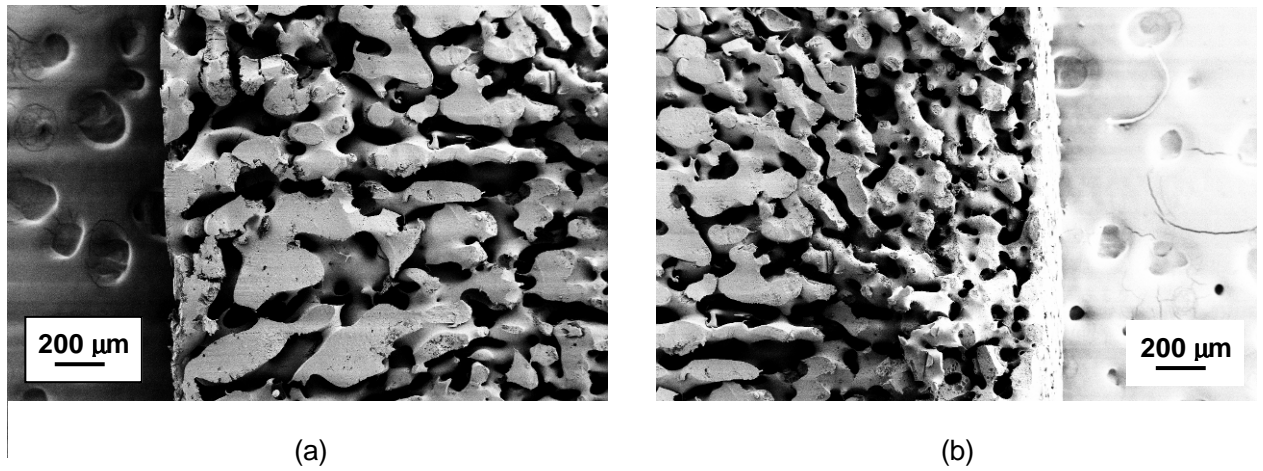
Figure 4.5: Phase structure developed after contact annealing at 200°C for 10 min with a gap size of 2.5 mm: (a) near the oil coated stainless steel surface; and (b) near the bare stainless steel surface.

This hypothetical mechanism for formation of a graded phase structure between lubricated and bare steel surfaces was further tested at another annealing temperature of 200°C. Fig. 4.5 compares the phase structures developed on the different contact sides after an annealing time of 10 min. A gradient in pore size was also observed for this annealing condition. The average pore size found to be much larger than at 180°C. This time, pores near the lubricated surface grew to about 300 μm which was several times larger than these near the confining surface. The larger size on the lubricated side is again comparable to that in quiescent annealing. However, there appeared to be some growth on the bare steel side. This may indicate the existence of a partial wall slip condition at the contact.

The results in Fig. 4.4 and Fig. 4.5 demonstrated the strong effects from boundary conditions on the phase coarsening behavior during geometrically confined annealing. Combining with the temperature effect, one may control both the phase size

and its gradient in confined annealing, leading to the production of gradient porous materials with a controllable structure. The effect of gap size in contact annealing was also investigated. Fig. 4.6 shows different phases structures created with reduced gap sizes of 1.5 mm and 1 mm. The annealing temperature and time were set to 180°C and 10 min. In the SEM pictures, the phase structures are oriented in their annealing position; that is, the upper side corresponds to the lubricated contact side, and the lower side corresponds to the bare steel side. For both reduced thicknesses, the phase size on the lubricated side was comparable to that in quiescent annealing while on the bare steel side, no significant growth was detected. Since the thickness is reduced, the resulting pore size gradients are larger for these reduced gap thicknesses.
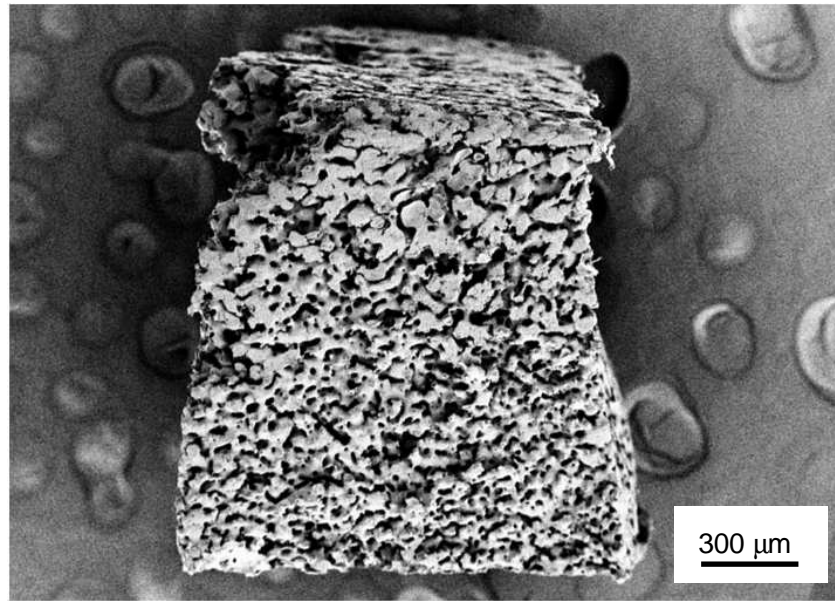
(a)
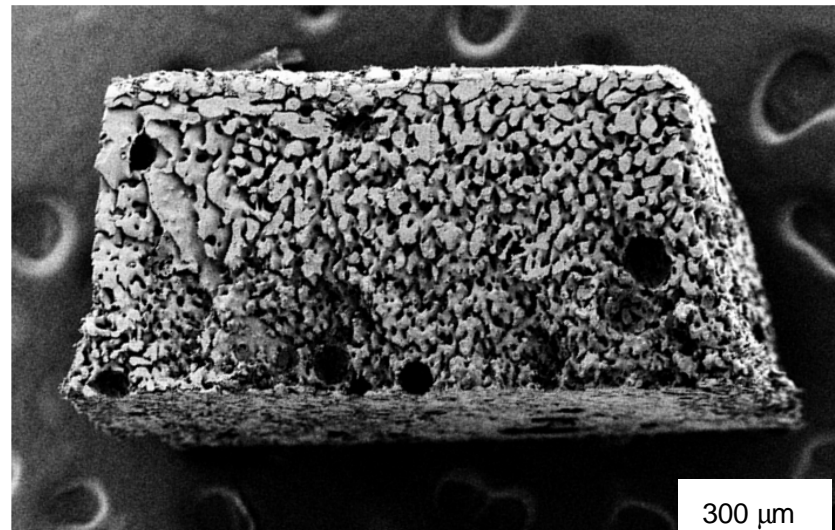
(b)

Figure 4.6: Phase structures developed after contact annealing at 180°C for 10 min with reduced gap sizes: (a) 1.5 mm; and (b) 1 mm.
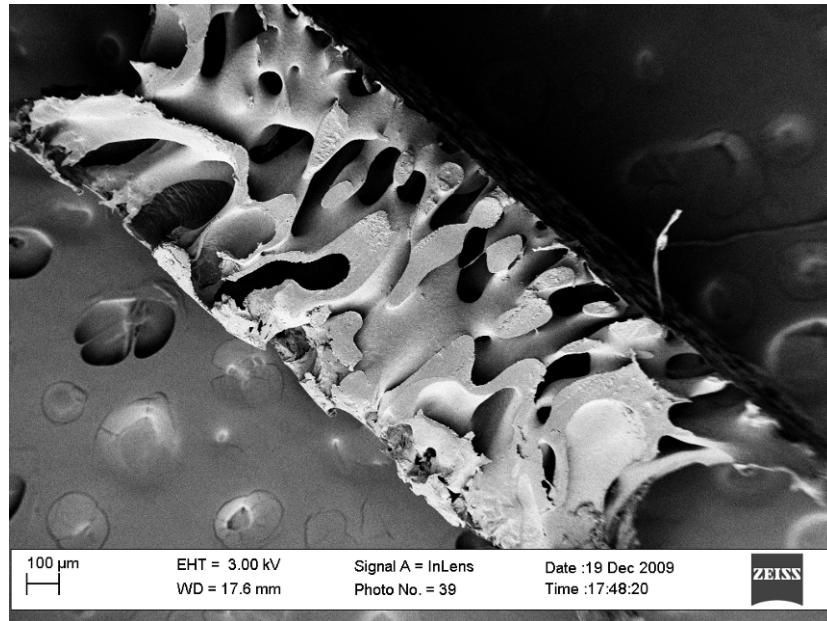
Figure 4.7: Orientated phase structure developed after geometrically confined annealing with oil-coated stainless steel surface on both sides. The annealing temperature, annealing time and gap size are 180°C, 10 min and 0.7 mm, respectively.

Experiments were also conducted at extremely small gap sizes comparable to the grain size of coarsened phase structures. When the gap size was reduced to 0.5 mm, demolding became a difficulty because of strong adhesion between the annealed blend and the bare steel surface. To resolve this issue, both plates were sprayed with PDMS to release the adhesion. In this case, a near wall-slip condition is expected on both sides, and therefore the phase structure would freely grow on both sides. However, as the gap size approaches the phase size, some discrete effects may arrive. Fig. 4.7 showed an orientated phase structure developed after annealing at 180°C for 10 min between two PDMS lubricated steel surfaces with a gap size of 0.7 mm. The pores appeared to be aligned more in the thickness direction. Similar orientation was also observed at 200°C

with small gap sizes less than 1 mm, especially at a long annealing time. However, at shorter annealing times, e.g., less than 5 min, no obvious orientation was observed. These results indicated that an orientated morphology would represent a thermodynamically more favorable state under such extreme confinement. Similar orientated phase structures under extreme confinement was also observed by other researchers in copolymer structures.[31-33]
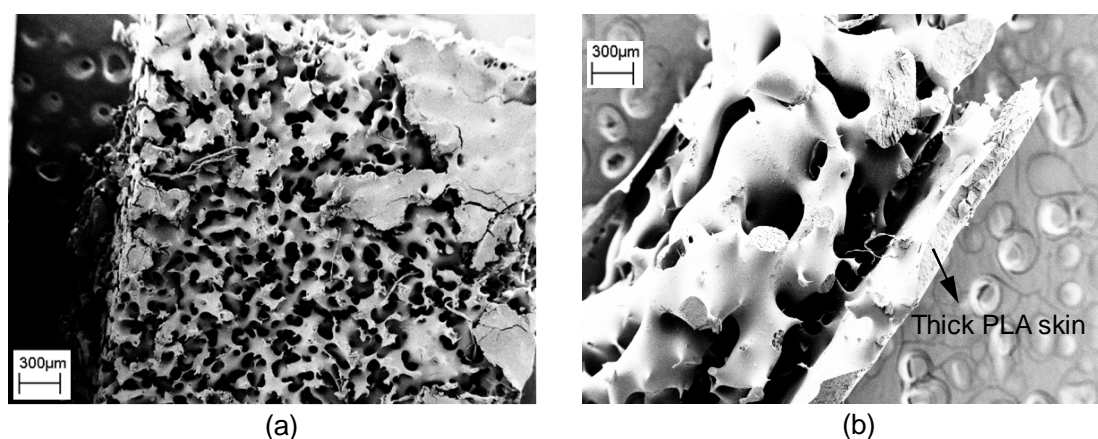
Figure 4.8: Formation and growth of skin layer during compression annealing: (a) instantaneous formation of a thin PLA skin; and b) growth of the skin after 20 min at 200°C. Bare stainless steel were used for both contact surfaces.

The results from compression annealing at 200°C with a compression ratio of 6 are given in Fig. 4.8 and Fig. 4.9. Two types of mold surfaces were used: stainless steel surface and PTFE surface. For both cases, a thin skin of PLA, approximately 10 μm thick, was formed immediately after the compression, as shown in Fig. 4.8.a and Fig. 4.9.a (in Fig. 4.8.a, the thin skin was partially removed to show the inside structure). As the 12 mm sample being slowly compressed, a lateral squeeze flow was formed parallel

to the compressing surface. It has been reported that the low viscosity component in a polymer blend during shear flow tends to migrate to the mold-blend interface to minimize the total system free energy[34-39]. In this PLA/PS blend, PLA was the low viscosity component during compression and, according to the energy minimization theory, it has the tendency to flow to the high shear rate region near the mold-blend interface. This possible mechanism for phase migration may be considered in a simple extreme case involving a liquid soaked sponge. When the sponge is compressed, the liquid will be squeezed and migrated out of the sponge structure. In fact, PLA skin was also formed on the lateral non-contact side of the sample.
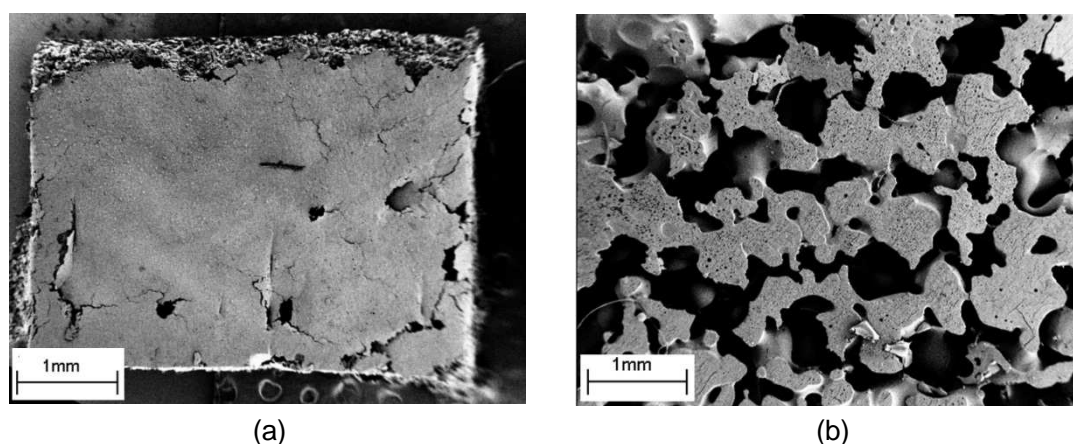
Figure 4.9:   Results from compression annealing between a pair of Teflon surfaces at 200°C: (a) a thin PLA skin formed instantaneously after compression molding; and (b) the thin skin disappeared after 20 min.

The thickness of the PLA skin layer was found to either grow or reduce during compression annealing depending on the type of mold surface. For the compressed sample annealed with the steel contact, the initial dense skin of PLA became thicker and

reached about 200 µm at the end of 10 min annealing, as shown in Fig. 4.8.b. This result may be understandable, considering the better wettability of PLA on the steel surface as indicated by the contact angles in Fig. 4.3. Furthermore, the thin PLA layer adhered at the mold surface could serve as a seed layer to drive in-flow of more PLA from the bulk through the co-continuous network due to the minimization of interfacial energy. On the other hand, the compressed sample with the PTFE contact lost its initial PLA skin after a period of annealing. Fig. 4.9.b shows the structure developed after a 20 min of annealing at 200°C. A fully co-continuous structure can be clearly seen at the blend surface.

Based on these experimental results on compression annealing, it was speculated that the difference in interfacial affinity between the polymer components and the mold surface could significantly affect the annealing path. With the steel surface, the higher wettability of PLA on the mold surface would promote the formation of the 200 µm thick PLA skin at the end of annealing. However, when PTFE was used as the mold surface material, the PLA would dewet on the mold surface. Therefore, the PLA in the initial skin layer started to reorganize in order to reach a lower energy state.
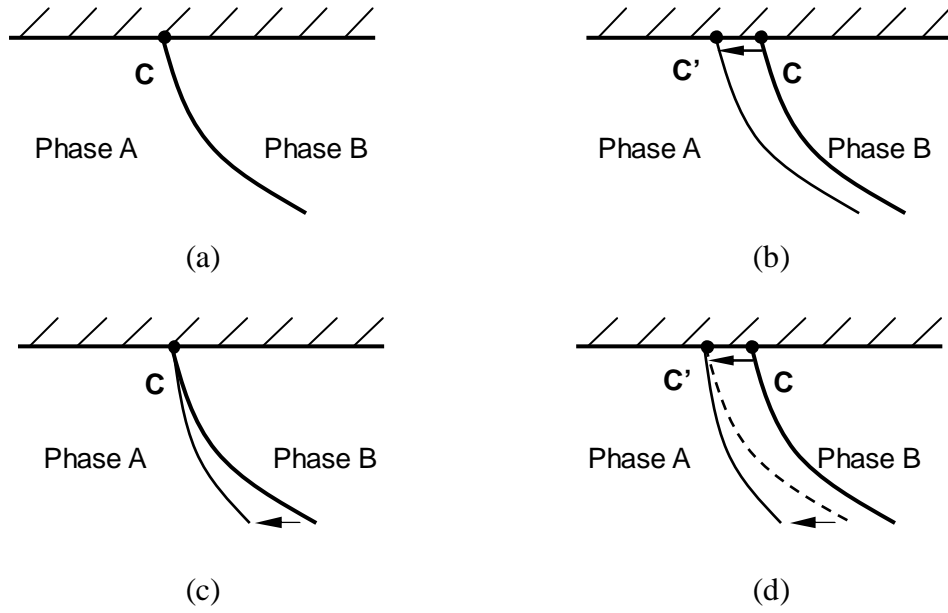
Figure 4.10: Boundary conditions at the ternary contact line (TCL) and the binary polymer interface (BPI): (a) no-slip TCL with stationary BPI; (b) slip TCL with stationary BPI; (c) no-slip TCL with BPI relaxation; and (d) slip TCL with BPI relaxation.

One major finding from this study is that the kinematic boundary condition at the mold surface can significantly affect the coarsening process during geometrically confined annealing. To understand this effect, two types of boundary conditions at the ternary contact line (TCL) and their interplay with the relaxation of the binary polymer interface (BPI) are illustrated in Fig. 4.10. Fig. 4.10.a shows a blend with a fully compatible BPI in contact with the mold surface with a no-slip TCL. In this case, no change of the phase structure is expected. In Fig. 4.10.b, a slip wall is applied at the TCL so that the TCL can move along the mold surface. In Fig. 4.10.c, BPI relaxation is allowed for a no-slip TCL. In this case, the BPI is anchored at the mold surface, but it can be deformed away from the mold surface. Therefore, phase structure coarsening can occur away from the mold surface. This case can be used to describe the results from

contact annealing with the bare stainless steel surface. In the last case in Fig. 4.10.d, combined effects of a slip TCL and a mobile BPI are illustrated. In this case, the BPI can

Slip wall

Slip wall

(a)

No-slip wall

No-slip wall

(b)
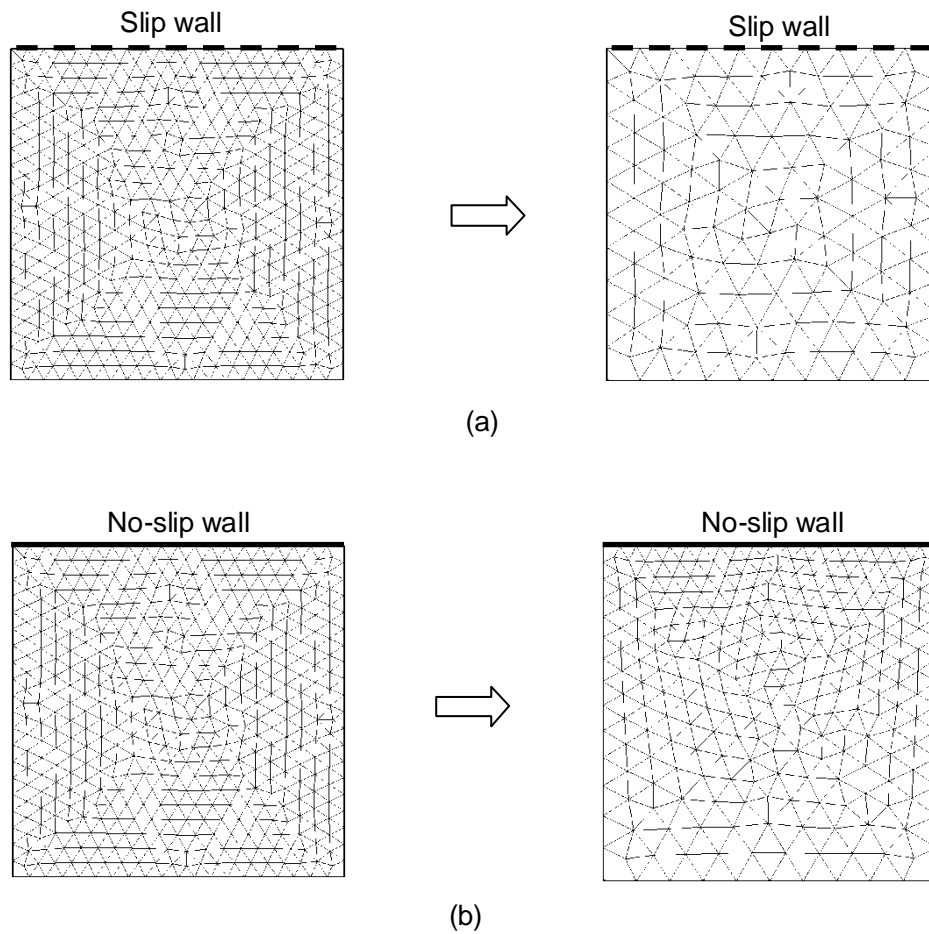
Figure 4.11: Effects of kinetic boundary condition on phase structure coarsening (a) with slip wall; and (b) with no-slip wall.

freely move and deform at the mold surface. The contact annealing at the PDMS lubricated steel surface conforms to this combined boundary and interfacial conditions. The phase coarsening process of an immiscible polymer blend during contact annealing with different TCL contact conditions is also schematically depicted in Fig. 4.11. With a slip wall, uniform coarsening of the phase structure is expected, while with a no-slip wall, graded coarsening would occur.
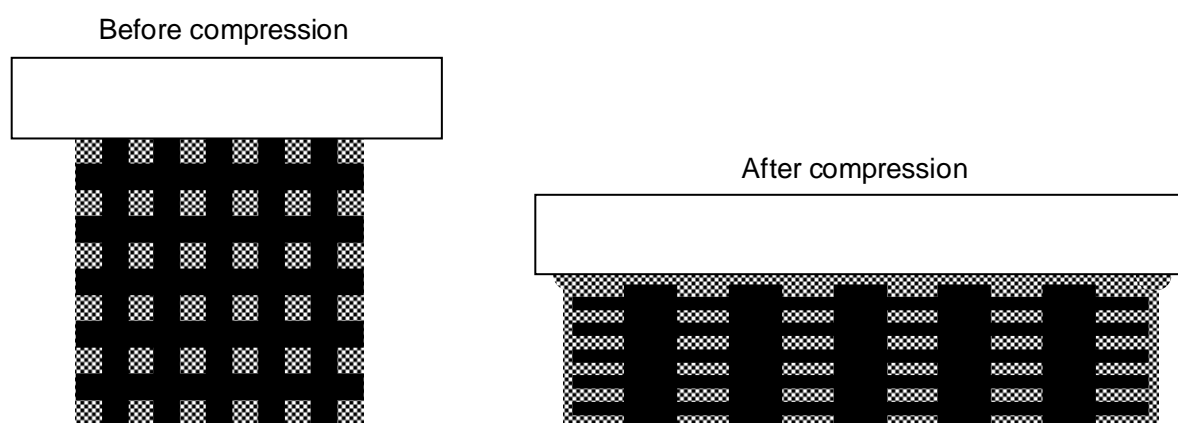
Figure 4.12: Formation of skin layer at the mold surface after compression molding.

Another important finding is on the instantaneous formation of a thin polymer film at the contact surface during compression molding. This effect is illustrated in Fig. 4.12; after compression molding, a thin polymer layer migrated to the mold surface. In this case, a dense skin, rather than a porous surface, would be formed after extraction of the second polymer component. Although a sound theory for this phenomenon is yet to be determined, it may be simply described using the sponge effect. Upon compression, the low viscosity polymer liquid can be squeezed out from the more solid-like sponge

network formed by the second polymer.

While efforts are being conducted to further investigate these interface or contact surface related effects during confined annealing, some useful processing strategies can be proposed for formation of innovative porous materials. By varying the mold surface properties, the compression ratio, the size of the geometry, the annealing temperature and time, one can obtain a large degree of freedom in kinetics for creating porous materials with controllable pore sizes, pore size gradient, and even gradient in density.

4.4   Conclusions

This study explored possible geometrical confinement effects during compression molding of co-continuous polymer blends for scaffold applications. Two annealing procedures, contact annealing and compression annealing, were used for coarsening the phase structure. Gradient porous structures were generated in contact annealing experiments with different annealing temperatures and gap sizes. The degree of phase coarsening near the mold surface was found to be significantly affected by the mold surface properties. The coarsening process at a no-slip mold surface was suppressed, resulting in a near-zero phase coarsening rate. This geometrical confining effect was largely relaxed at a PDMS lubricated mold surface, yielding a phase size comparable to that in quiescent annealing. The gap size was found to affect the gapwise morphology. In particular, at an extremely small gap size comparable to the phase size after quiescent coarsening, an oriented phase structure was developed between two lubricated mold surfaces. Compression annealing at a compression ratio of 6 was conducted using both

steel and PTFE mold surfaces. For both types of mold surfaces, a thin PLA skin layer was formed immediately after compressing a 12 mm thick blend disc to 2 mm. This skin thickened to 200 µm after 10 min annealing at 200°C with metal contact, but disappeared on the PTFE mold surface with the same processing parameters. These experimental results indicated a large process window for controlling the process kinetics in geometrically confined annealing during compression molding. By varying the mold surface properties, the compression ratio, the size of the geometry, the annealing temperature and time, one can obtain a large degree of freedom in kinetics for creating innovative porous materials with controllable pore sizes, pore size gradient, and even gradient in density.

4.5 References

1. Thomson, R. C., M. J. Powers, and A. G. Mikos. Hydroxyapatite fiber reinforced poly(a-hydroxy ester) foams for bone regeneration. *Biomaterials* 19:1935-1943, 1998.

2. Goldstein, A. S., G. Zhu, G. E. Morris, R. K. Meszlenyi, and A. G. Mikos. Effect of osteoblastic culture conditions on the structure of poly(DL-lactic-co-glycolic acid) foam scaffolds. *Tissue Engineering* 5:421-433, 1999.

3. Mikos, A. G., A. I. Thorsen, L. A. Czerwonka, Y. Bao, R. Langer, D. N. Winslow, and I. P. Vacanti. Preparation and characterization of poly(L-lactic acid) foams. *Polymer* 35:1068–77, 1994.

4. Shastri, V. P., I. Martin, and R. Langer. Macroporous polymer foams by hydrocarbon templating. *Proc. Natl. Acad. Sci. U.S.A.* 97:1970–5, 2000.

5. Mooney, D. J., C. L. Mazzoni, C. Breuer, K. McNamara, D. Hern, and J. P. Vacanti. Stabilized poly glycolic acid fibre-based tubes for tissue engineering. *Biomaterials* 17:115-124, 1996.

6. Mikos, A. G., A. J. Thorsen, L. A. Czerwonka, Y. Bao, R. Langer, D. N. Winslow, and J. P. Vacanti. Preparation and characterization of poly(L-lactic acid) foams. *Polymer* 35:1068-1077, 1994.

7. Mikos, A. G., Y. Bao, L. G. Cima, D. E. Ingber, J. P. Vacanti, and R. Langer. Preparation of poly (glycolic acid) bonded fiber structures for cell attachment and transplantation. *J. Biomed. Mater. Res.* 27:183–189, 1993.

8. Schugens, C., V. Maquet, C. Grandfils, R. Jerome, and P. Teyssie. Polylactide macroporous biodegradable implants for cell transplantation II: preparation of polylactide foams for liquid–liquid phase separation. *J. Biomed. Mater. Res.* 30:449–461, 1996.

9. Nam, Y. S. and T. G. Park. Biodegradable polymeric microcellular foams by modified thermally induced phase separation method. *Biomaterials* 20:1783–1790, 1999.

10. Nam, Y. S. and T. G. Park. Porous biodegradable polymeric scaffolds prepared by thermally induced phase separation. *J. Biomed. Mater. Res.* 47:8–17, 1999.

11. Lo, H., S. Kadiyala, S. E. Guggino, K. W. Leong. Poly(L-lactic acid) foams with cell seeding and controlled-release capacity. *J. Biomed. Mater. Res.* 30:475–84, 1996.

12. Lo, H., M. S. Ponticiello, and K. W. Leong. Fabrication of controlled release biodegradable foams by phase separation. *Tissue Eng.* 1:15–28, 1995.

13. Mooney, D. J., D. F. Baldwin, N. P. Suh, J. P. Vacanti, and R. Langer. Novel approach to fabricate porous sponges of poly(D,L-lactic-co-glycolic acid) without the use of organic solvents. *Biomaterials* 17:1417–22, 1996.

14. Park, T. G. New approaches to fabricate highly porous tissue scaffolds. *The Fourth Asia-Pacific conference on medical and biological engineering, Seoul, Korea,* 1999.

15. Nam, Y. S., J. J. Yoon, and T. G. Park. A novel fabrication method of macroporous biodegradable polymer scaffolds using gas foaming and salt as a porogen additive. *J. Biomed. Mater. Res., Appl. Biomater.* 53:1–7, 2000.

16. Sparacio, D. and E. J. Beckman. Generation of microcellular biodegradable polymers in supercritical carbon dioxide. *Polymer Preprints: Division of Polymer Chemistry, American Chemical Society* 38(2):420–423, 1997.

17. Harris, L. D., B. S. Kim, and D. J. Mooney. Open pore biodegradable matrices formed with gas foaming. *J. Biomed. Mater. Res.* 42:396–402, 1998.

18. Wang, X. X., W. Li, and V. Kumar. A method for solvent-free fabrication of porous polymer using solid-state foaming and ultrasound for tissue engineering applications. *Biomaterials* 27:1924–1929, 2006.

19. Singh, L., V. Kumar, and B. D. Ratner. Generation of porous microcellular 85/15 poly(D,L-lactide-co glycolide) foams for biomedical applications. *Biomaterials* 25(13):2611–7, 2004.

20. Park, A., B. Wu, and L.G. Griffith. Integration of surface modification and 3D fabrication techniques to prepare patterned poly(L-lactide) substrates allowing regionally selective cell adhesion. *J. Biomater. Sci. Polym. Ed.* 9:89–110, 1998.

21. Landers, R. and R. Mülhaupt. Desktop manufacturing of complex objects, prototypes and biomedical scaffolds by means of computer-assisted design combined with computer-guided 3D plotting of polymers and reactive oligomers. *Macromol. Mater. Eng.* 282:17–21, 2000.

22. Ang, T.H., F. S. A. Sultana, D. W. Hutmacher, Y. S. Wong, Y. H. Fuh, H. T. Mob, et al. Fabrication of 3D chitosan-hydroxyapatite scaffolds using a robotic dispensing system. *Mater. Sci. Eng. C* 20(1–2):35–42, 2002.

23. Hoque, M. E., E. W. Hutmacher, W. Feng, S. Li, M. H. Huang, M. Vert, and Y. S. Wong. Fabrication using a rapid prototyping system and in vitro characterization of PEG-PCL-PLA scaffolds for tissue engineering. *J. Biomater. Sci. Polymer Edn* 16(12):1595-1610, 2005.

24. Taboas, J. M., R. D. Maddox, P. H. Krebsbach, and S. J. Hollister. Indirect solid free form fabrication of local and global porous, biomimetic and composite 3D polymer-ceramic scaffolds. *Biomaterials* 24:181-194, 2003.

25. Yao, D., W. Zhang, and J. G. Zhou. Controllable Growth of Gradient Porous Structures. *Biomacromolecules* 10(5):1282-1286, 2009.

26. Yuan, Z. H. and B. D. Favis. Macroporous poly(L-lactide) of controlled pore size derived from the annealing of co-continuous polystyrene/poly(L-lactide) blends. *Biomaterials* 25:2161-2170, 2004.

27. Yuan, Z. H. and B. D. Favis. Coarsening of immiscible co-continuous blends during quiescent annealing. *AIChE Journal* 51:271-280, 2005.

28. Potschke, P. and D. R. Paul. Formation of Co-continuous structures in melt-mixed immiscible polymer blends. *J. Macromole. Sci.-Polymer Reviews* C43(1):87-141, 2003.

29. Riscanu, D., B. D. Favis, C. Y. Feng, and T. Matsuura. Thin-film membranes derived from co-continuous polymer blends: preparation and performance. *Polymer* 45:5597-5609, 2004.

30. Cox, W. P. and E. H. Merz. Correlation of Dynamic and Steady Flow Viscosities. *J. Polym. Sci. 28*(118):619–622, 1958.

31. Koneripalli, N., R. Levicky, and F. S. Bates. Confinement-induced morphological changes in diblock copolymer films. *Langmuir* 12:6681-6690, 1996.

32. Kellogg, G. J., D. G. Walton, A. M. Mayes, P. Lambooy, T. P. Russell, P. D. Gallagher, and S. K. Satija. Observed surface energy effects in confined diblock copolymers. *Physical Review Lett*ers 76(14):2503-2506, 1996.

33. Pickett, G. T. and A. C. Balazs. Equilibrium orientation of confined diblock copolymer films. *Macromolecules* 30:3097-3103, 1997.

34. Zhang, W., D. Sarang, and Y. Donggang. Processing properties of polypropylene with a minor addition of silicone oil. *Polym. Eng. Sci.* accepted, 2009.

35. Lee, H. and L. A. Archer. Functionalizing polymer surfaces by field-induced migration of copolymer additives – Role of shear fields. *Polym. Eng. Sci.* 42:1568-1579, 2002.

36. Shelby, M. D. and G. B. Caflisch. Shear field induced diffusion and molecular weight fractionation during polymer processing. *Polym. Eng. Sci.* 44:1283-1294, 2004.

37. Zatloukal, M., J. De Witte, C. Lavalle, and P. Saha. Investigation of PPA interactions with polymer melts in single layer extrusion and coextrusion flows. *Plastics Rubber and Composites* 36:248-253, 2007.

38. Kharchenko, S. B., P. M. McGuiggan, and K. B. Migler. Flow induced coating of fluoropolymer additives: Develoment of frustrated total internal reflection imaging. *Journal of Rheology* 47:1523-1545, 2003.

39. Lo, H.H.K., C.M. Chan, and S.H. Zhu. Characterization of the lubricant layer formed at the interface between the extrudate and the die wall during the extrusion of high density polyethylene and fluoroelastomer blends by XPS, SIMS and SEM. *Polym. Eng. Sci.* 39:721-732, 1999.

CHAPTER 5

FABRICATION OF INTERCONNECTED MICROPOROUS BIOMATERIALS WITH HIGH HYDROXYAPATITE NANOPARTICLE LOADING

5.1 Introduction

Biodegradable and biocompatible polymers, due to some advantageous properties over traditional metallic materials, find increasing applications in biomedical implanting devices [9, 10, 2]. Extensive research has also been conducted to further improve the mechanical properties as well as bioactivity of these "new" implanting materials. In particular, combining hydroxyapatite with a biopolymer such as poly (glycolic-co-lactic acid) (PLGA) was demonstrated to be able to generate synergistic result by taking advantage from each component [9, 10].

Recently, the importance of interconnected microporous structures was also emphasized by researchers in this field, and many intelligent techniques were invented to make such structures. Existing techniques able to realize this design concept include fiber bonding (nonwoven meshes)[19, 17, 6], solvent casting/particulate leaching [33, 7, 17, 29], phase separation/emulsification [35, 28, 21, 15], gas foaming [20, 24, 22, 31, 8, 34, 30], co-continuous melt blending [25, 37, 38, 36], and solid freeform fabrication techniques [24, 13, 1, 12, 32]. These techniques have been found to be especially useful when dealing with polymers.

However, most of these existing methods for porous materials are not suitable for filled/reinforced polymers, and the lack in mechanical strength of the resulting porous materials hinders their applications in load bearing, either primary or secondary, biomedical devices. Particularly for methods dealing with a polymer solution, such as solvent casting and phase separation, one primary difficulty is caused by the segregation of the particles over the required long processing period. For other methods coping with a polymer melt, such as gas forming and melt blending, the extremely high viscosity of the filled polymer, especially at high particle loading, causes a processing difficulty. On the other hand, solid freeform fabrication techniques such as fusion deposition modeling and laser sintering can be used to include inorganic fillers, but they have a low resolution, prohibiting the production of finely structured materials.

In the present work, we developed and investigated a technique for processing porous biopolymer composites with high nanoparticle loading. Melt blending combined with after-mixing small-strain oscillation were found to be effective in obtaining the needed interpenetrating microporous material. As a case study, this technique was used to generate a highly HA loaded PLGA nanocomposite with an interconnected microporous structure. The mechanisms underneath the experimental observations, particularly on the enhanced particle migration under oscillatory shear, were discussed, and strategies for producing highly particle loaded biopolymers with interconnected microporous structures were proposed.

5.2   Fabrication Method

Polymer melt blending was identified as a potential technique for generating the needed microporous material with high nanoparticle loading. Due to its high level of process controllability, melt blending has recently been reported as a versatile protocol for processing porous materials [25, 37, 38, 36]. In this method, a binary polymer blend with a co-continuous phase structure was prepared first, and after extraction of the sacrificial polymer component a porous material is produced. To incorporate high loading of nanoparticles in the porous material, new challenges arrive. First, if the sacrificial polymer contains a large amount of particles, channel blockage can result after sacrificial polymer dissolution. Second, inclusion of a high concentration of nanoparticles in the blend can result in extremely high viscosity and therefore a difficult process. Alternatively, one may elect to premix the biopolymer with the particles and then blend the resulting mixture with the sacrificial polymer. However, this would result in a large difference in viscosity between the two polymer components, leading to the generation of an unwanted droplet phase structure.

The new technique aimed at reducing the nanoparticle usage during blending, resolving the channel blockage problem after sacrificial extraction, and yet producing an interpenetrating porous material with the desired high nanoparticle loading. The following steps are involved in this process. First, a biodegradable polymer, a sacrificial polymer, and inorganic fillers are melt-blended under appropriate conditions for forming a co-continuous phase structure. Then, at the melt state, the blend is subjected to a small-strain oscillation to facilitate migration of the filler particles from

the sacrificial component to the biopolymer component. In the final step, the sacrificial phase is selectively dissolved to leave an interconnected microporous structure consisted of only the biodegradable polymer and the inorganic fillers. The salient feature of this technique is the inclusion of an accelerated particle migration process. This not only substantially reduces the nanoparticle usage (and thus reduced viscosity during melt blending), but also avoids unwanted accumulation of particles in the open channels.

5.3 Experimental

5.3.1 Materials

PLGA in a biomedical grade for implanting devices was acquired from Purac (a division of CSM, Netherlands). The as-received PLGA was an amorphous polymer with glass transition temperature at 60°C, judged by DSC (Differential Scanning Calorimetry) at 10°C/min ramping rate. PS (polystyrene) from Dow Chemical (Dow Styron® 675 Polystyrene) with a Vicat softening point at 108°C was chosen as the sacrificial polymer. Both polymers were obtained in a pellet form from the suppliers. HA nanoparticles in a National Formulary (NF)/ Food Chemical Codex (FCC) grade with CAS code 1306-06-5 were obtained from Fisher Scientific (Calcium Phosphate C133-500). According to SEM, the size of the HA particles was around 100 nm or smaller, Fig. 5.1.
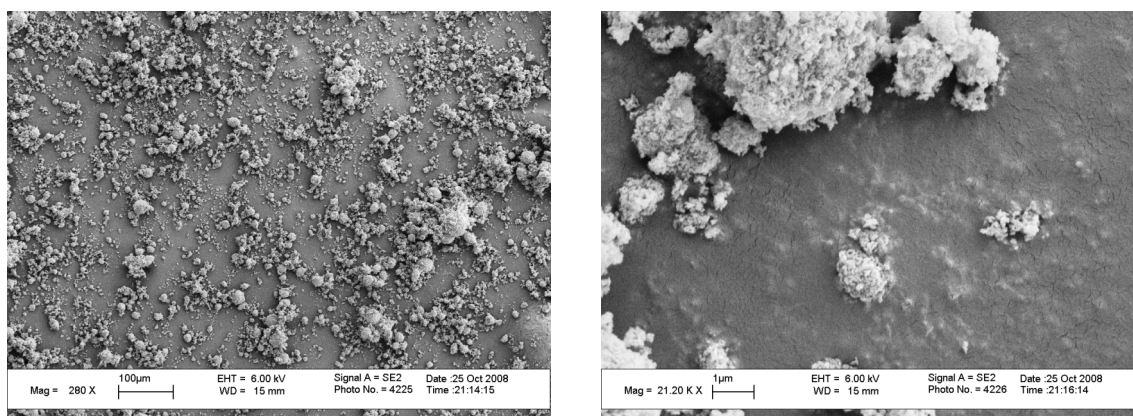
(a)	(b)

Figure 5.1: SEM images of Hydroxyapatite nanoparticle: (a) low resolution image; (b) zoom-in image.

5.3.2 Processing

A Brabender Intelli-Torque rheometer equipped with two roller blades capable of tumbling and distributive mixing was used to mix the raw materials. To reduce hydrolysis caused degradation, all the materials involved in this study were dried in a vacuum oven overnight at 90°C to remove the absorbed moisture and stored in a desiccator until ready for the next step of the experiment. A compounding temperature of 200°C and a mixing speed of 60 rpm were used during the blending process. The resulting shear rate is approximately 100 s^{-1}. Ultrahigh purity nitrogen was used as a purging gas during the whole mixing process to reduce degradation caused by oxygen and moisture. The achievement of a homogeneous blend morphology inside the chamber was established by the development of a constant blending torque.

In this study, two mixing procedures were compared. For the first procedure, a single-step mixing procedure, all three components were fed into the mixer

simultaneously. For the second procedure, a two-step mixing procedure, a uniform blend of PLGA and HA was premixed first, and then the PS component was added. After mixing, the molten blend was immediately scraped out of the chamber and quenched in tap water, followed by the same drying and storage procedure mentioned above.

The dried blends were compression molded into 1.2 mm thick sheets at 200°C and cut into discs of 25 mm diameter. The disk sample was then reheated to 200°C and subjected to oscillatory shear deformation under an isothermal condition at varied frequency and varied processing time. The oscillatory shear deformation was applied to the disc sample using a parallel-plate rheometer (AR2000ex from TA Instrument), with gap size set at 1 mm. After the oscillatory shear, the sample was cooled down to room temperature with a cooling rate of 10 °C/min.

To produce a porous material, the solidified ternary blend after compression molding and dynamic annealing was submerged in cyclohexane at 75°C for 3 days to extract the PS phase, the sacrificial phase. The complete extraction of PS was verified by comparing the weight of the dissolved sample with that of the original sample. Completely etched samples were dried in a vacuum oven at 90°C

5.3.3 Characterizations

Different characterization techniques, including XRT (X-ray tomography), SEM (scanning electron microscopy), and TGA (thermogravimetric analysis) were used to investigate the structure and morphology of the materials produced in this study. For

XRT, the disks after dynamic annealing and cooling but without solvent extraction were directly inspected on Dage X-Ray XD7600NT XRT. SEM (LEO SEM 1550 at 5 KV) was used to examine the structure of the porous materials after PS extraction. The SEM samples were sputtered with a gold/platinum alloy. The porous materials without sputtering were also examined with TGA (Q5000 IR from TA Instrument) to determine the concentration of HA nanoparticles. The TGA was operated under a pure nitrogen environment at 10°C/min heating rate. Additionally, the rheological properties of the tertiary blend were characterized on a parallel-plate rotational rheometer (AR2000ex from TA Instrument).

5.4   Results and Discussion

5.4.1 Morphology from SEM

SEM was used to observe the phase structure and nanoparticle distribution in the samples fabricated under different conditions. The phase structures of the as-mixed PLGA/PS 50/50 wt% and PLGA/PS/HA 40/40/20 wt% blends are compared in Fig. 5.2. In this comparison, both blends were prepared using the single-step mixing procedure. The phase size of the PLGA/PS blend was around 50 µm. With the ratio of PLGA to PS kept at 1:1, the addition of 20 wt% of HA nanoparticles in the blend yielded a reduced phase size of approximately 5 µm. This 10-times reduction in phase size may be partly attributed to the increased viscosity due to nanoparticle addition.

(a)   (b)
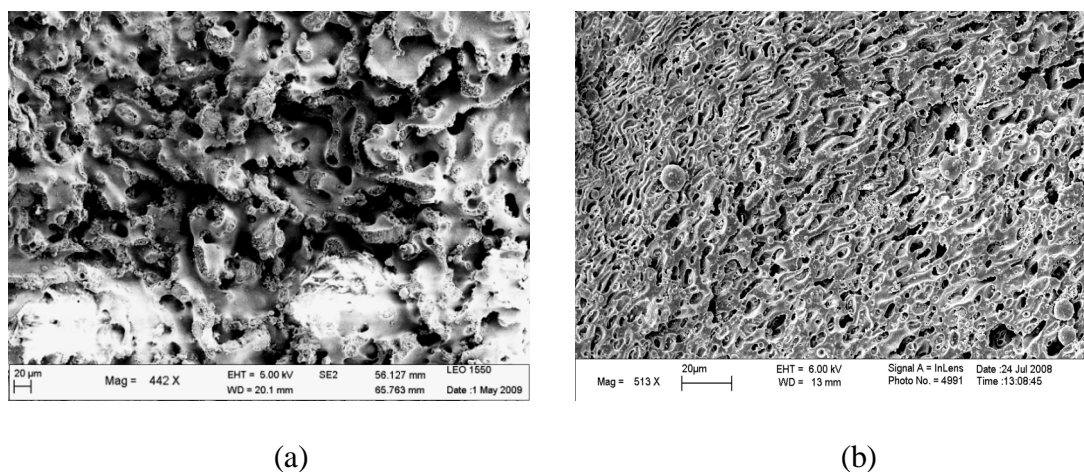
Figure 5.2: SEM morphology of the as-mixed blends after extraction of the PS phase: (a) PLGA/PS 50/50 wt% blend and (b) PLGA/PS/HA 40/40/20 wt% blend.
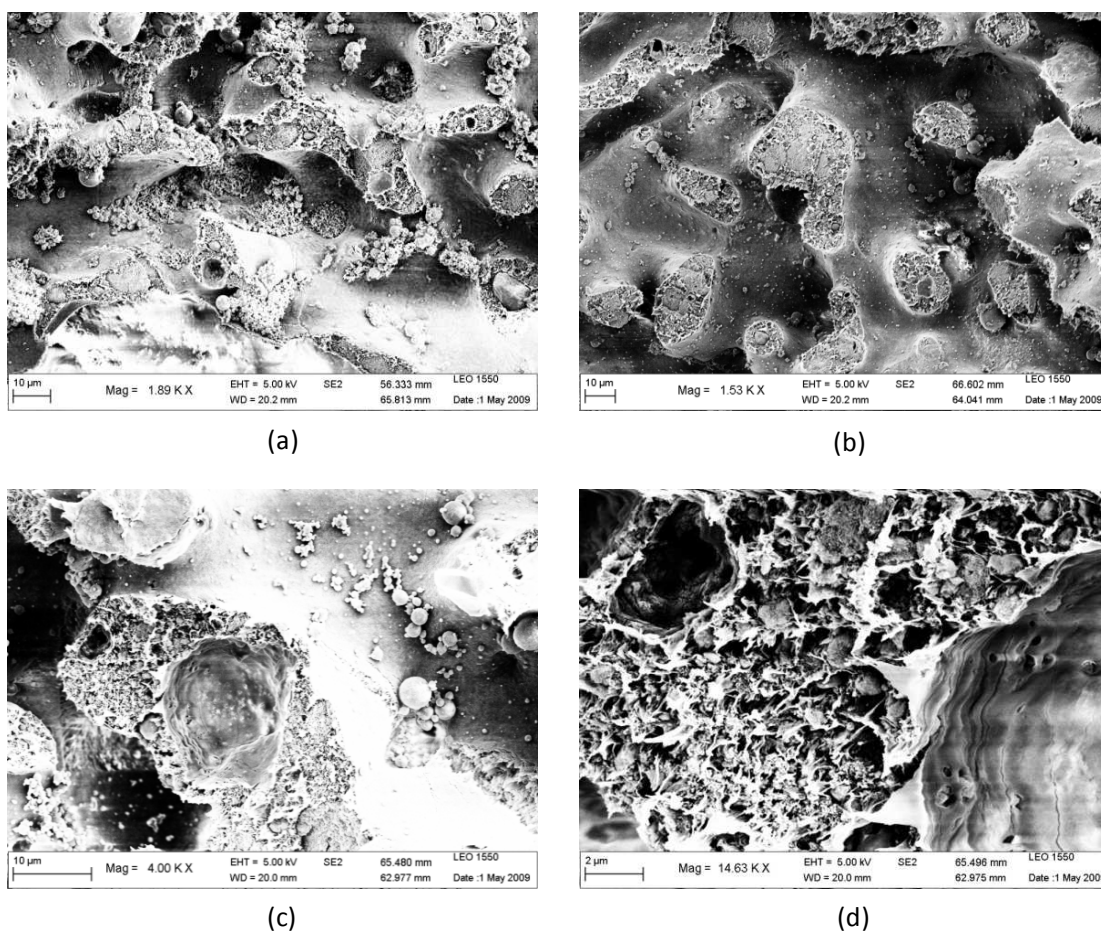
Figure 5.3: SEM morphology of the tertiary blend (PLGA/PS/HA 40/40/20 wt%) after extraction of the PS phase. The blend was prepared using the single-step mixing approach and after mixing was subjected to oscillatory shear deformation with two levels of oscillation time: (a) 5 min and (b-d) 20 min with different magnifications.

Fig. 5.3 shows the morphological evolution of the PLGA/PS/HA 40/40/20 wt% blend during dynamic annealing under small-strain oscillation. For all samples shown in the figure, the PS phase was extracted. It was seen that, with longer annealing time, more HA nanoparticles entered into the PLGA phase. For the as-mixed sample, HA nanoparticles were distributed uniformly in both PLGA and PS phases. After a short period of oscillation, e.g. 5 min, at 200°C and 1 rad/s, a considerable number of HA nanoparticles still remained in the PS phase; after dissolution of the PS phase, these

HA particles resided in the channels inside the PLGA (Fig. 5.3.a). In contrast, after a sufficiently long oscillation time, e.g. 20 min, the channel became rather clean, with only a limited number of relatively large HA particles presented (Fig. 5.3.b-c). This indicated that most small nanoparticles had migrated into the PLGA phase. The SEM image of this sample further indicated that these nanoparticles were uniformly distributed in the remaining PLGA phase (F. 5.3.d). The resulting material is a porous PLGA/HA composite, with interconnected 3-D microchannel network running inside the whole material. For comparison purposes, blends with only quiescent annealing, i.e., without small-strain oscillation, were also examined. Without oscillation, a large number of nanoparticles were presented inside the channels (with morphology similar to Fig. 5.3.a), even with a prolonged annealing time over 20 min. These results suggested that small-strain oscillation effectively assisted in the migration of the nanoparticles from the PS phase to the PLGA phase. Complete migration of the nanoparticles yielded a PLGA/HA composite at a high HA loading level reaching 33%. The composite material prepared by this method further possessed interconnected, clean microchannels. Note that if a large number of HA particles were presented in the PS phase, the channels after dissolution of the PS phase could be blocked by the residual particles. This could reduce the connectivity of the channels and hinder the use of the composite material in tissue engineering applications.

(a)	(b)
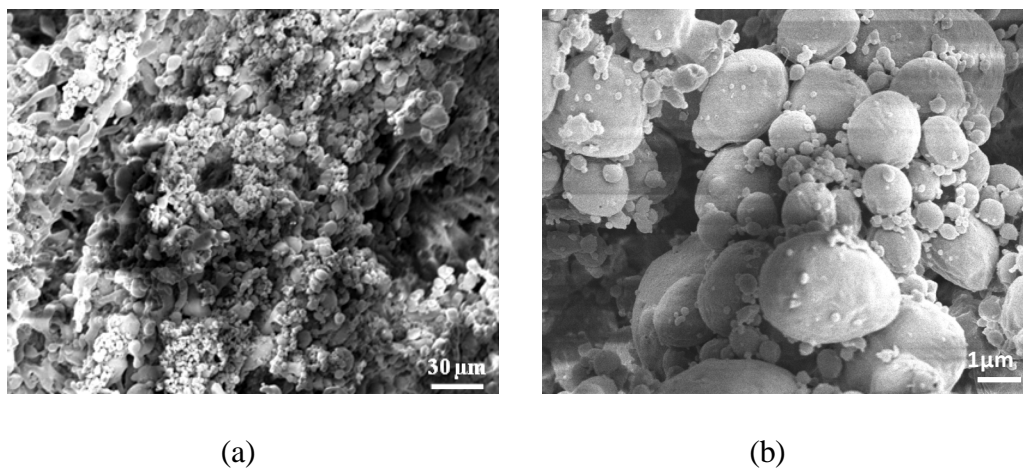
Figure 5.4: SEM morphology of the tertiary blend (PLGA/PS/HA 40/40/20 wt%) prepared using the two-step approach: (a) at low magnification and (b) a zoomed-in view.

The blends used for the SEM study shown in Fig. 5.3 were all prepared using the single-step mixing approach. In this case, all three components, i.e., PLGA, PS and HA, were fed into the batch mixer simultaneously during mixing. For comparison, the morphology of the blends made by premixing PLGA and HA and then mixing with PS was obtained, as shown in Fig. 5.4. The motivation was that this second approach, if successful, could be a more effective method for forming highly HA loaded PLGA materials/devices because in this case particle migration is no longer needed. However, the experimental results in Figure 3 indicated that the blend did not form a co-continuous morphology; instead, a droplet in matrix morphology was formed. This second method, therefore, did not yield a desirable porous PLGA composite material with interpenetrating microchannels.
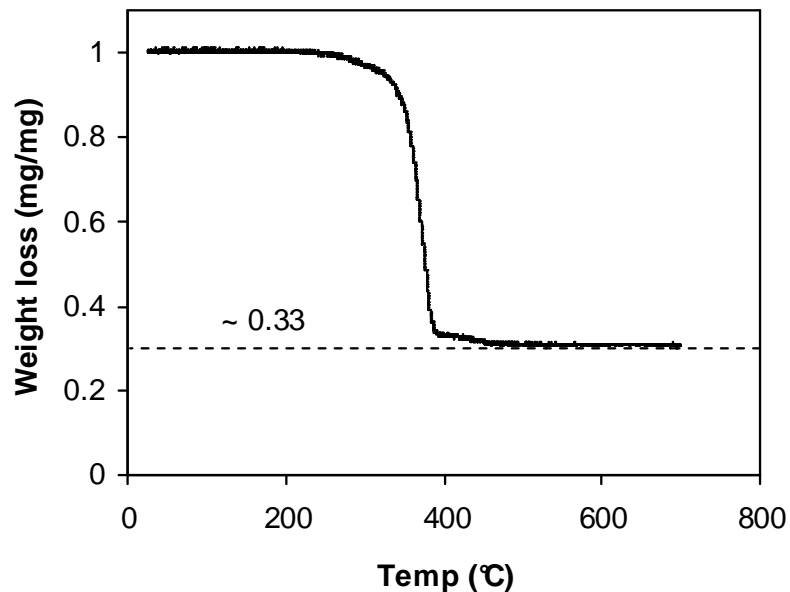
Figure 5.5: TGA of the PLGA/PS/HA blend sample oscillated with 1 rad/s angular frequency at 200°C for 2000 s. The PS phase was extracted by solvent before TGA.

5.4.2 Thermal Analysis

The concentration of HA nanoparticles in the porous PLGA/HA composite material was further evaluated by TGA. A heating rate of 10°C/min was used in the test. The TGA data of the sample processed at 200°C and under 1 rad/s oscillation for 20 min are shown in Fig. 5.5. From the testing data, one can find that the residual solid material at 700°C was approximately 33 wt%. It is known that at such high temperature, PLGA should be degraded into gasses. Therefore, the solid content should be HA particles, and the concentration of HA in the final porous PLGA composite should be 33%. Since microchannels inside the porous PLGA composite were quite clean, it can be further concluded that the 33% HA particles were mainly included in the PLGA matrix material.

(a)   (b)   (c)
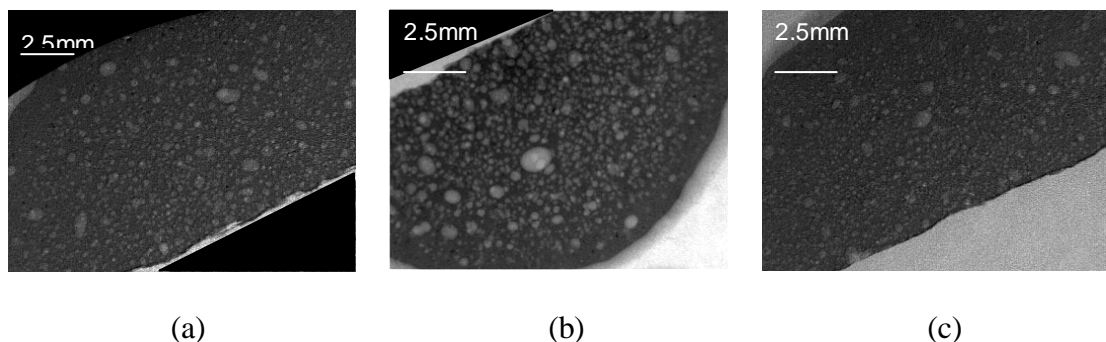
Figure 5.6: XRT of the PLGA/PS/HA blend (40/40/20 wt%) subjected to oscillatory shear at 1 rad/s and 200°C for different shearing times: (a) 5 min, (b) 10 min and (c) 20 min.

5.4.3 XRT observation

The contrast in XRT imaging comes from local density differences, or, more specifically, from local electron density differences. The density contrast between the two polymers involved in this study is much lower that that between the matrix and the HA phase; the density contrast between the two polymer components is around 1.1 while the value is more than 3 for HA/matrix. Therefore, XRT was expected to be able to pinpoint the HA distributions in the tertiary PLGA/PS/HA blend.

The samples used for XRT imaging in this study were all prepared using the single-step mixing procedure with a post-annealing stage under oscillatory deformation. Three different levels of annealing time were used during sample preparation: 5, 10, and 20 min. The results are shown in Fig. 5.6. A number of light-colored dots/regions can be seen in the XRT images for all samples. From the known density contrast between HA and the polymers, these light dots were believed to be HA deficient

polymer regions. This observation agreed with the SEM results previously described; when HA particles migrated from the PS phase to the PLGA phase, the PS phase had a reduced density, showing a light shade in XRT. Some kinetics on morphological development was also shown in the XRT results. For some reason, the light dots grew initially (from 5 min to 10 min) but reduced in size in a later stage (i.e., at 20 min). This result is a bit surprising and yet indicated the possible rearrangement of the nanoparticles in the polymer phases. At the initial stage of annealing, it is possible that a large number of highly concentrated nanoparticles were presented only at the interfacial region between the PS phase and the PLGA phase. The size of the PLGA phase would increase when the nanoparticles further diffused into and became evenly distributed in the PLGA phase. This rearrangement would cause the relative reduction of the PS phase.

It should also be noted that the size of the light dots appeared to be much larger than the size of the actual microchannels observed in SEM. This would be understood considering how XRT builds up the final image. Like all transmission mode techniques, XRT averages the information of a 3D object in the X-ray incident direction and projects on the normal plane of the incident beam. The projected features in this manner could have a size much larger than the actual size in a cross-sectional view. This could be particularly true for a 3-D co-continuous morphology. Some extremely large dots, with size over 0.5 mm and obviously larger than other surrounding dots, were also observed in the XRT images. These dots were believed to be air bubbles introduced to the blend during sample preparation.
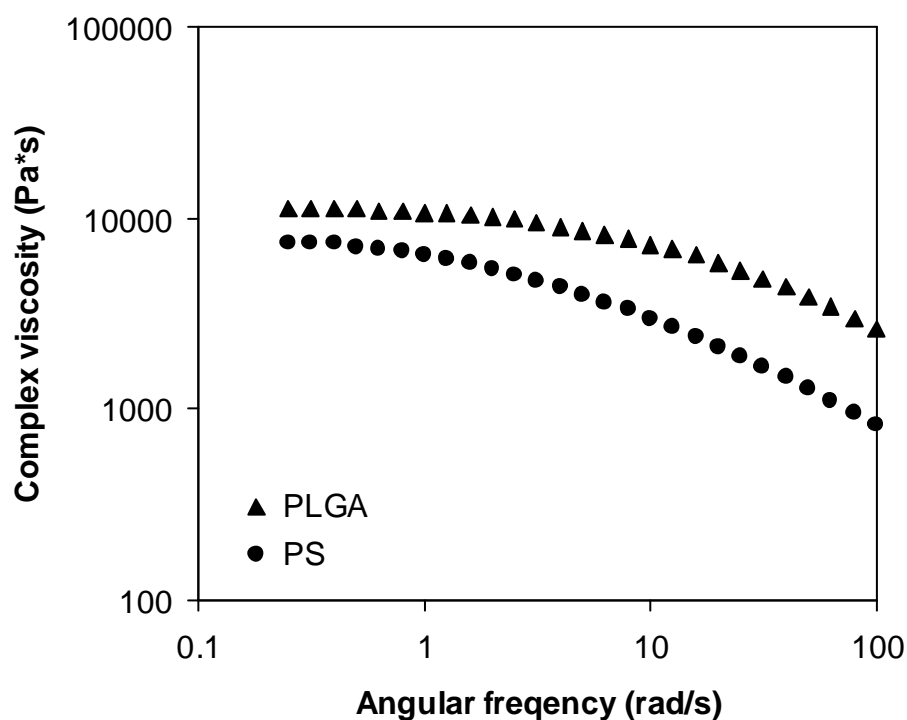
Figure 5.7: Complex viscosity *vs.* angular frequency at 200°C for PS and PLGA.

5.4.4 Rheology

All parallel-plate rheological tests were carried out at 1 mm gap size and under small-strain oscillatory shear in the linear viscoelastic range. In order to preserve the original morphology, the initial heating and delaying time was minimized during the test. The relations of complex viscosity and angular frequency at 200°C for the pure polymers are given in Fig. 5.7. Using the well-known Cox-Merz rule[3] for shear viscosity of pure polymers, one can convert angular frequency equivalently to shear rate. From the resulting shear rate dependency, it is seen that both polymers are highly

pseudoplastic, with viscosity decreasing with the increase of shear rate. Two types of viscosity were important in the current study. First, the viscosities and their ratio at the processing shear rate during batch mixing were major factors affecting the phase structure of the blend. For example, the phase inversion could be related to the viscosity ratio.[18] Second, for a particulate blend, the viscosity is also expected to affect the particle migration/diffusion process. Classical theory such as the Stoke-Einstein equation[4] predicts an inverse relation between the diffusion coefficient and the viscosity.

For the blends, mixing was performed at 60 rpm and 200°C. The shear rate at this mixing speed with a rotor diameter of 35.5 mm was estimated to be 100 s^{-1}. The viscosity ratio of PLGA over PS in this case was around 3, calculated from the data in Figure 5.6. For a 50/50 wt% PLGA/PS blend used in this study, this viscosity ratio could result in a co-continuous phase morphology. However, for the procedure in which PLGA and HA were premixed before mixed with PS to form the tertiary blend, the viscosity of the PLGA/HA blend should be used for final blend morphology prediction instead of the viscosity of PLGA. It is known that, addition of inorganic particles into polymers typically causes a viscosity increase and the actual value increases with increasing particle concentration. This can be used to explain the difficulty in forming a co-continuous phase structure using the two-step mixing approach (cf. Fig. 5.4).
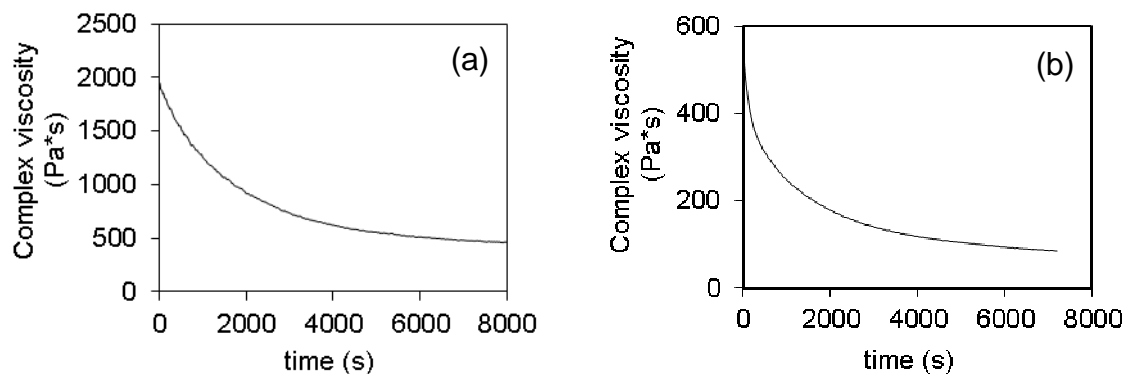
Figure 5.8: Small-strain time sweep data of a PLGA/PS blend (50/50 wt%) at 200°C and two different angular frequencies: (a) 1 rad/s and (b) 100 rad/s.

To prepare samples for parallel-plate rheometry, the blends were compression

molded into 1.2 mm thick sheets and cut into 25 mm diameter discs. During time- and

frequency-sweep tests, the gap size and strain amplitude were fixed at 1 mm and 0.01,

respectively. In Fig. 5.8, time sweep testing results of PLGA/PS 50/50 wt% blend at 1

and 100 rad/s angular frequencies were summarized. For this binary blend, steady

decrease in complex viscosity was found for both angular frequencies. This

phenomenon might be attributed to the decrease in total interfacial area due to phase

0coarsening during annealing of the co-continuous blend.

Fig. 5.9 shows different rheological behaviors of HA ternary blends prepared

by different mixing procedures. The time-sweep data of the blend prepared using

single-step mixing is shown as Curve A in the figure. The angular frequency applied in

this test was 1 rad/s and the testing temperature was 200°C. For comparison, the blend

with the same composition but made through two-step mixing was tested under the

same conditions, and the data is shown as Curve B in the figure. Despite the similar

complex viscosity values at the start, the two blends showed a different time dependency of viscosity. Blend A experienced a large increase in viscosity over a long period of time (~20 min) before a viscosity peak was reached. The increase of viscosity in this period of time exceeded 100%. In contrast, blend B only showed a mild increase in viscosity, approximately 8%, and the viscosity peak was reached in a much shorter time, about 6 min. The different responses of the two different blends during testing may be accredited to different structural evolution processes. For blend A, there existed a significant particle migration process; that is, the HA particles migrated from the PS phase to the PLGA phase during testing, causing an increase in viscosity of the blend.
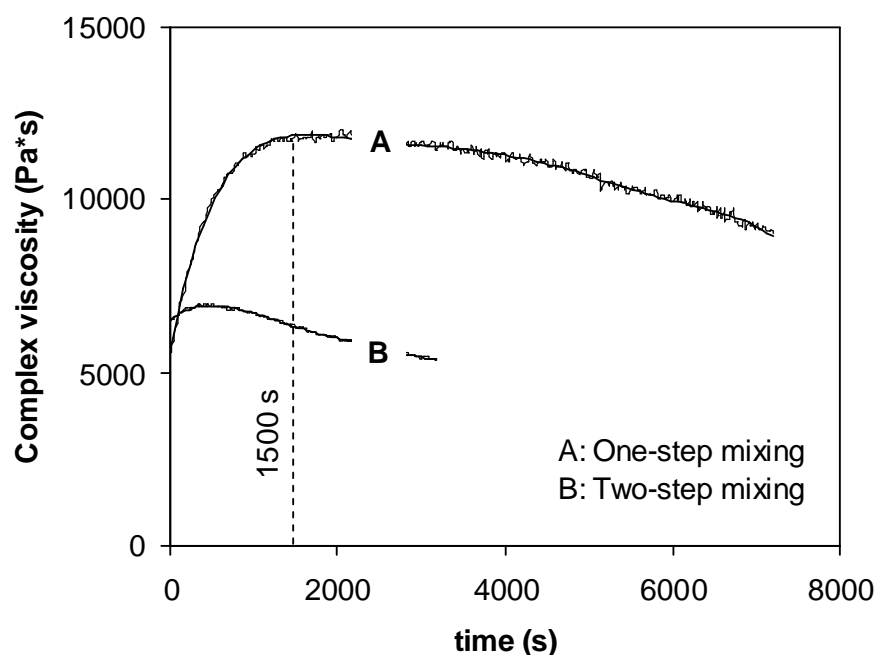
Figure 5.9: Small-strain time sweep data of PLGA/PS/HA blends (40/40/20 wt%) at 200°C and 1 rad/s angular frequency. Blend A was prepared by single-step mixing, and blend B was prepared by two-step mixing.

This explanation is consistent with the morphological observations obtained in SEM and XRT. By comparison, for blend B, the particle migration process is expected to be a weak process during testing since the HA particles were already in the PLGA phase at the beginning of testing due to premixing. PLGA/PS blends without HA were also tested in parallel-plate rheometry under the identical conditions as those for the tertiary blends. Without HA nanoparticles, the viscosity of the blend decreased monotonically. This provides further evidence that particle migration was the major mechanism causing the viscosity increase in the tertiary blends.

Nanoparticle migration in immiscible polymer blends was also revealed in previous publications, but mostly dealing with a dispersed morphology [26, 27, 39, 11].

Possible driving forces for particle migration in such systems can be derived from the difference in chemical affinity between the nanoparticles and the different polymer components. The particles tend to migrate to the polymer phase exhibiting stronger chemical/physical interactions with the additive. Utilizing this mechanism, one can control the migration of nanoparticles in immiscible polymer blends. In particular, one can move nanoparticles form a sacrificial phase to the desired polymer phase.

Parametric experiments were conducted on blend A to study the effects of oscillation frequency and processing temperature on the migration kinetics. The migration time of HA nanoparticles under different conditions were measured. From the morphological observations and rheological behaviors of the PLGA/PS/HA blends (as described in the previous sections), it appeared reasonable to use the peak viscosity time as the characteristic time for particle migration. During testing, two levels of temperature,
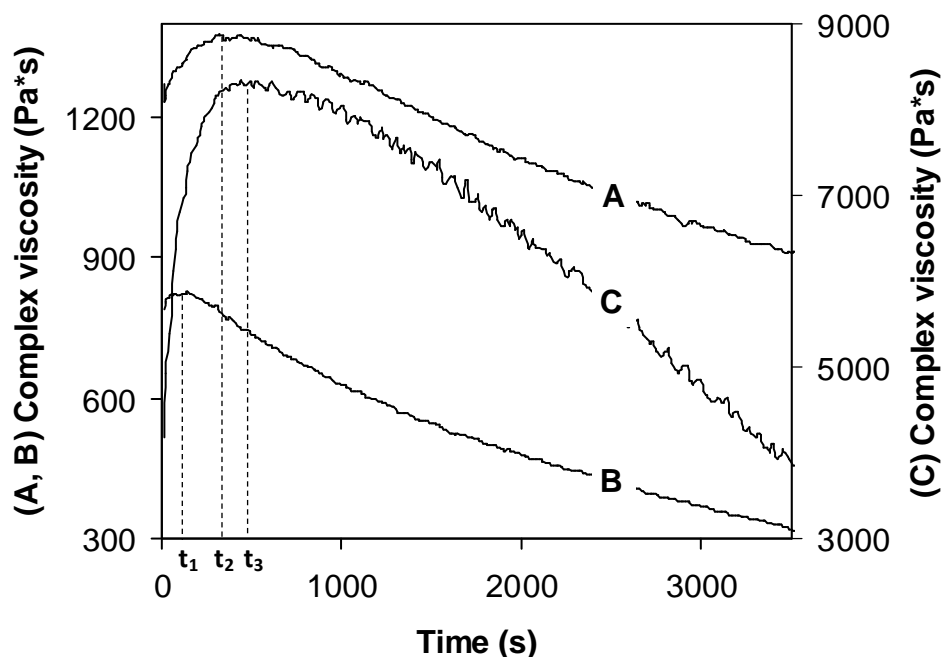
Figure 5.10: Small strain time sweep data of PLGA/PS/HA blends (40/40/20 wt%) under different testing conditions: (A) at 200°C and 100 rad/s angular frequency; (B) at 220°C and 100 rad/s angular frequency; (C) at 220°C and 1 rad/s angular frequency. The peak times are indicated in the figure as $t_1 = 140$ s, $t_2 = 360$ s, and $t_3 = 500$ s.

200 and 220°C, and two levels of angular frequency, 1 and 100 rad/s, were employed, producing four different testing data sets. The viscosity data are given in Fig. 5.10. Note that the data for 200°C and 1 rad/s has already been given in Fig. 5.9 and thus not reproduced. The viscosity obtained in all these tests experienced a considerable increase in the initial stage of testing. However, the time scale for reaching the peak viscosity differed in different testing conditions. Furthermore, the magnitude of viscosity was significantly dependent on the testing conditions. The temperature dependency and the shear rate dependency of viscosity can be clearly seen in the data. Particularly, the viscosity is expected to be lower at a higher temperature. Likewise, the

increase in testing frequency can cause a reduction in the viscosity magnitude due to the shear-thinning behavior or pseudoplasticity of the polymeric material.

Table 5.1: Shear viscosities of PLGA and PS at different angular frequencies and temperatures.

Angular frequency	Material	Component viscosity (Pa-s)		Arithmetically combined viscosity at 50/50 wt%	
		@ 200°C	@ 220°C	@ 200°C	@ 220°C
1 rad/s	PS	6400	1900	8550	3250
	PLGA	10700	4600		
100 rad/s	PS	828	500	1739	1130
	PLGA	2650	1760		

Table 5.2: Comparison between experimental peek times with the predicted migration time from the ξ parameter ($\xi = T/\eta$). The data are all normalized with those at the reference state, 200°C and 1 rad/s. The subscript r refers to the reference state.

	200°C, 100 rad/s	220°C, 1 rad/s	220°C, 100 rad/s
Normalized ξ parameter, ξ/ξ_r	0.20	0.36	0.12
Normalized peek time, t/t_r	0.24	0.33	0.09

From the classical diffusion theory [4, 5], temperature and viscosity are expected to be two major parameters affecting the diffusion coefficient. The increase in temperature and the decrease in viscosity would cause an increase in the diffusion coefficient. Based on this theory, it would be interesting to define a new parameter, $\xi = T/\eta$, and analyze the data in Fig. 5.10 in terms of this ξ parameter. For a complex blend system as the one involved in this study, the arithmetically combined viscosity of the two polymer components may be deemed as the equivalent viscosity affecting the particle migration process. Table 5.1 summarizes the testing conditions, the complex viscosities, and the arithmetically combined viscosities. From these data, normalized ξ parameters (ξ/ξ_r) and normalized peak times (t/t_r) were calculated and summarized in Table 2. The test at 200°C and 1 rad/s was chosen as a reference state. From Table 5.2, it can be seen that the normalized peak times are nearly equal to the normalized ξ parameters for testing cases, at least from the first order approximation. This simple method for predicting the viscosity peak time, and consequently the characteristic particle migration time and the kinetics, could be useful for complex blend systems as the one employed in this study.

5.5   Conclusions

In this work, a new technique for processing interpenetrating microporous material with high nanoparticle loading was developed and investigated. A tertiary polymer blend PLGA/PS/HA (40/40/20 wt%) was chosen as a model system. The blend prepared under conditions for formation of a co-continuous structure was annealed

under small-strain oscillatory shear between two parallel plates. The results from different characterizations suggested that the applied small-strain oscillation substantially accelerated the migration of HA nanoparticles during annealing from the PS phase to the PLGA phase; nearly all HA particles were uniformly presented in the PLGA phase after 20 min annealing at 200°C. After dissolution of the PS phase, a PLGA/HA composite material with interconnected microporous structure was successfully produced. The HA particle loading in the PLGA phase exceeded 30 wt%. Two different mixing strategies, i.e. single-step mixing and two-step mixing, were compared. The results showed that only the single-step method yielded a desirable porous PLGA composite material with interpenetrating microchannels, while the two-step approach produced an undesired droplet-in-matrix phase structure. Parametric studies on the effect of temperature and the oscillation frequency on the particle migration process were also conducted. Based on the experimental data, absolute temperature divided by arithmetically combined viscosity was suggested as the dominant parameter depicting the kinetics of the HA nanoparticle migration process during post-annealing under small-strain oscillation.

5.6   References

1. Ang TH, Sultana FSA, Hutmacher DW, Wong YS, Fuh JYH, Mo XM, Loh HT, Burdet E and   Teoh SH 2002 Fabrication of 3D chitosan-hydroxyapatite scaffolds using a robotic dispensing system *Mater. Sci. Eng. C* **20** 35–42

2. Bos RRM, Rozema FR, Boering G, Nijenhuis AJ, Pennings AJ 1991 Verwey AB, Nieuwenhuis P and   Jansen HWB 1958 Degradation of and Tissue Reaction to Biodegradable Poly (L-lactide) for Use as Internal Fixation of Fractures – A Study in Rats *Biomaterials* **12** 32-36

3. Cox WP and Merz EH, Correlation of Dynamic and Steady Flow Viscosities 1958 *J. Polym. Sci.* **28**   619–22

4. Einstein A 1908 Elementary theory of the Brownian motion *Zeitschrift für Elektrochemie und angewandte physikalische Chemie* **14** 235-39

5. Elias L, Fenouillot F, Majeste JC, Alcouffe P and   Cassagnau P 2008 Immiscible polymer blends stabilized with nano-silica particles: Rheology and effective interfacial tension *Polymer* **49** 4378–85

6. Freed LE, Marquis JC, Nohria A, Emmanual J, Mikos AG and Langer R 1993 Neocartilage formation in vitro and in vivo using cells cultured on synthetic biodegradable polymers *J. Biomedical Materials Research* **27** 11-23

7. Goldstein AS, Zhu G, Morris GE, Meszlenyi RK and Mikos AG 1999 Effect of Osteoblastic Culture conditions on the structure of poly(DL-lactic-co-glycolic acid) foam scaffolds *Tissue Engineering* **5** 421-433

8. Harris LD, Kim BS and Mooney DJ 1998 Open pore biodegradable matrices formed with gas foaming *J. Biomed. Mater. Res.* **42** 396–02

9. Higashi S, Yamamuro T, Nakamura T, Ikada Y, Hyon SH and Jamshidi K 1986 Polymer Hydroxyapatite Composites for Biodegradable Bone Fillers *Biomaterials* **7** 183-87

10. Hollinger JO, Battistone GC. Biodegradable Bone Repair Materials -Synthetic-Polymers and Ceramics 1986 *Clinical Orthopaedics and Related Research* **207** 290-05

11. Hong JK, Kim YK, Ahn KH and Lee SJ 2008 Shear-induced migration of nanoclay during morphology evolution of PBT/PS blend. *Journal of Applied Polymer Science* **108** 565-75

12. Hoque ME, Hutmacher EW, Feng W, Li S, Huang, MH, Vert M and Wong YS 2005 Fabrication using a rapid prototyping system and in vitro characterization of PEG-PCL-PLA scaffolds for tissue engineering *J. Biomater. Sci. Polymer Edn* **16** 1595-10

13. Landers R and Mlhaupt R 2000 Desktop manufacturing of complex objects, prototypes and biomedical scaffolds by means of computer-assisted design combined with computer-guided 3D plotting of polymers and reactive oligomers. Macromol *Mater.   Eng.* **282** 17–21

14. Lo H, Kadiyala S, Guggino SE and Leong KW 1996 Poly(L-lactic acid) foams with cell seeding and controlled-release capacity *J. Biomed. Mater. Res*. 30 475–84

15. Lo H, Ponticiello MS and Leong KW 1995 Fabrication of controlled release biodegradable foams by phase separation *Tissue Eng.* **1** 15–28

16. Mikos AG, Thorsen AJ, Czerwonka LA, Bao Y, Langer R, Winslow DN and Vacanti JP 1994 Preparation and characterization of poly(L-lactic acid) foams *Polymer* **35** 1068-77

17. Mikos AG, Bao Y, Cima LG, Ingber DE, Vacanti JP and Langer R 1993 Preparation of poly (glycolic acid) bonded fiber structures for cell attachment *J. Biomed. Mater. Res.* **27** 183-9

18. Miles IS, Zurek A 1988 Preparation, structure, and properties of two-phase co-continuous polymer blends *Polym. Eng. Sci.* **28**, 796-805

19. Mooney DJ, Mazzoni CL, Breuer C, McNamara K, Hern D and Vacanti JP 1996a Stabilized poly glycolic acid fibre-based tubes for tissue engineering *Biomaterials* **17** 115-24

20. Mooney DJ, Baldwin DF, Suh NP, Vacanti JP and Langer R 1996b Novel approach to fabricate porous sponges of poly(D,L-lactic-co-glycolic acid) without the use of organic solvents *Biomaterials* **17** 1417–22

21. Nam YS and Park TG 1999 Biodegradable polymeric microcellular foams by modified thermally induced phase separation method *Biomaterials* **20** 1783–90

22. Nam YS, Yoon JJ and Park TG 2000 A novel fabrication method of macroporous biodegradable polymer scaffolds using gas foaming and salt as a porogen additive *J. Biomed. Mater. Res., Appl. Biomater.* **53** 1–7

23. Park A, Wu B and Griffith LG 1998 Integration of surface modification and 3D fabrication techniques to prepare patterned poly(L-lactide) substrates allowing regionally selective cell adhesion *J. Biomater. Sci. Polym. Ed.* **9** 89–110

24. Park TG 1999 New approaches to fabricate highly porous tissue scaffolds *The Fourth Asia-Pacific conference on medical and biological engineering, Seoul, Korea*

25. Potschke P and Paul DR 2003 Formation of Co-continuous structures in melt-mixed immiscible polymer blends *J. Macromole. Sci.-Polymer Reviews C* **43** 87-141

26. Potschke P, Bhattacharyya AR and Janke A 2004 Carbon nanotube-filled polycarbonate composites produced by melt mixing and their use in blends with polyethylene *Carbon* **42** 965–69

27. Potschke P, Kretzschmar B and Janke A 2007 Use of carbon nanotube filled polycarbonate in blends with montmorillonite filled polypropylene *Composites Science and Technology* **67** 855–60

28. Schugens C, Maquet V, Grandfils C, Jerome R and Teyssie P 1996 Polylactide macroporous biodegradable implants for cell transplantation II preparation of polylactide foams for liquid–liquid phase separation *J. Biomed. Mater. Res.* **30** 449–61

29. Shastri VP, Martin I and Langer R 2000 Macroporous polymer foams by hydrocarbon templating *Proc. Natl. Acad. Sci., USA* **97** 1970–75

30. Singh L, Kumar V and Ratner BD 2004 Generation of porous microcellular 85/15 poly(D,L-lactide-co glycolide) foams for biomedical applications *Biomaterials* **25** 2611–7

31. Sparacio D and Beckman EJ 1997 Generation of microcellular biodegradable polymers in supercritical carbon dioxide. *Polymer Preprints Division of Polymer Chemistry. American Chemical Society* **38** 420–23

32. Taboas JM, Maddox RD, Krebsbach PH and Hollister SJ 2003 Indirect solid free form fabrication of local and global porous, biomimetic and composite 3D polymer-ceramic scaffolds *Biomaterials* **24** 818-94

33. Thomson RC, Yaszemski MJ, Powers JM and Mikos AG 1998 Hydroxyapatite fiber reinforced poly(a-hydroxy ester) foams for bone regeneration *Biomaterials* **19** 1935-43

34. Wang XX, Li W and Kumar V 2006 A method for solvent-free fabrication of porous polymer using solid-state foaming and ultrasound for tissue engineering applications *Biomaterials* **27** 1924–29

35. Whang K, Thomas CH, Healy KE and Nuber G 1995 A novel method to fabricate bioabsorbable scaffolds *Polymer* **36** 837–42

36. Yao D, Zhang W and Zhou JG 2009 Controllable Growth of Gradient Porous Structures. *Biomacromolecules* **10** 1282-6

37. Yuan ZH and Favis BD 2004 Macroporous poly(L-lactide) of controlled pore size derived from the annealing of co-continuous polystyrene/poly(L-lactide) blends *Biomaterials* **25** 2161-70

38. Yuan ZH and Favis BD 2005 Coarsening of immiscible co-continuous blends during quiescent annealing *AIChE Journal* **51** 271-80

39. Zhao JF and Huang HX 2008 Migration of nanoclay in PP/PS blend and effect of its location on cell structure *Proceedings of IMECE*

CHAPTER 6

MICROPATTERNING OF POROUS STRUCTURES FROM

CO-CONTINUOUS POLYMER BLENDS

6.1 Introduction

Due to their large internal surface area, porous materials have been widely used in applications where high surface activity is desired. Example applications are extracellular scaffolds for tissue engineering [1, 2], porous substrates for catalytic reaction [4, 5], and permeable media for membrane filtration [98, 99]. In addition to the internal porous structure, some emerging applications, such as cell aligning scaffold [100-85], micro fluidic devices [92-17], micropatterned porous electrodes [96, 97], fuel cell membranes [20-25], etc., further desire these materials be shaped into specific geometries including micropatterns.

In contrast to the immense literature in porous material generation, micropatterning of porous devices remains a technical challenge. Most well known techniques for processing porous materials, such as gas foaming, powder sintering, and solid freeform fabrication, have limited capability due to their relatively poor morphological control and/or low geometrical resolution at smaller sizes. Recently, Wessling and coworkers [26, 27] developed a phase separation micromolding process for generating micropatterns with internal pores down to submicron sizes. They cast a concentrated polymer solution into a micropatterned mold and employed freeze drying

or coagulation for extracting the solvent and forming the desired porous structure. This process has been used for generating micropatterned devices, such as microsieves [98, 99] and porous scaffolds [100-85], for filtration and biomedical applications. However, there are some fundamental limitations with this process. The use of a large amount of solvent leads to a slow and environmentally unfriendly process. More critically, the pore size and its distribution from this thermodynamically unstable process are hard to control. The resulting devices also tend to have a dense skin formed which is undesired in filtration and scaffolding applications.

A desired process for micropatterning porous devices would be able to *in situ* control the generation of the porous structure while achieving high geometrical patterning accuracy. One versatile technique for controllable generation of a co-continuous phase morphology is immiscible polymer blending [106-112]; a porous structure can be produced by extraction of the sacrificial polymer. By tuning the material and process parameters, one can generate a desired porous structure with well-defined pore size and distribution. Particularly, the authors [115, 116] have developed techniques for controllable growth of gradient porous structures by regulating the boundary conditions during an in-mold annealing process. In the mean time, there has also been extensive work on precision micropatterning of polymers [117, 118]. It would therefore be interesting to explore the feasibility of combining co-continuous polymer blending with precision micropatterning for creating micropatterned porous devices.

In this study, co-continuous polymer blending was combined with hot embossing, a widely used micropatterning technique, for fabrication of micropatterned

porous devices. A salient feature of this new process is that a controllable in-mold annealing stage is applied to the embossed blend to regulate its structural evaluation. A special effort was made to generate an open pore structure at the mold contact surface. Parametric experimental studies were conducted on stamps with different feature sizes under different processing conditions. The results demonstrated the feasibility and the versatility of the proposed technique in fabricating micropatterned porous structure with controllable morphology.
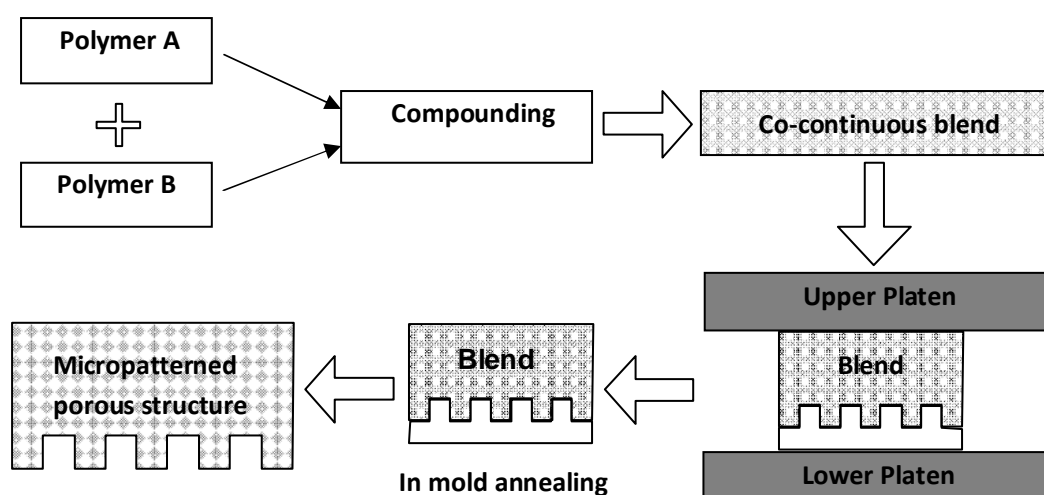
Figure 6.1: Process sequence for micropatterning of porous structures.

6.2   Fabricating technique

The process sequence used in the new process for fabricating micropatterned porous materials is shown in Fig. 6.1. Initially, two immiscible polymers are melt mixed under suitable conditions to form a co-continuous blend with phase size in the micrometer range. The quenched blend is then reheated above the softening temperatures (i.e.,

glass transition temperature for amorphous polymer or melting temperature for semicrystalline polymer) of both polymer components and hot-embossed (or compression molded) in a heated mold. After the embossing stage, the embossed blend further undergoes an in-mold annealing stage where controlled phase evolution occurs for generating the desired morphology. Finally, after cooling and demolding of the embossed article, one polymer component is selectively extracted, leaving behind a porous micropattern.

The critical step is this special hot embossing process is in-mold annealing. In contrast with the standard hot embossing process for purely geometrical patterning purposes, the new process is able to control the evolution of the internal phase structure. First, the initial phase structure will be coarsened from thermal annealing effects. Due to the interfacial tension, the interfacial area between the polymer components will decrease, resulting in a larger phase size. Second, the phase structure can further be regulated by applying proper boundary conditions during in-mold annealing. Particularly, by employing a temperature different at the boundary, a gradient phase structure can be generated, as demonstrated in the authors' previous work [115]. Furthermore, varied kinematical and dynamical conditions at the mold surface can be utilized for fine controlling the phase structure near the surface. It has been found that different chemical interaction at the mold surface can yield a different surface morphology [116]. By modifying the mold surface properties, different morphology including a segregated layer and co-continous dual phases can be generated right at the surface. Last but not least, geometrical confinement can also be used in the annealing

step to influence the coarsening kinetics and produce globally or locally aligned microporous structures.

6.3 Experimental

6.3.1 Materials

The two polymers, poly(lactic acid) (PLA) and polystyrene (PS), used in this study were obtained from commercial sources. The PLA was a semicrystalline polymer produced by NatureWorks LLC under the product name of INGEO™ 6202D. It has Tg (glass transition temperature) of 55 °C and Tm (melting temperature) of 165 °C as measured by DSC (differential scanning calorimeter), model TA-Q200 from TA Instruments, with temperature rate of 10 °C/min. The PS was provided by Dow Chemical under the product name of Styron 675. The Tg for this polymer was determined to be 95 °C. The thermal stability of these resins was examined using TGA (thermal gravimetric Analyzer), model TA-Q5000IR from TA Instruments, with a heating rate of 10 °C/min in a nitrogen environment. The thermal degradation temperatures of PLA and PS were determined to be 270 and 380 °C, respectively. To minimize the hydrolysis of the PLA, both polymers were dried inside a vacuum oven at 90 °C for 12 hr prior to melt processing.

6.3.2 *Blending*

The dried PLA and PS at a 50/50 weight ratio were melt mixed in a recirculating batch mixer (RCPBM-2000, Randcastle extrusion systems Inc.) at 180 °C and 30 rpm with nitrogen purging. The mixing operation was stopped when an equilibrium torque was achieved. While still molten, the mixture was scraped out and quenched into tap water to preserve the blend morphology. The solidified blend was dried in a vacuum oven for 6 hr at 90 °C and stored in a desiccator before hot embossing.

(a)   (b)
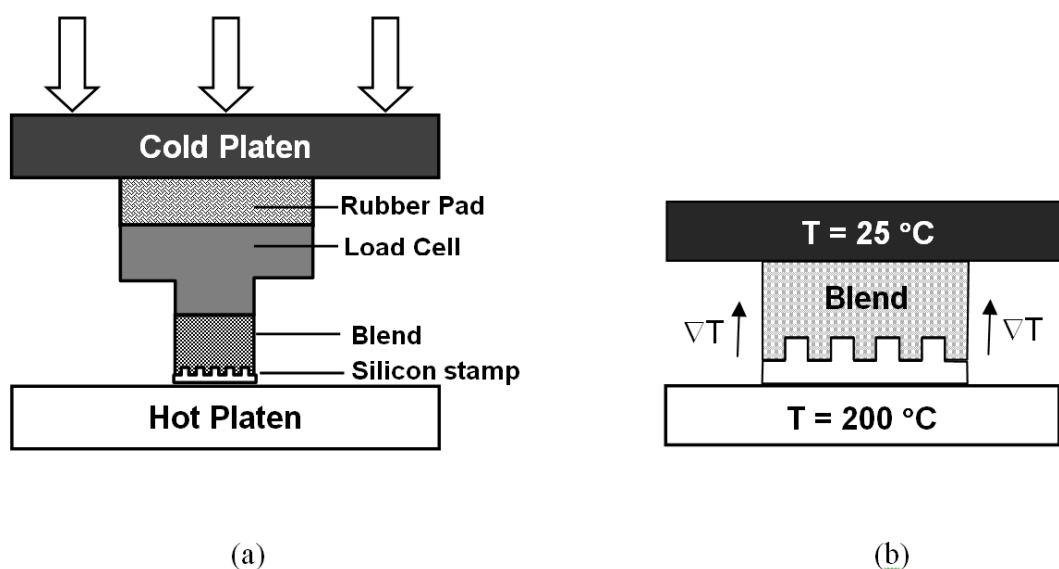
Figure 6.2: Experimental setups for (a) hot embossing and (b) in-mold annealing.

6.3.3 Hot embossing

The experimental setup for hot embossing, retrofitted onto a hydraulic press with upper and lower platens, is illustrated in Fig. 6.2.a. Silicon stamps with square microchannels, as shown in Fig. 6.3, were used as the embossing mold. Samples with dimension of 1 x 0.5 x 0.5 cm (length by width by thickness) were cut from the as-mixed blend. The sample surface was polished with a fine sand paper. The polished sample was preheated in an oven set at the same temperature as the target embossing temperature. Once reaching the target temperature, the sample was immediately removed from the oven and hot embossed against the silicon stamp placed on the lower heated platen of the hot press. The combined embossing and holding stages were carried out under constant pressure control. A load cell (LCM305-2KN, Omega Inc.) installed on the upper platen was used for pressure monitoring. A rubber pad, approximately 10 mm thick, inserted between the load cell and the upper platen was used to facilitate uniform

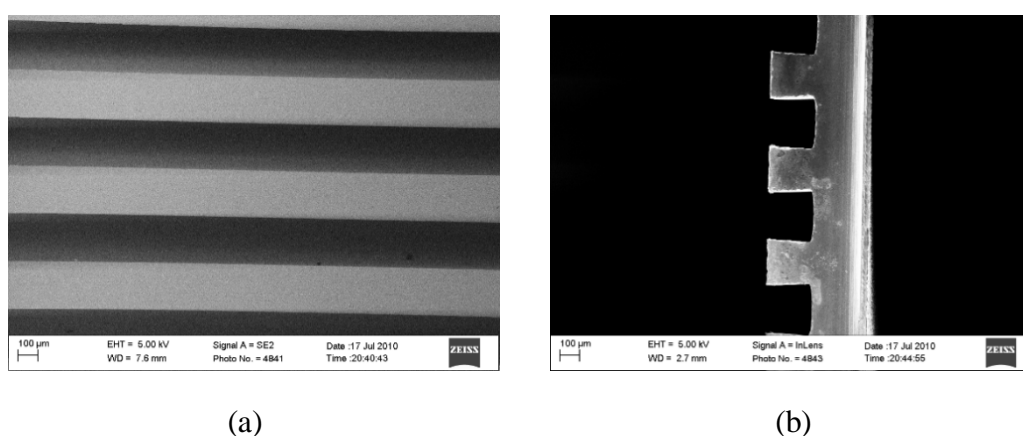(a)   (b)

Figure 6.3: Geometry of silicon stamps used for hot embossing: (a) top view; (b) side view.

transfer of the embossing pressure. The total embossing and holding time was set to be 1 min, of which the initial pressure loading step (i.e., the embossing step) took about 5 s and the holding stage used the remaining 55 s. The primary experimental parameters investigated in this study included the embossing force (10, 20, 50, and 80 N), the embossing temperature (100, 120, 140, 160, and 180 °C), and the microchannel size (10, 50, and 250 µm) on the stamp.

6.3.4 *In-mold annealing*

The tendency for a co-continuous blend structure to coarsen during thermal annealing offers the opportunity to control internal morphology without using complex setups. To determine a suitable scheme for morphology control in micropatterning, three different annealing protocols/sequences were investigated.

In the first approach, the as-mixed blend was first hot embossed using the procedure described in the previous section. At the end of the holding stage, the embossed polymer blend and the silicon stamp (without ejection) were placed inside an oven at 180 °C for thermal annealing, with constant nitrogen purging. After annealing, the molten blend together with the mold was quenched into tap water. This sequential embossing and thermal annealing approach is denoted as the "E-A" approach in the later discussion.

In the second approach, the sequence of hot embossing and annealing was inverted. The annealing step was first conducted to grow the blend phase structure to

the desired size; then, the annealed blend was hot embossed against the silicon stamp. This annealing and embossing sequence is abbreviated as "A-E" in the later discussion.

The third approach is a further modification of the first one. Specifically, the annealing step was modified to include a gradient thermal field. Instead of a convective oven, a hot press with a differential temperature setup, as shown in Fig. 6.2.b, was employed. The bottom platen was set at 200 °C while the upper platen was kept at room temperature. By doing this, a temperature gradient was generated in the direction perpendicular to the platen surface. During the entire in-mold annealing process, a small force was applied to maintain the contact but not to deform the material. This embossing and gradient annealing sequence is referred to as "E-GA" for further reference.

6.3.5 Extraction of sacrificial polymer

Samples with desired phase structures and micropatterns were submerged into cyclohexane at 75 °C for 24 h to selectively remove the PS phase and form a PLA mircoporous structure. This dissolution process was monitored by measuring the weight loss of the sample. The dissolved samples were collected and dried thoroughly under vacuum at 80 °C for at least 4 hr to remove the residual solvent.

6.3.6 Characterization

Rotational rheometry was conducted to understand the flow behavior of the two polymer resins. The measurement was performed on a parallel-plate rheometer (AR

2000se, TA Instruments) with varied temperature and frequency. The instrument was operated under a small-strain oscillatory mode in the linear viscoelastic region. SEM (scanning electron microscopy) was used for observing the pattern geometry and the microporous structure. To prepare the SEM sample, the dried porous patterns were brittle fractured in liquid nitrogen and sputter coated with gold.

6.4   Results and Discussion

6.4.1 Formation of a co-continuous phase structure

The well-known criterion for formation of a co-continuous phase morphology by blending two immiscible polymers is that the shear viscosity ratio of the two polymer components is equal to their concentration ratio [44]. This phase inversion criterion was used to determine the mixing conditions in the present study.

Fig. 6.4 shows the parallel-plate rheometry data for PLA and PS. The complex viscosity was obtained under a frequency sweep mode at two different temperatures, 180 and 200 °C. Under these temperatures, both polymers show typical pseudoplastic behavior with an obvious shear-thinning at high frequency in the testing range. Based on the geometrical parameters of the batch mixer, the shear rate applied to the blend during mixing was estimated to be 100 s^{-1}. At this shear rate and a temperature of 180 °C, the viscosity ratio of PLA to PS is around 1, according to the rheological data in Fig. 6.4.
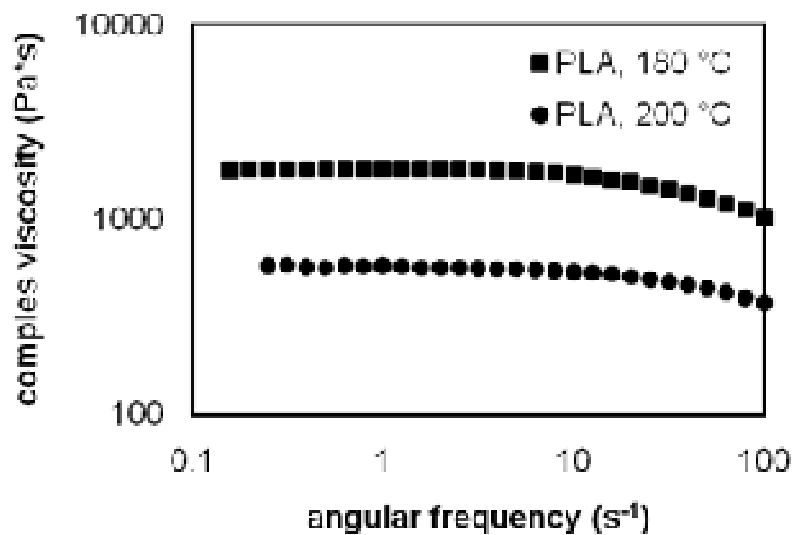
(a)
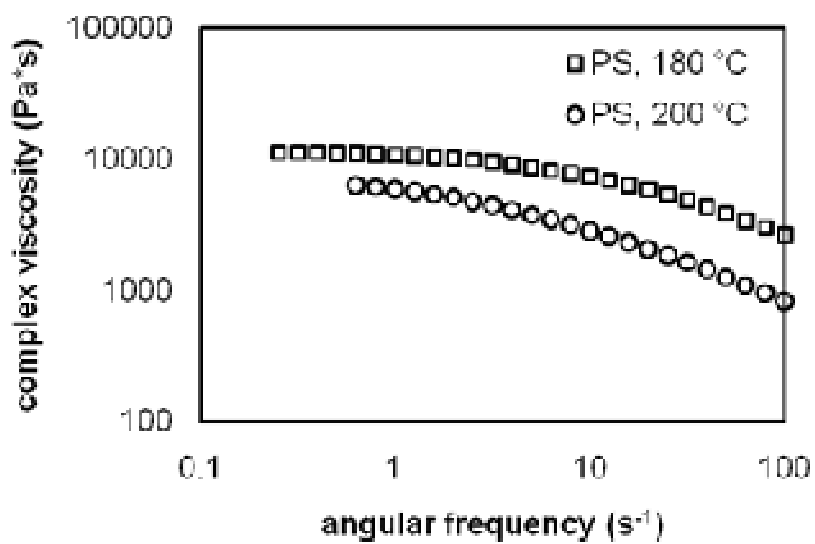
(b)

Figure 6.4: Complex viscosity of PLA and PS at different temperatures: (a) PLA resin; (b) PS resin.
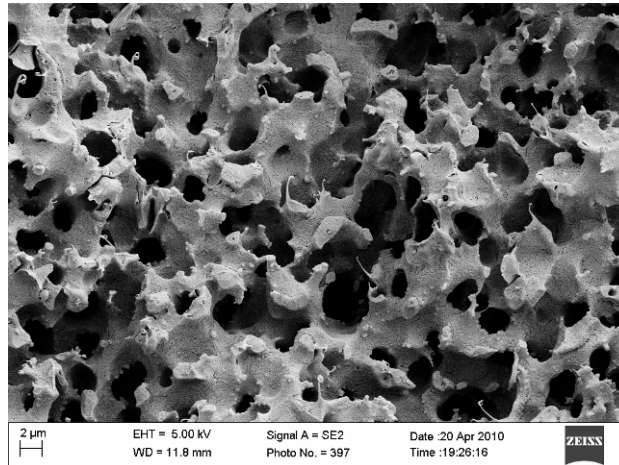
Figure 6.5: Phase morphology of as-mixed PLA/PS 50/50 wt% blend.

Based on the phase inversion criterion mentioned previously, mixing of PLA and PS at 50/50 wt% should lead to a co-continuous phase structure. This was further confirmed by weight loss measurement and SEM observation on samples selectively dissolved by cyclohexane (which is a solvent to PS but not to PLA). From the weight loss test, nearly all PS was extracted from the blend after dissolved in cyclohexane, indicating a nearly 100% co-continuity in the PLA/PS blend. Fig. 6.5 shows an SEM of the porous structure after PS extraction. From this image, the average phase size was estimated to be 5 µm.

6.4.2 Effects of embossing

During embossing, the blend is subjected to a deformation field. The effect of this deformation process on the structural changes was studied first. The silicon stamps with three different feature sizes (10, 50, and 250 µm) were used in this study. Despite

the difference on feature size, all stamps have aspect ratio of 1. Five temperature levels (100, 120, 140, 160, and 180 °C) and four compression force levels (10, 20, 50, and 80 N) were applied to cover a broad rang of processing conditions. Note the temperature employed in the experiment were all above the Tg of PS to ensure the deformability of the blend. Likewise, the low limit of the embossing force, 10 N, was set to achieve a full replication of the groove. Compression force higher than 80 N was not applied as this tended to cause the breakage of the silicon stamp. The total embossing stage lasted for 1 min, and after embossing, the sample was immediate quenched in tap water. For all samples, the PS phase was extracted before SEM imaging.

Fig. 6.6 shows the replication and morphology of samples prepared at 100 °C and 80 N with three different sized stamps. Under these embossing conditions, the silicon grooves are reasonably replicated, except local sharp edges. For all three cases, an orientated structure was observed in regions where primary deformation occurred. One can find that the microstructures were actually stretched and oriented into the cavities on the stamp. At this low embossing temperature, close to Tg of PS and well below the PLA melting temperature, structural recovery or relaxation is anticipated to be insignificant. Therefore, the deformation caused structural orientation can be retained.
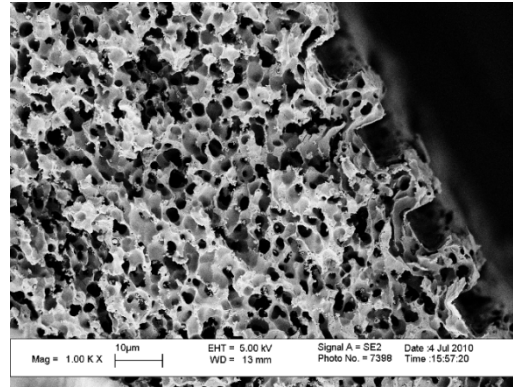
(a)
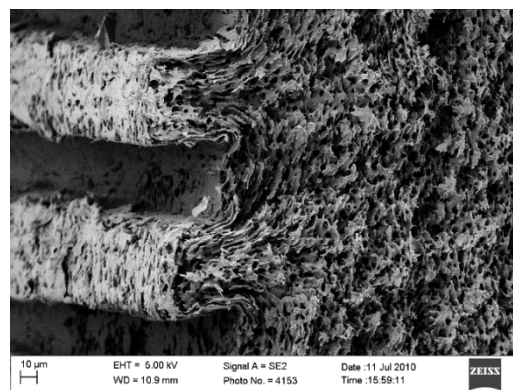
(b)
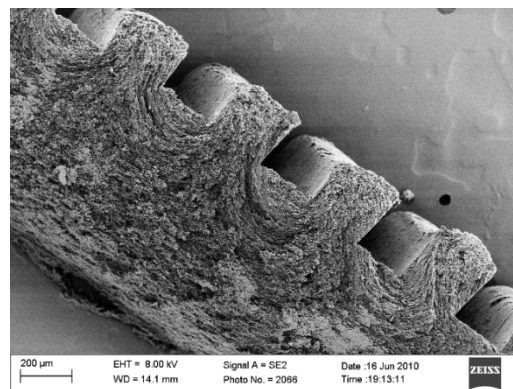
(c)

Figure 6.6: Samples produced at 100 °C and 80 N with stamps of different groove sizes: (a) 10 µm; (b) 50 µm; (c) 250 µm.

The replication and morphology of samples prepared at increased temperatures but still below the PLA melting temperature are shown in Figs. 6.7-6.9, with both side and top views of the embossed structures. From the side view, it can be seen that the morphological orientation was reduced at these higher temperatures. At 160 °C, close to the PLA melting temperature, a nearly isotropic porous structure was found even in those regions where large deformation occurred (Fig. 6.9). The embossed structure after PS extraction also exhibited an open pore structure, even at the outside surfaces. This can be clearly seen from the top views in Fig. 6.7-6.9. At these increased temperatures, the required force for complete filling of the silicon groove was significantly reduced. While a force of 80 N was needed to fill the grooves at 100 °C, only 20 N was needed to fill the grooves at 140 °C.

Embossing experiments at temperature above the PLA melting temperature were also conducted. As an example, Fig. 6.10 shows the replication and morphology of patterns embossed at 180 °C, approximately 15 °C above the PLA melting temperature. At this elevated temperature, only 10 N compression force was needed to achieve complete filling of the microcavities. This reduced embossing force is understandable due to the highly increased fluidity of the blend at a temperature above the T_g or T_m of both components. Under these embossing conditions, faithful pattern duplication was realized, even at the sharp edges of the microgrooves. From the side view in Fig. 6.10, it can be seen that a highly isotropic porous structure was produced at this elevated temperature. Based on these observations, it seems that
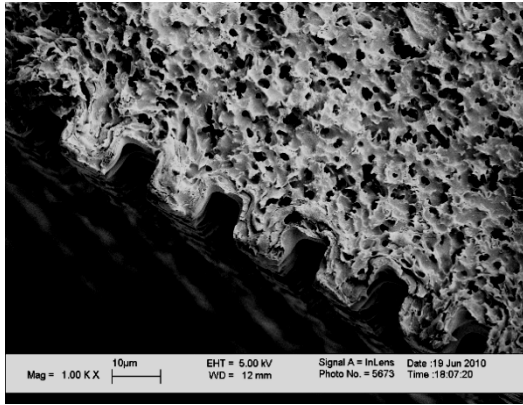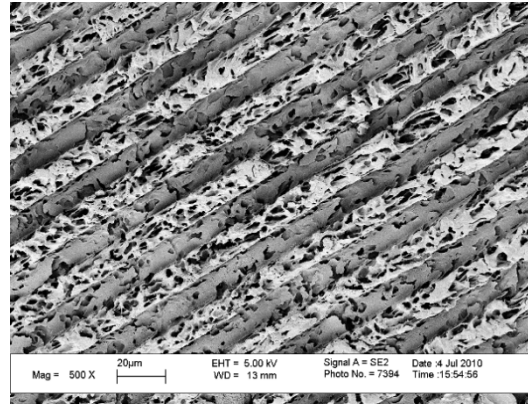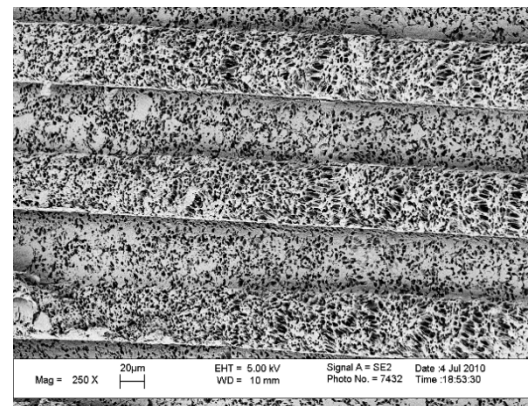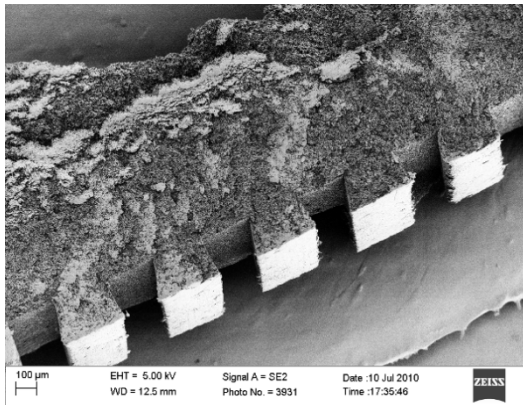
(a1)   (a2)
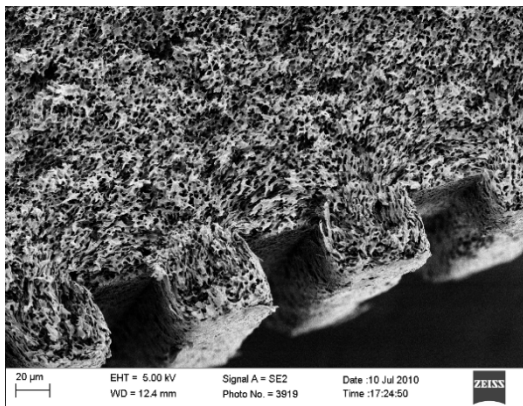
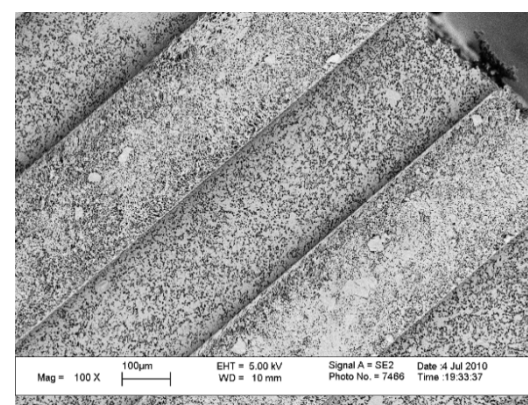(b1)   (b2)
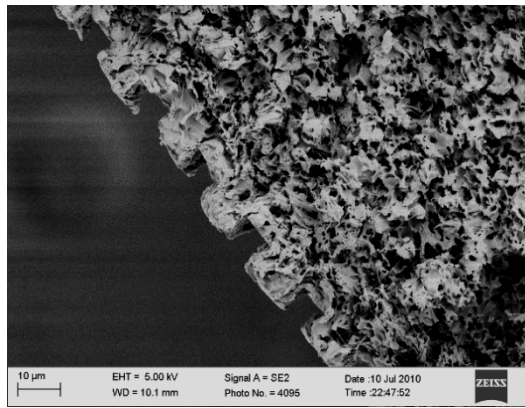

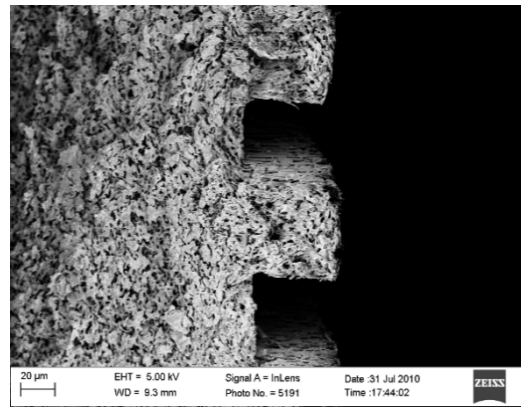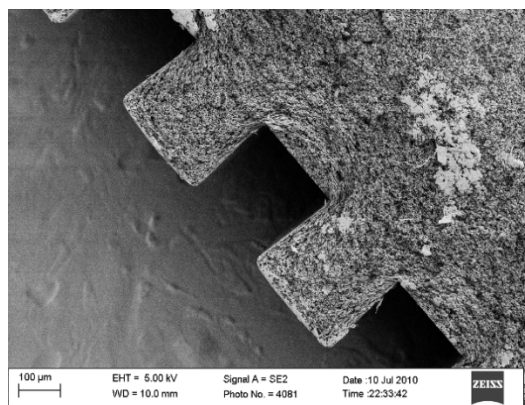(c1)   (c2)

Figure 6.7: Samples produced at 120 °C and 20 N compression force with stamps of different groove sizes: (a1 & a2) 10 µm; (b1 & b2) 50 µm; (c1 & c2) 250 µm.
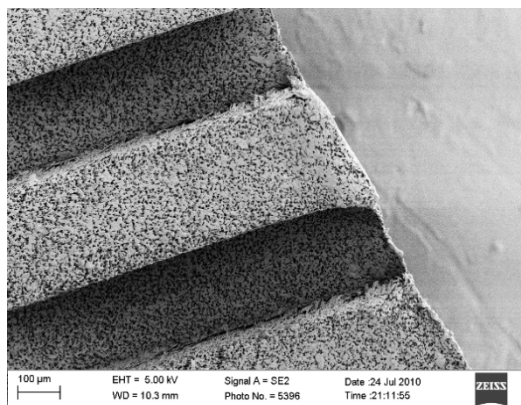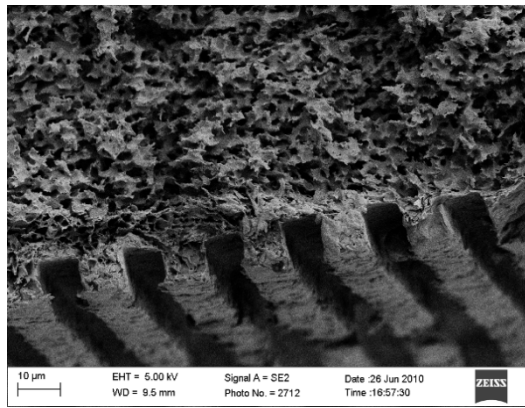
(a)

(b)

(c)

(d)

Figure 6.8: Samples produced at 140 °C and 20 N compression force with stamps of different groove sizes: (a) 10 µm; (b) 50 µm; (c) 250 µm; (d) 250 µm, top view.

(a)   (b)
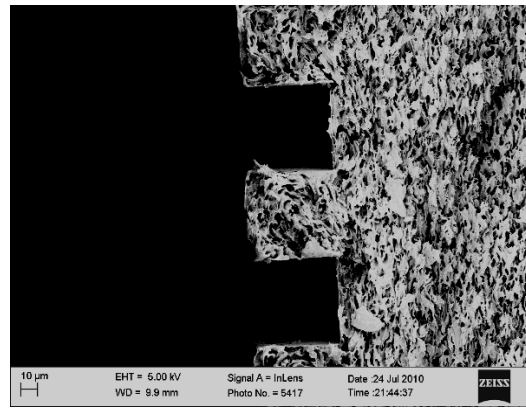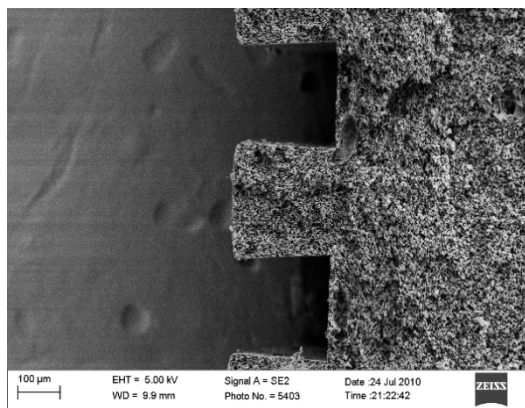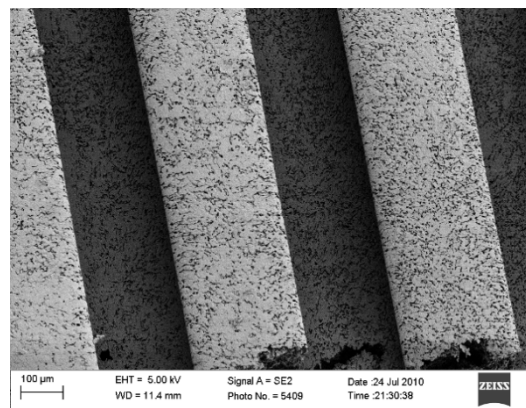
(c)   (d)

Figure 6.9: Samples produced at 160 °C and 20 N compression force with stamps of different groove sizes: (a) 10 µm; (b) 50 µm; (c) 250 µm; (d) 250 µm, top view.

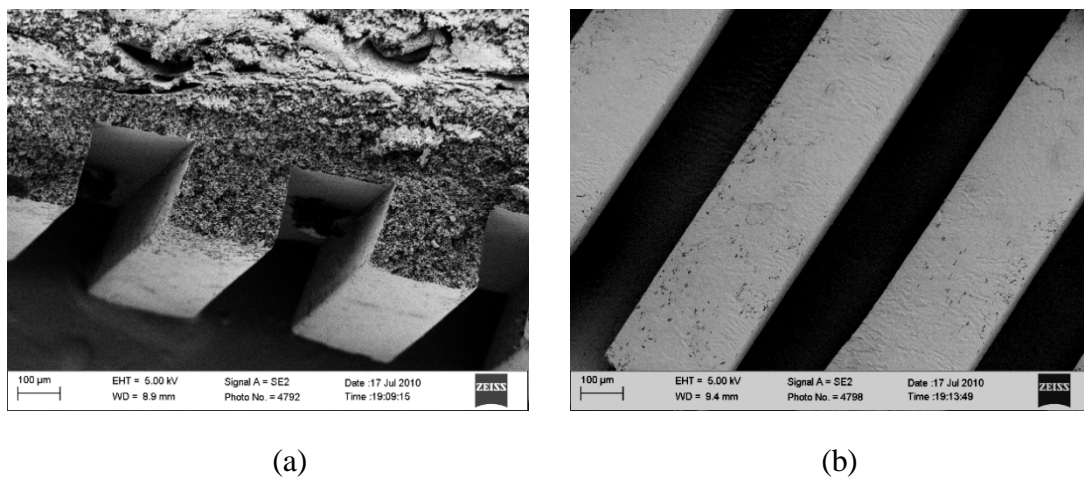(a)   (b)

Figure 6.10: Samples produced at 180 °C and 10 N compression force with a stamp of 250 m groove size: (a) side view; (b) top view.

embossing a completely melted blend is similar to embossing a semi-molten blend at reduced temperatures (Figs. 6.7-6.9).

However, at 180 °C, a dense skin was found on the external surfaces of the embossed pattern. In fact, close examination of replicated porous patterns indicated an earlier initiation of this skin formation phenomenon even at a temperature below Tm of PLA. If comparing the surface appearances shown in Figs. 6.8-6.10, one can easily see a gradual decrease of the surface openness when the embossing temperature increased from 140 to 180 °C. When high permeability is a priori, the formation of a denser skin is undesired. On the other hand, the modification of the surface openness can render a change in permeability of the structure. One may therefore utilize this phenomenon for controlling the permeability of the resulting device [2].
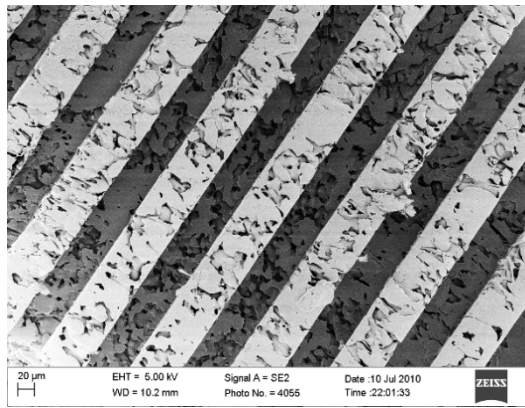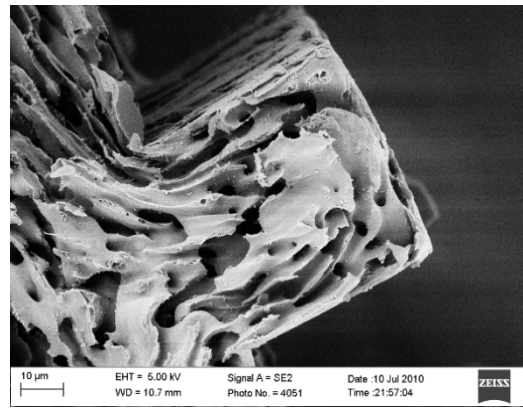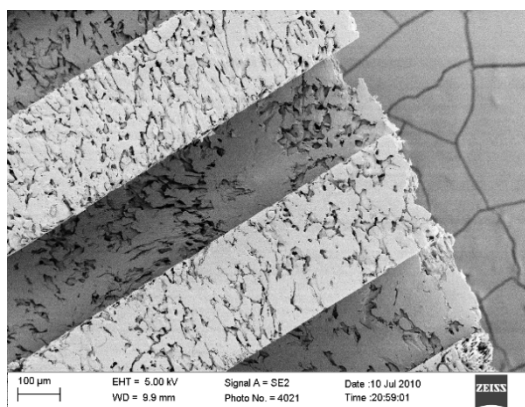
Figure 6.11: Samples prepared by annealing at 180 °C for 5 min followed by hot embossing at 120 °C and 20 N compression force, with stamps of different groove sizes: (a) 50 µm, top view; (b) 50 µm, cross-section; (c) 250 µm, top view, (d) 250 µm, cross-section.

6.4.3 Effects of annealing

For a co-continuous polymer blend, its internal structure tends to coarsen when the processing temperature is higher than the flow temperatures (Tm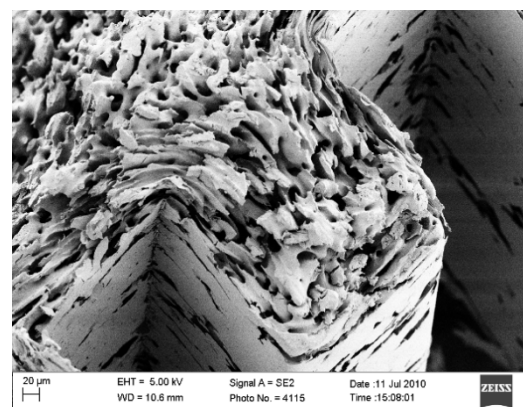 for PLA and the rubber plateau temperature for PS) of the involving components. Through quiescent annealing at different temperature and time, material structures with different phase sizes can be generated. In the current study, annealing and hot embossing were combined to create micropatterned porous structures with different pore sizes. Two procedures were tested for this fabricating concept and the influence of embossing-annealing sequence on the final sample structures was investigated. In the first procedure, annealing was conducted prior to embossing, while the second one reversed the sequence. These two fabricating procedures were referred to as AM and MA, respectively, for further reference.

The experimental results from the AM protocol are given in Fig. 6.11. These samples were first annealed inside an oven at 180 °C for 10 min. The annealed samples were cooled to room temperature to freeze the phase morphology before being reheated to 120 °C and embossed with 20 N compression force. In Fig. 6.11 (a & c), most of the surface pores were closed after hot embossing for samples with both 50 and 250 µm features. The cross-sections of these samples (Fig. 6.11 (b & d)) demonstrated an oriented structure especially around the corners. Such high level of orientation was not observed in the embossing experiments without the pre-annealing step. This can be seen by comparing with the structure in Fig. 6.7. It can also be seen
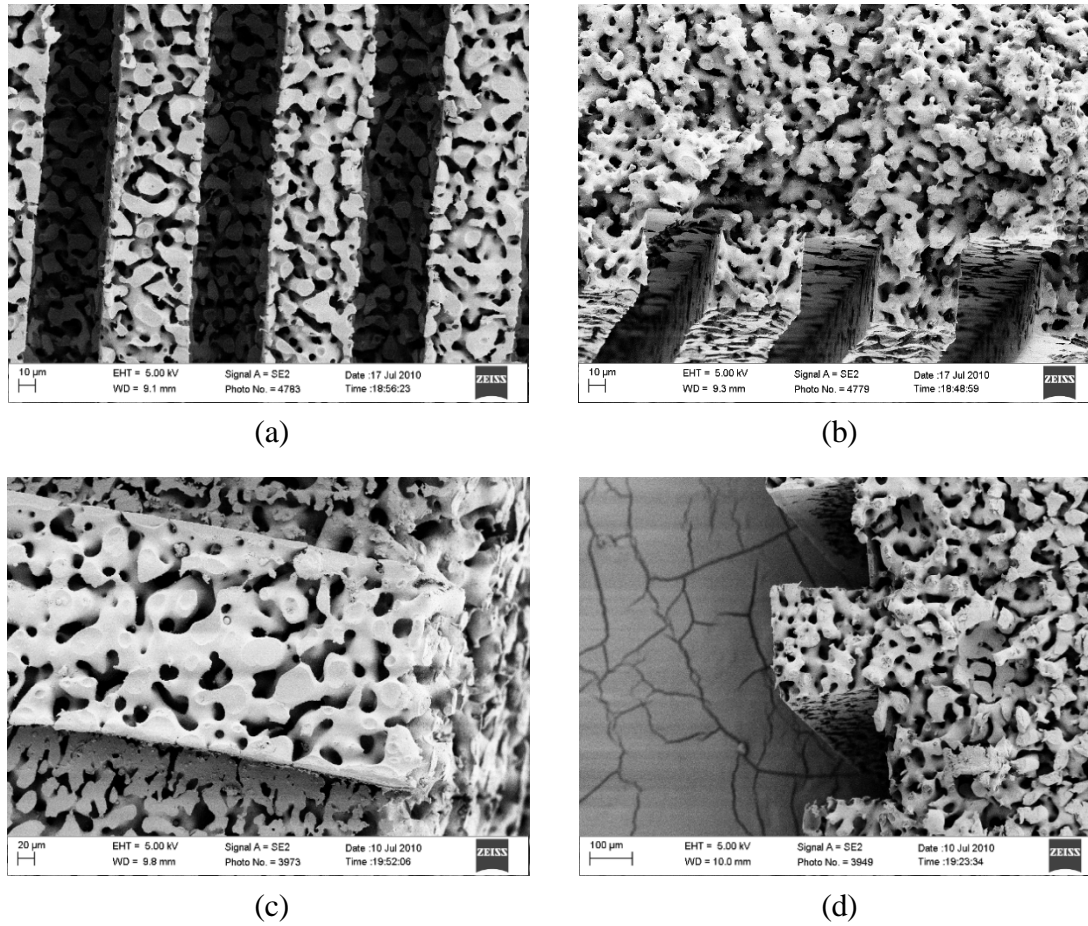
Figure 6.12: Samples embossed at 120 °C and 20 N compression force before annealed in oven at 180°C for different times: (a) 50 µm and 3 min, cross-section; (b) 50 µm and 3 min, top view; (c) 250 µm and 5 min, top view; (d) 250 µm and 5 min, cross-section.

that the pore size are very different in these two cases; with the annealing step, the pore size was increased by at least 5 times. From these contrasted observations, it may be reasonable to conjecture that the initial phase size play an important role in affecting the embossed structure; the large phase structure appeared to be more affected by the deformation. The reduced orientation at smaller pore sizes may be attributed to the increased elastic effects caused by the increased interfacial area.

The experimental results from the MA protocol are given in Fig. 6.12. The

annealing step was conducted after embossing, but the embossing step was performed under the same condition as in the AM protocol. Comparing with Fig. 6.11, one can see that the phase structures in Fig. 6.12 are much more uniform. Furthermore, open pore surfaces were obtained with this processing sequence. The difference may be explained as follows. As mentioned earlier, smaller pore size helps suppress orientations from deformation due to the increased elastic effect. Likewise, the annealing step facilitates additional elastic recovery/relaxation, thus further reducing the orientation. Therefore, the MA protocol is a better one for generating porous structures with a uniform morphology.

6.4.4 Controllable generation of graded porous structures

The MA method can be further developed for creating porous micropatterns with a graded porous structure. The coarsening rate during the annealing stage may be controlled spatially by varying the geometrical and/or boundary conditions applied on the blend. Two examples are given below to demonstrate this valuable modification.

In the first example, geometrical confinement was utilized to generate orientated structure. Fig. 6.13 shows a phase morphology highly modified by the geometrical conferment. Here, the side walls of microgroove on the stamp were used to impose a geometric confinement locally onto the blend microstructure. When the phase structure grew to a level comparable to the size of the microgroove, the existence of the groove walls could strongly impinge the structure evolution of the blend. Instead of growing equally in all directions, the structure tends to grow along the less obstructed

directions. As a result, the microstructure grew much faster along the groove direction, which caused the formation of an orientated morphology. Similar geometrical confinement effects were found previously by the authors during compression molding of a planar geometry [116].

(a)   (b)
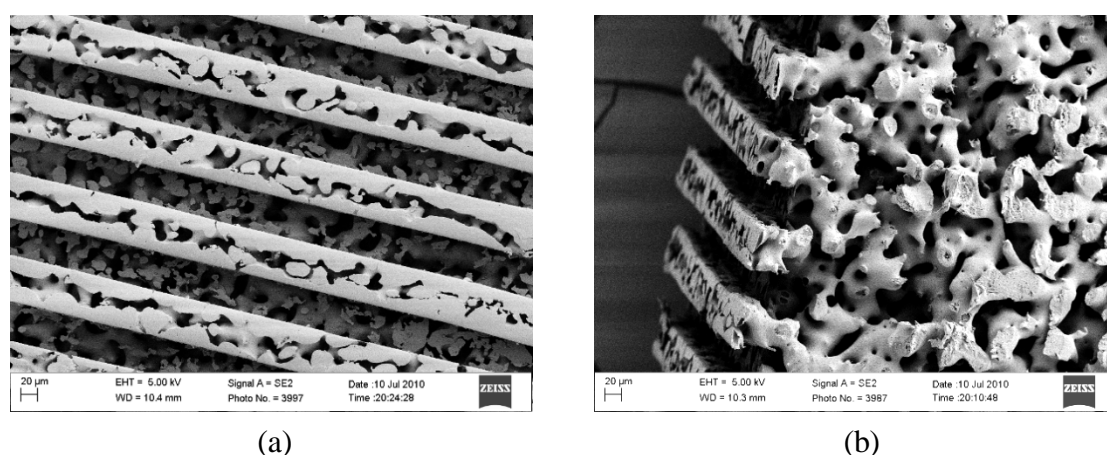
Figure 6.13: Surface aligned structure formed by embossing at 120 °C and 20 N compression force and consequentially annealing inside oven at 180°C for 10 min: (a) top view; (b) cross section. The groove size is 50 µm.

In the second example, a varied thermal boundary condition was applied to generate a gradient thermal field and consequently a gradient coarsening rate. This resulted in the generation of a gradient phase structure in the micropattern, as shown in Fig. 6.14. Instead of annealing in a uniform temperature field (as used for generating the morphology in Fig. 6.12), a temperature difference was imposed on the lower and upper plates during annealing (Fig. 6.14.a). With this setup, the material in contact with the silicon stamp had a higher temperature than the remaining. As a result, the phase size on the patterned side was much larger. The increased coarsening rate is caused by

the decreased viscosity at increased temperature; this mechanism is well understood [115].

Using the same principle, one can easily generate micropatterns with other types of

graded structures.

(a)

| 100 μm | EHT = 5.00 kV | Signal A = SE2 | Date :17 Jul 2010 | ZEISS |
| | WD = 10.1 mm | Photo No. = 4839 | Time :20:20:39 | |
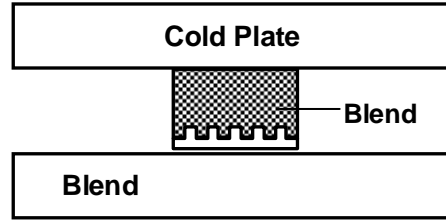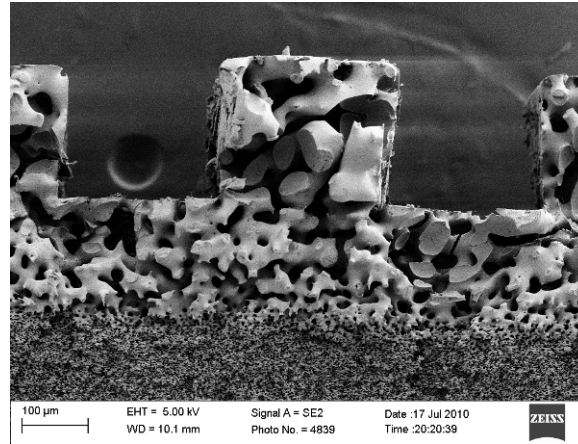
(b)

Figure 6.14: Micropatterned graded porous structure formed by embossing at 120 °C and 20 N compression force and consequentially annealing between two plates with upper plate at 20 °C and bottom plate at 200 °C: (a) annealing unit design; (b) SEM image of the micropatterned graded porous structure.

6.5   Conclusions

In this study, a new process for micropatterning of porous devices with a controllable morphology was developed and investigated. Specifically, a co-continuous polymer blend was hot embossed against a micropatterned mold and then annealed inside the mold to obtain the desired internal morphology. It was found that embossing at a low temperature below the polymer flow temperature led to a significantly deformed internal structure. This orientation effect was largely suppressed by hot embossing the blend above the flow temperature, especially when an in mold annealing stage was applied after embossing. In mold annealing was found to be a versatile technique for controlling the internal structure of the embossed pattern; not only the overall phase size but also its gradient and distribution can be controlled by varying the boundary conditions during in mold annealing. This in mold annealing process is superior to pre-embossing annealing, since the latter in combination with hot embossing led to the formation of a closed pore surface and undesired structural deformation.

6.6 References

1. Virgilio N, Sarazin P, Favis BD, Towards ultraporous poly(L-lactide) scaffolds from quaternary immiscible polymer blends, *Biomaterials*, 31, 5719-5728, 2010.

2. Xiang ZY, Sarazin P, Favis BD, Controlling Burst and Final Drug Release Times from Porous Polylactide Devices Derived from Co-continuous Polymer Blends, *Biomacromolecules*, 10, 2053–2066, 2009. Cao Y, Yin FP, Feng J, Rayatpisheh S, Chan V, Chan-Park MB, Regulating orientation and phenotype of primary vascular smooth muscle cells by biodegradable films patterned with arrays of microchannels and discontinuous microwalls, *Biomaterials*, 31, 6228-6238, 2010.

3. Sun CY, Liu SX, Liang DD, Shao KZ, Ren YH, and Su ZM, Highly stable crystalline catalysts based on a microporous metal-organic framework and polyoxometalates, *JACS*, 31, 5, 1883-1888, 2009.

4. Selvam P and Mohapatra SK, Synthesis, characterization and catalytic properties of mesoporous TiHMA molecular sieves: selective oxidation of cycloalkanes, *Microporous and mesoporous materials*, 7, 3, 137-149, 2004.

5. Girones M, Akbarsyah IJ, Nijdam, W, Van Rijn CJM, Jansen HV, Lammertink RGH, and Wessling M, Polymeric microsieves produced by phase separation micromolding, *J. Membrane Science*, 283, 411-424, 2006.

6. Bikel M, Culfaz PZ, Bolhuis-Versteeg LAM, Perez JG, Lammertink RGH, and Wessling M, Polymeric microsieves via phase separation microfabrication: process and design optimization, *J. Membrane Science*, 347, 93-100, 2010.

7. Papenburg BJ, Schuller-Ravoo S, Bolhuis-Versteeg LAM, Hartsuiker L, Grijpma DW, Feijen J, Wessling M, Stamatialis D, Designing porosity and topography of poly(1,3-trimethylene carbonate) scaffolds, *Acta Biometerialia*, 5, 3281-3294, 2009.

8. Lam MT, Clem WC, Takayama SC, Reversible on-demand cell alignment using reconfigurable microtopography, *Biomaterials*, 29, 1705-1712, 2008.

9. Isenberg BC, Tsuda Y, Williams C, Shimizu T, Yamato M, Okano T, Wong JY, A thermoresponsive, microtextured substrate for cell sheet engineering with defined structural organization, *Biomaterials*, 29, 2565-2572, 2008.

10. Yucel D, Kose GT, Hasirci V, Polyester based nerve guidance conduit design, *Biomaterials*, 31,1596-1603, 2010.

11. Berry CC, Campbell G, Spadiccino A, Robertson M, Curtis ASG, The influence of microscale topography on fibroblast attachment and motility, *Biomaterials*, 25, 5781-5788, 2004.

12. Sarkar S, Lee GY, Wong JY, Desai TA, Development and characterization of a porous micro-patterned scaffold for vascular tissue engineering applications, *Biomaterials*, 27, 4775-4782, 2006.

13. Jang HS, Cho MW, Park DS, Micro fluidic channel machining on fused silica glass using powder blasting, *Sensors*, 8, 700-710, 2008.

14. Song YA, Batista C, Sarpeshkar R, Han Jongyoon, Rapid fabrication of microfluidic polymer electrolyte membrane fuel cell in PDMS by surface

patterning of perfluorinated ion-exchange resin, *J. Power Sources*, 183, 674-677, 2008.

15. Mekaru H, Fukushima E, Hiyama Y, Takahashi M, Thermal roller imprint on surface of Teflon perfluoroalkoxy inlet tube, *J. Vac. Sci. Technol. B* 27(6), 2814-2819, 2009.

16. Choi HW, Bong S, Farson DF, Lu CM, Lee LJ, Femtosecond laser micromachining and application of hot embossing molds for microfluid device fabrication, J. *Laser Appl.,* 21, 196-204, 2009.

17. Pemg BY, Wu CW, Shen YK, Lin Y, Microfluidic chip fabrication using hot embossing and thermal bonding of COP, *Polym. Adv. Technol.*, 21, 457-466, 2010.

18. Kang MG, Guo LJ, Nanoimprinted Semitransparent Metal Electrodes and Their Application in Organic Light-Emitting Diodes, *Adv. Mater.,* 1391-1396, 2007.

19. Rao J, L. Keeney RW, Moth-eye-structured light-emitting diodes, *Optics Communications,* 283, 2446–2450, 2010.

20. Zhang Y, Lu J, Shimano S, Zhou H, Maeda R, Development of MEMS-based direct methanol fuel cell with high power density using nanoimprint technology, *Electrochemistry Communications*, 9, 1365-1368, 2007.

21. Lozano A, Barreras F, Valino L, Marin C, Imaging of gas flow through a porous medium from a fuel cell bipolar plate by laser-induced fluorescence, *Exp. Fluids*, 42, 301-310, 2007.

22. Zhang Y, Lu J, Zhou HS, Itoh T, Maeda R, Application of Nanoimprint Technology in MEMS-Based Micro Direct-Methanol Fuel Cell (μ-DMFC), *J. Miroelectromech. Syst.*, 17(4), 1020-1028, 2008.

23. Ishizuka M, Houjou H, Motokawa S, Mizuno J, Momma T, Osaka T, Shoji S, Metallization on Three Dimensions Microstructures Using Photoresist Spray Coating for Microdirect Methanol Fuel Cell, Jpn. *J. Appl. Phys*, 45(10A), 7944-7948, 2006.

24. Taylor AD, Lucas BD, Guo LJ, Thompson LT, Nanoimprinted electrodes for micro-fuel cell applications, *J. Power Sources*, 171, 218-223, 2007.

25. Kim HT, Reshentenko TV, Kweon HJ, Microstructured membranee assembly for direct methanol fuel cell, *J. Electrochem. Soc.*, 154, 10, B1034-B1040, 2007.

26. Vogelaar L, Barsema JN, Van Rijn CJM, Nijdam W, and Wessling M, Phase separation micromolding, *Adv. Mater*, 15, 16, 1385-1389, 2003.

27. Vogelaar L, Lammertink RGH, Barsema JN, Nijdam W, Bolhuis-Versteeg LAM, Van Rijn CJM, and Wessling M, Phase separation micromolding: a new generic approach for microstructuring various materials, *Small,* 1, 6, 645-655, 2005.

28. Hull CW, Apparatus for Production of Three-Dimensional Objects by Stereolithography, U.S. Patent 4,575,330, 1984.

29. Zhou JG and He ZY, Rapid pattern based powder sintering technique and related shrinkage control, *Journal of Materials and Design*, 19, 241-248, 1998.

30. Morelli S, Salerno S, Piscioneri A, Papenburg BJ, Di Vito A, Giusi G, Canonaco M, Stamatialis D, Drioli E, and De Bartolo L, Influence of micro-patterned PLLA

membranes on outgrowth and orientation of hippocampal neurites, *Biomaterials,* 31, 27, 7000-7011, 2010.

31. Wu GZ, Xu HB, Zhou T, Morphology evolution, crystalline orientation, and thermal expansion of PA6/SEBS blends with nanolayer networks, *Polymer*, 51, 3560-3567, 2010.

32. Yu W, Zhou W, Zhou CX, Linear viscoelasticity of polymer blends with co-continuous morphology, *Polymer*, 51, 2091-2098, 2010.

33. Pyun A, Bell JR, Won KH, Weon BM, Seol SK, Je JH, Macosko CW, Synchrotron X-ray Microtomography for 3D Imaging of Polymer Blends, *Macromolecules*, 40, 2029-2035, 2007.

34. Galloway JA, Koester KJ, Paasch BJ, Macosko CW, Effect of sample size on solvent extraction for detecting cocontinuity in polymer blends, *Polymer*, 45, 423-428, 2004.

35. Zhang W, Yao DG, Zhang QW, Zhou JG, Leikes PI, Fabrication of interconnected microporous biomaterials with high hydroxyapatite nanoparticle loading, *Biofabrication*, 2, 035006, 2010.

36. Steinmann S, Gronski W, Friedrich C, Quantitative rheological evaluation of phase inversion in two-phase polymer blends with cocontinuous morphology, *Rheologica acta*, 41, 77 -86, 2002.

37. Lopez-Barron CR, Macosko CW, Characterizing Interface Shape Evolution in Immiscible Polymer Blends via 3D Image Analysis, *Langmuir*, 25(16), 9392-9404, 2009.

38. Li JM, Ma PL, Favis BD, The Role of the Blend Interface Type on Morphology in Cocontinuous Polymer Blends, Macromolecules, 35, 2005-2016, 2002.

39. Yuan ZH, Favis BD, Influence of the Efficacy of Interfacial Modification on the Coarsening of Cocontinuous PS/HDPE Blends During Quiescent Annealing, *J. Polym. Sci. Part B: Polym Phys*, 44, 711-721, 2006.

40. Yao DG, Zhang W, Zhou JG, Controllable Growth of Gradient Porous Structures, *Biomacromolecules*, 10, 1282–1286, 2009.

41. Zhang W, Deodhar S, and Yao DG, Geometrical confining effects in compression molding of co-continuous polymer blends, *Annals of Biomedical Engineering*, 38(6), 1954–1964, 2010.

42. Heckele M and Schomburg WK, Review on micro molding of thermoplastic polymers, *J. Micromechanics Microengineering*, 14, R1-R14, 2004.

43. Becker H and Gartner C, Polymer microfabrication methods for microfluidic analytical applications *Electrophoresis*, 21, 12-26, 2000.

44. Potschke P and Paul DR, Formation of co-continuous structures in melt-mixed immiscible polymer blends *J. Macromol. Sci., Polym. Rev.* C, 43, 87–141, 2003.

CHAPTER 7

NUMERICAL SIMULATION ON PHASE COARSENING

PROCESS OF CO-CONTINUOUS POLYMER BLEND

7.1   Introduction

In co-continuous polymer blends, the competition between interfacial tension and viscous resistance gives rise to the intriguing phase coarsening behavior. Experimentally, researchers yet notice a simple linear relation between annealing time and pore size increase. As one might expect, the coefficient for this relation is a combination of the interfacial tension coefficient γ and the blend zero-shear viscosity η. For numerous co-continuous polymer blends, γ/η was surprisingly found to be sufficient in characterizing the coarsening process where the average pore diameter could change from several to hundreds of micrometers. Moreover, this relation was found to be effective for a large range of concentration as long as the blend could keep its co-continuous phase morphology. Because of the availability of relation like this, researchers can predict the needed annealing time to get a desired pore size by comparing the pore sizes of samples annealed for different periods of time. However, the complex dependency of zero-shear viscosity and interfacial tension on the system temperature makes the information for one temperature cannot be easily applied to other annealing conditions. Consequently, for isothermal annealing process, coarsening rate has to be measured for each individual annealing temperature. For non-isothermal

annealing where temperature gradient exists, this direct point-by-point measuring method can be very hard to implement. The resulted insufficiency on information about spatial distribution of the phase coarsening rate can strongly limit the application of co-continuous polymer blend in situations where complex gradient porous material is required. This limitation becomes even more severe when precise control over pore size distribution is an essential design criterion for a device to have the required functions.

To overcome this technical difficulty and facilitate the fabrication of porous devices with complex pore size distribution, rheological characterization, scanning electron microscopy, and numerical simulation were combined together for better prediction of the final pore size distribution. The final pore size, as mentioned previously, is directly linked to the initial phase size and the local coarsening rate. Among these two controlling parameters, the initial phase size is determined by the mixing conditions and material properties of both components inside the blend. Actually, the mixing conditions and the material properties are not completely independent when formation of co-continuous phase morphology is required. To form the initial co-continuous phase morphology, the mixing conditions have to be chosen to make the two components have a viscosity ratio proportion to their concentration ratio. Because of this requirement, the control over the initial phase size of a blend with a fixed concentration ratio is limited. This makes quiescent annealing the critical step for the pore size control which is the object of this study.

Despite the simplicity in the phenomenological expression for coarsening rate,

kinetics of co-continuous polymer blend phase coarsening is very complex. In current study, a big portion of these details, such as phase agglomeration/breakage, viscoelasticity, and interfacial slippage, were not considered explicitly and instead the phase coarsening was treated purely as a free energy driven phase separation process. The only kinetic factor being included in the modeling is the viscous flow of both components which have equal viscosity at any temperatures. As the modeling was designed to study non-isothermal annealing phenomena, the temperature dependence of zero-shear viscosity was introduced into the simulation by using WLF model.

7.2   Simulation Procedures

7.2.1 Generation of initial phase morphology

In current study, the possibility of utilizing phase morphology obtained from different sources for numerical modeling was explored. To be more specific, both numerical simulation plot and SEM (Scanning Electron Microscopy) observation were targeted as the candidates for generating the initial phase morphologies. Starting from a simulation generated plot, one can track the influence of each individual variable on the kinetics of the overall phase evolution from the beginning. On the other hand, using SEM image as the initial phase morphology, one can have a more realistic model and the opportunity to verify the quality of the constructed model in representing the real experimental results. However, one should keep in mind that the concentration ratio is accurate only for the whole material. The area ratio calculated from a single cross-section may not exactly equal the concentration ratio.

For numerical simulation plot method, the initial phase morphology was generated through modeling the spinodal decomposition of a binary polymer mixture. The starting state for this simulation was a homogeneous fluid. In this fluid, the viscosities of both components were ignored. Also, entropy, which is important for long chain polymer system, was not included. The error caused by leaving out the entropy effect, however, was considered negligible as the characteristic length scale in this simulation was tens of micrometers which were much larger than the intrinsic length scale of a polymer chain. Morphology evolution at this length scale was unlikely to show any confinement effect which could lead to variation on the entropy

part of the system free energy. The only driven force for the phase separation was the interfacial tension which was calculated as the difference between the surface tensions of the two polymer components. The calculated interfacial tension was embedded into Cohn-Hilliard equations which were used to describe the phase separation kinetics of the binary polymer blend. As soon as the two components formed distinguishable phase domains, the simulation was stopped to reserve the phase morphology for later simulation.

Compared with the simulation plot method, generating the initial phase morphology using SEM image was much more straightforward. For a particular concentration, a small piece of the as-mixed blend was collected and one component was then selectively extracted. The weight change of the sample was measured to monitor the progress of the extracting process. After the sacrificial component was completely removed, the resulted porous sample was observed with SEM. The SEM image was recorded and saved for further simulation.

7.2.2 Digital image analysis

The main goal for digital image analysis is to transfer images from various sources into information which can be used to define phase domains in a CFD (Computational Fluid Dynamics) model. According to the style of the images, one can differentiate them as colored image or gray scale plot. For colored image adopted by most simulation software and optical microscope, the intensities of the RGB (Red, Green, and Blue) elements are combined to represent component A, component B, and the

interface between A and B. In the case of grey scale plot generated by SEM, only one intensity variable is involved. In order for these images to be recognizable for CFD simulation, one has to change these intensity variables into B&W (Black and White) to define domain A and domain B.
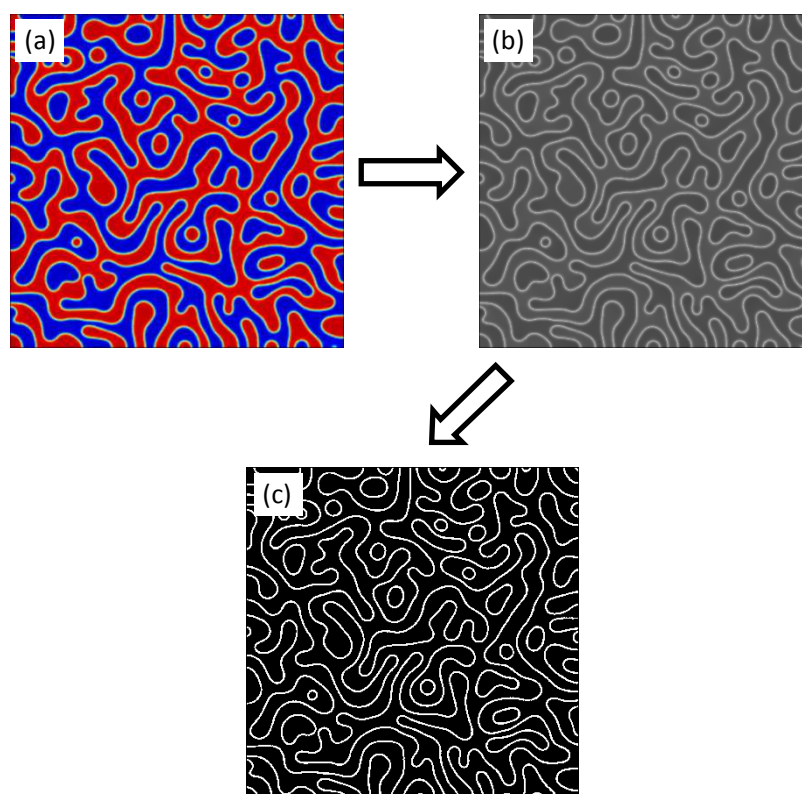

Figure. 7.1: Image analysis of simulation generated result: (a) co-continuous phase morphology in a binary polymer blend; (b) gray scale image; (c) interface between component A and B.

For colored image, it was first changed to gray scale plot where the interfaces were locations where the intensity had a high value, shown in Fig.7.1 (b). The produced grey scale image was transferred into B&W format using proper threshold

parameter. The criterion for proper threshold parameter was to recover the interface as faithfully as possible refer to the interface on the initial image. For gray scale image collected from SEM, it was directly transferred into B&W plot, Fig.7.2. In these B&W images, the intensity variable could only have two values, one or zero. A binary plot like this could be imported into CFD software to study the phase coarsening phenomenon of co-continuous polymer blend.
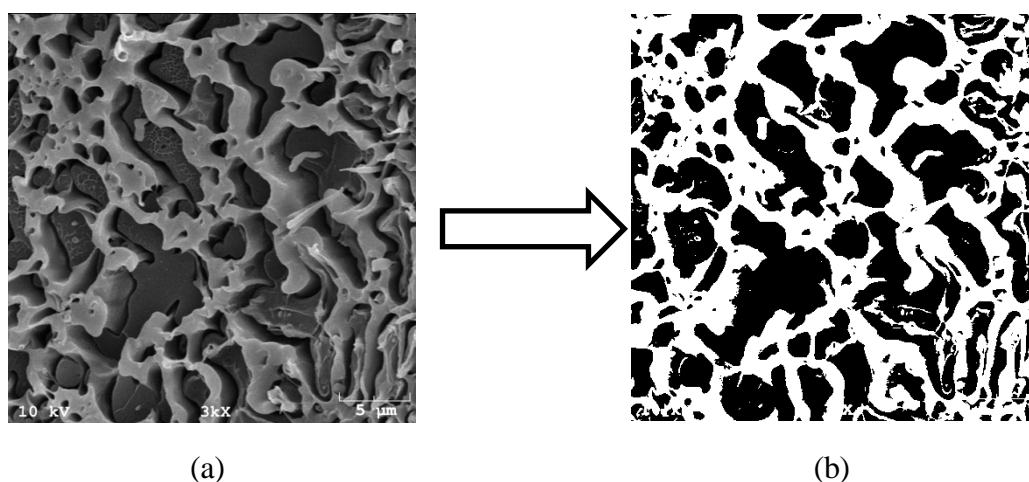

(a)   (b)

Figure. 7.2: Image analysis of SEM: (a) co-continuous phase morphology in a binary polymer blend; (b) B&W (Black and White) plot of the SEM image.

7.2.3 Isothermal annealing

Through years, many different techniques are developed to understand the phase morphology and coarsening kinetics of co-continuous polymer blend. Because of the high achievable resolution and the simplicity in sample preparation, SEM is widely

used in study of co-continuous polymer blend. However, each of these "in-plane" SEM images can only provide partial information regarding the complex 3D phase structure of a co-continuous polymer blend. To obtain the complete structural information of this type of material, one needs to do SEM observation of many cross-sections. This practice is extremely time-consuming and tends to overload researchers with structural details which may not contribute to the understanding of a blend. To be more specific, the total interfacial area and its reduction rate are the two important variables for the current study in understanding the kinetics of isothermal annealing. In comparison with these two parameters, the information about the whole process of structure evolution becomes less necessary. For this reason, the author explored the possibility of utilizing numerical simulation to link the 2D information (e.g. interfacial length measured from SEM) with 3D variables like these mentioned above. With this knowledge, one only needs to conduct limited number of 2D SEM observations to understand the relevant 3D objects.

In order to utilize numerical simulation to study the quiescent isothermal annealing process, there are two issues one needs to resolve in advance. First, one needs to obtain information about material properties which dominate the kinetics of the annealing process. Secondly, a proper theoretical modeling strategy needs to be laid out to describe the co-continuous polymer blend system and its phase coarsening process. In the case of quiescent isothermal annealing, the dominating parameters are zero shear viscosity of both components and interfacial tension between them. If the system can be assumed at its steady state, the temperature dependency of these

material properties will have no influence on the isothermal annealing process. They, for this reason, can be individually measured and applied for numerical simulation. In current study, the zero shear viscosities of the two components were set to be identical. Besides, both components were treated as Newtonian fluid, which should be a valid approximation considering the small strain rate encountered in the coarsening process. Unlike zero shear viscosity, the interfacial tension between two polymers was not so easy to be collected. The main difficulty here was the long relaxation time resulted from the high zero shear viscosity. For polymer blend, this means the required thermodynamic equilibrium for interfacial tension measurement cannot be reached in a reasonable period of time. In the meantime, holding polymer at high temperature can render to thermal degradation and influence the interfacial tension measure. However, since the goal of this study is to build up the relation between 2D experimental observation and 3D interfacial area, one does not need precise value of the interfacial tension to achieve this goal. With this in mind, the author adopted the difference between the surface tensions of the two components as an approximated interfacial tension in forming the relation between the 2D observation and 3D system properties. These essential material variables will then be applied in the next step of numerical modeling.

In modeling a two-phase co-continuous polymer blend, Navier-Stokes equation, mass conservation equation, and equations for tracking the interface between the two polymer components were combined to describe the coarsening process. The polymer blend was treated as an incompressible fluid since no pressure was purposely

added in isothermal annealing process and under normal atmosphere pressure the compressibility of common polymers could be safely ignored. The incompressible formulation of the Navier-Stokes equations was designed to describe the ongoing interfacial tension driven phase coarsening phenomenon inside the polymer blend where the two components could have different viscosity. To simplify the model, only interfacial

$$\rho \frac{\partial u}{\partial t} + \rho(u \cdot \nabla)u = \nabla \cdot [-PI + \mu(\nabla u + \nabla u^T)] + F_{st} \tag{7.1}$$

$$\nabla \cdot u = 0 \tag{7.2}$$

tension and viscous stress were considered, Eq. 7.1 and 7.2. In Eq. 7.1, the ρ and μ were equivalent density and equivalent viscosity. Both of them are variables of position. P and F_{st} are system pressure and interfacial tension respectively. It is clear that the interfacial tension term F_{st} competes with the second term on the right side of Eq. 7.1in determining the velocity field u. However, the information about u is not sufficient to determine the phase behavior for a two-phase system. One needs a tool to track the interface evolution corresponding to the changes in the velocity field.

There are two common techniques which can be employed to track the interface movement in a two-phase mixture. [14-16] The first technique is called level set method which utilizes a smooth step function ϕ to describe the density distribution of the two components. The ϕ function changes smoothly from 1 for component A to 0

for component B. The isocontour surface (3D)/line (2D) of $\phi = 0.5$ defines the interface between A and B. The influence of velocity field u on the level set function ϕ can be expressed using Eq. 7.3. [14, 16]

$$\frac{\partial \phi}{\partial t} + u \cdot \nabla \phi = \gamma \nabla \cdot (\varepsilon \nabla \phi - \phi(1-\phi)\frac{\nabla \phi}{|\nabla \phi|}) \tag{7.3}$$

In this equation, terms on the left-hand side give the motion of a local interface according to a particular velocity field; terms on the right-hand side are set up to ensure a proper numerical stability. The role of parameter γ is to secure the stability of the level set function and the correct movement of the interface. In order to get reasonable simulation results, tuning of γ is required on a case-to-case basis. Another parameter in this method, ε, is used to define the thickness of the interfacial region. A larger ε value means a thicker interface and a smoother change of the step function ϕ from one phase region to another. According to the formulation of this method, the equivalent density ρ and the equivalent zero-shear viscosity μ can be defined as in Eq. 7.4 and 7.5. [14, 16]

$$\rho = \rho_1 + (\rho_2 - \rho_1)\phi \tag{7.4}$$

$$\mu = \mu_1 + (\mu_2 - \mu_1)\phi \tag{7.5}$$

The level set expression of the interfacial tension F_{st} is presented in Eq. 7.6 [14, 16]

$$F_{st} = \sigma\kappa\delta n = \nabla \cdot \left(\sigma\left(I - \left(nn^T\right)\right)\delta\right) \tag{7.6}$$

In this equation, σ is the interfacial tension coefficient, n is the unit vector normal to the interface, κ is the curvature, and δ is a Dirac delta function with its center locates at the interface. The formulations of n and κ are summarized in Eq.7.7 and 7.8. [14, 16]

$$n = \frac{\nabla\phi}{\|\nabla\phi\|}\Big|_{\phi=0.5} \tag{7.7}$$

$$\kappa = -\nabla \cdot n\big|_{\phi=0.5} \tag{7.8}$$

The δ function in Eq.7.6 was approximated by a smooth function in Eq. 7.9 to facilitate the numerical simulation. [14, 16]

$$\delta = 6\|\nabla\phi\|\|\phi(1-\phi)\| \tag{7.9}$$

At the beginning of the simulation, the velocity field variable u at the left-hand side of Eq.7.3 was set to zero to mimic the initial state of a quiescent isothermal annealing in which no net movement in either component other than a random thermal vibration, Eq. 7.10. [14, 16]

$$\frac{\partial \phi}{\partial t} = \gamma \nabla \cdot (\varepsilon \nabla \phi - \phi(1-\phi)\frac{\nabla \phi}{|\nabla \phi|}) \qquad (7.10)$$

As mentioned previously, there are two methods can be used to track the interface motion in a co-continuous polymer blend. The other method is called the phase field method in which Cahn-Hilliard equation is used to describe the interface movement. [15, 16] Different from the aforementioned level set method, phase field method not only moves the interface based on the value of local velocity field but also conducts system free energy minimization which incorporates phase field method with more physical meanings. For this reason, the author employed this method in current simulation of isothermal annealing process.

The two main differences between the phase field method and the level set method are the introduction of free energy function and the expression of interfacial tension. The system free energy is defined as a function of dimensionless phase field parameter ϕ, its gradient $\nabla \phi$, and system T, Eq. 7.11. [15, 16]

$$F(\phi, \nabla \phi, T) = \int (\frac{1}{2}\varepsilon^2 |\nabla \phi|^2 + f(\phi, T)) dV = \int f_{tot} dV \qquad (7.11)$$

The parameter ε, as in level set method, is a measure of the interfacial thickness. The evolution of the phase field parameter follows the kinetics represented by Eq. 7.12 [15, 16]

$$\frac{\partial \phi}{\partial t} + (u \cdot \nabla)\phi = \nabla \cdot \gamma (\frac{\partial f_{tot}}{\partial \phi} - \nabla \cdot \frac{\partial f_{tot}}{\partial \nabla \phi}) \qquad (7.12)$$

The terms inside the parenthesis at right-hand of Eq. 7.12 is the derivative of the system free energy with regard to dimensionless phase field variable φ and its gradient $\nabla\varphi$. The definition of phase field variable φ guarantees the volume fractions of the two components are $(1+\varphi)/2$ and $(1-\varphi)/2$. It is the right side of Eq.7.12 strives to guide the system towards its minimum free energy state. The mobility parameter γ defines the characteristic relaxation time for the energy minimization process.

To make the free energy expression more suitable for our two-phase polymer blend system, Ginzburg-Landau free energy equation was adopted to describe the total mixing energy density. For isothermal annealing process, the G-L equation is: [15, 16]

$$f_{mix}(\phi, \nabla\phi) = \frac{1}{2}\lambda|\nabla\phi|^2 + \frac{\lambda}{4\varepsilon^2}(\phi^2 - 1)^2 \qquad (7.13)$$

where λ is the mixing energy density and ε is the capillary width that defines the thickness of the interface. These two parameters are linked with interfacial tension coefficient σ through: [15, 16]

$$\sigma = \frac{2\sqrt{2}\lambda}{3\varepsilon} \qquad (7.14)$$

The combination of Eq. 7.12 and 7.13 leads to the Cahn-Hilliard equation: [15, 16]

$$\frac{\partial \phi}{\partial t} + u \cdot \nabla \phi = \nabla \cdot \gamma \nabla G \qquad (7.15)$$

where the u is the velocity field, γ is the mobility parameter which controls the characteristic time scale of the Cahn-Hilliard diffusion and links with the interface thickness, and G is the chemical potential and is defined as: [15, 16]

$$G = \lambda[-\nabla^2 \phi + \frac{\phi(\phi^2 - 1)}{\varepsilon^2}] \qquad (7.16)$$

From Eq. 7.15 and 7.16, it is not difficult to find out that Cahn-Hilliard equation is a fourth-order PDE (partial differential equation). This equation needs to be decoupled into two second-order PDEs to perform the numerical simulation. The decoupling procedure was based on the observation that the phase field variable φ stays at a value of 1 or -1 in either component and has values between 1 and -1 only in the very thin interfacial region. From this observation, the original fourth-order PDE was split into two second-order PDEs: [15, 16]

$$\frac{\partial \phi}{\partial t} + u \cdot \nabla \phi = \nabla \cdot \frac{\gamma \lambda}{\varepsilon^2} \nabla \Psi \qquad (7.17)$$

$$\Psi = -\nabla \cdot \varepsilon^2 \nabla \phi + \phi(\phi^2 - 1) \qquad (7.18)$$

Similar to the level set method, at the beginning of the simulation, the velocity

field variable u at the left-hand side of Eq.7.15 was set to zero to mimic the initial state of a quiescent isothermal annealing in which no net movement in either component other than a random thermal vibration, Eq. 7.19. [15, 16]

$$\frac{\partial \phi}{\partial t} = \nabla \cdot \frac{\gamma\lambda}{\varepsilon^2}\nabla\psi \qquad (7.19)$$

Correspond to the above definition, the expression for chemical potential and interfacial tension are: [15, 16]

$$G = \frac{\lambda\Psi}{\varepsilon^2} \qquad (7.20)$$

$$F = G\nabla\phi \qquad (7.21)$$

To be incorporated with Navier-Stokes equation for solving a two-phase flow problem, several key variables need to be defined in consistence with the phase field method. The first one is the volume fraction of fluid 2: [15, 16]

$$V_f = \min(\max([(1+\phi)/2],0),1) \qquad (7.22)$$

From this definition, the density and viscosity of the blend can be calculated with mixture rule: [15, 16]

$$\rho = \rho_1 + (\rho_2 - \rho_1)V_f \tag{7.23}$$

$$\mu = \mu_1 + (\mu_2 - \mu_1)V_f \tag{7.24}$$

where ρ_1, ρ_2, μ_1, and μ_2 are the density and zero-shear viscosity of fluid 1 and fluid 2 respectively.

The mean curvature of the interface between the two fluids can be calculated as: [15, 16]

$$\kappa = 2(1+\phi)(1-\phi)\frac{G}{\sigma} \tag{7.25}$$

The initial phase morphology of a 50/50% (concentration ratio) co-continuous polymer blend undergoing isothermal annealing process is presented in Fig.7.3. In this image, the red, blue, and green regions are polymer A, polymer B, and A-B interface respectively.
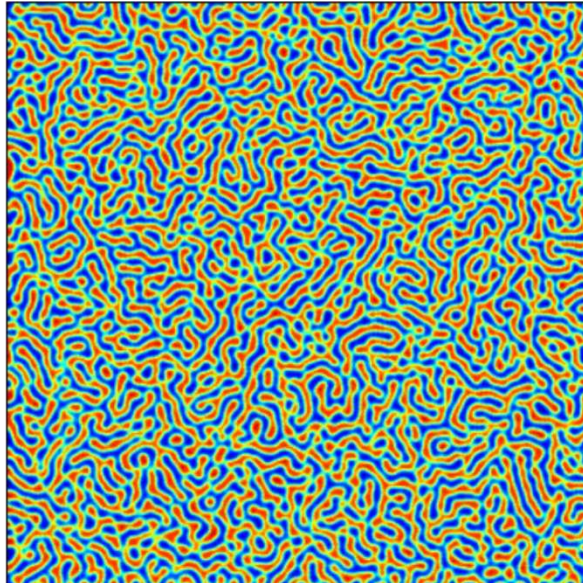
Figure 7.3: Initial phase morphology of a 50/50% (concentration ratio) co-continuous polymer blend undergoes isothermal annealing process. The red, blue, and green regions are polymer A, polymer B, and A-B interface respectively.

(a)

(b)

(c)   (d)
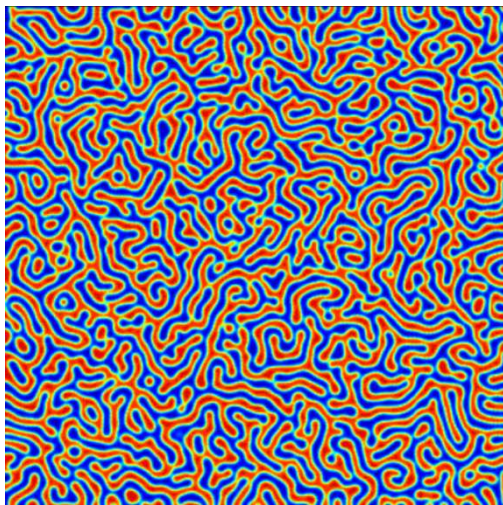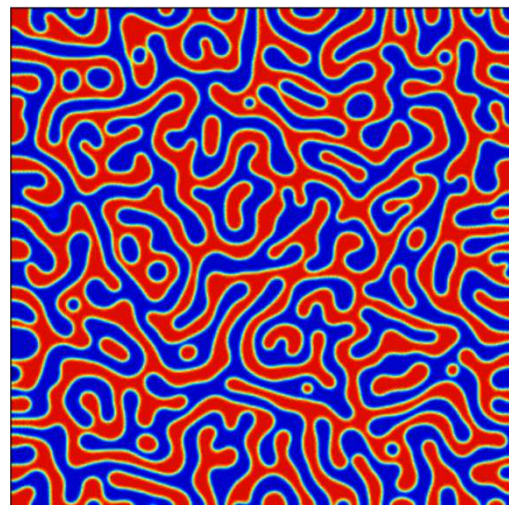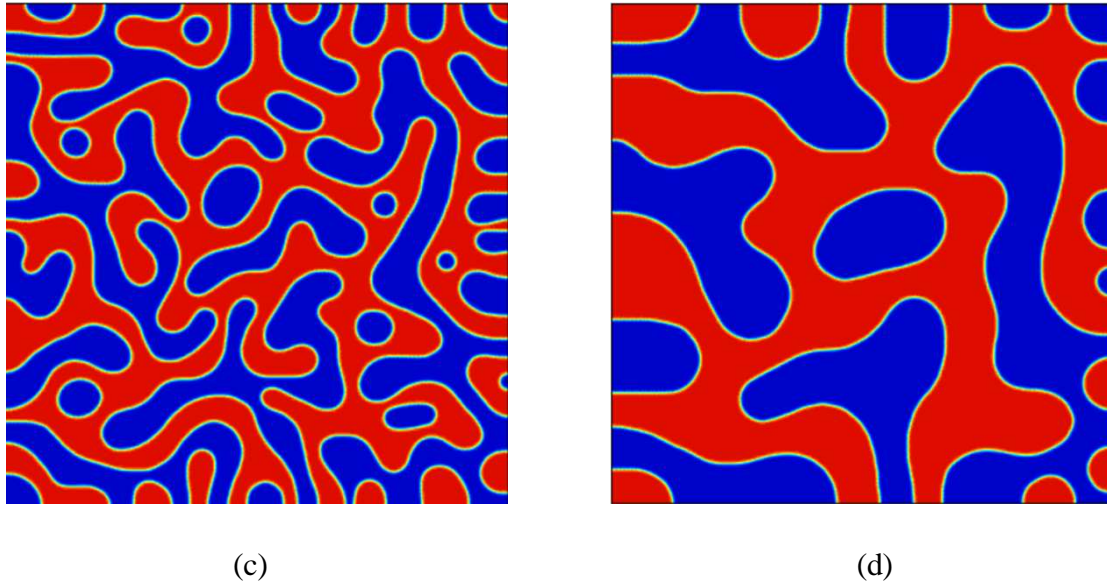
Figure 7.4: Phase morphologies of a 2D co-continuous polymer blend undergoing isothermal annealing for different times. The red region is polymer A and the blend region is polymer B. The total image size is 0.5 mm * 0.5 mm. The individual annealing times are: (a) 0.5; (b) 4; (c) 30; (d) 250 seconds.

Starting from the initial phase morphology in Fig. 7.3, a 2D simulation mimicking the isothermal annealing process of a co-continuous polymer blend was performed. Representative morphologies were shown in Fig. 7.4, while more comprehensive simulation results were supplied in appendix as Fig. A.1.

Although the phase evolution phenomenon presented in Fig. 7.4 and Fig. A.1 qualitatively matches the reported experimental observations, the reliability of the 2D simulation for an intrinsically 3D process should be verified. According to experimental results from other researchers, there is a simple relation between 2D and 3D coarsening rates for a co-continuous polymer blend. If a similar relation could be obtained between 2D and 3D simulation, the computational cost could be greatly reduced. To verify the existence of the aforementioned relation, the 2D and 3D

coarsening rates were calculated through simulation on a simplified 3D model. The relation between the geometry of the simplified 3D model and that of a co-continuous structure is shown in Fig. 7.5. When one focuses on the local geometry of a co-continuous structure (top two in Fig.7.5), the "real" geometry may be approximated as an ellipsoid presented with white line. The coarsening process can then be mapped to the rounding process of an elongated ellipsoid. This rounding process can be easily simulated for ellipsoid and its 2D counterpart, ellipse. The simulation results were summarized in Fig. 7.6 and Fig. 7.7. In order to compare the structural evolution kinetics of the 3D and 2D systems, two characteristic lengths were defined for them accordingly. For a 2D system, the characteristic length was expressed as the averaged interfacial length per unit area. Correspondingly, for a 3D system, the characteristic length was defined as the averaged interfacial area per unit volume. The ratio between the two characteristic lengths at their initial states (time=0) was used to adjust the 2D simulation result to its 3D counterpart.
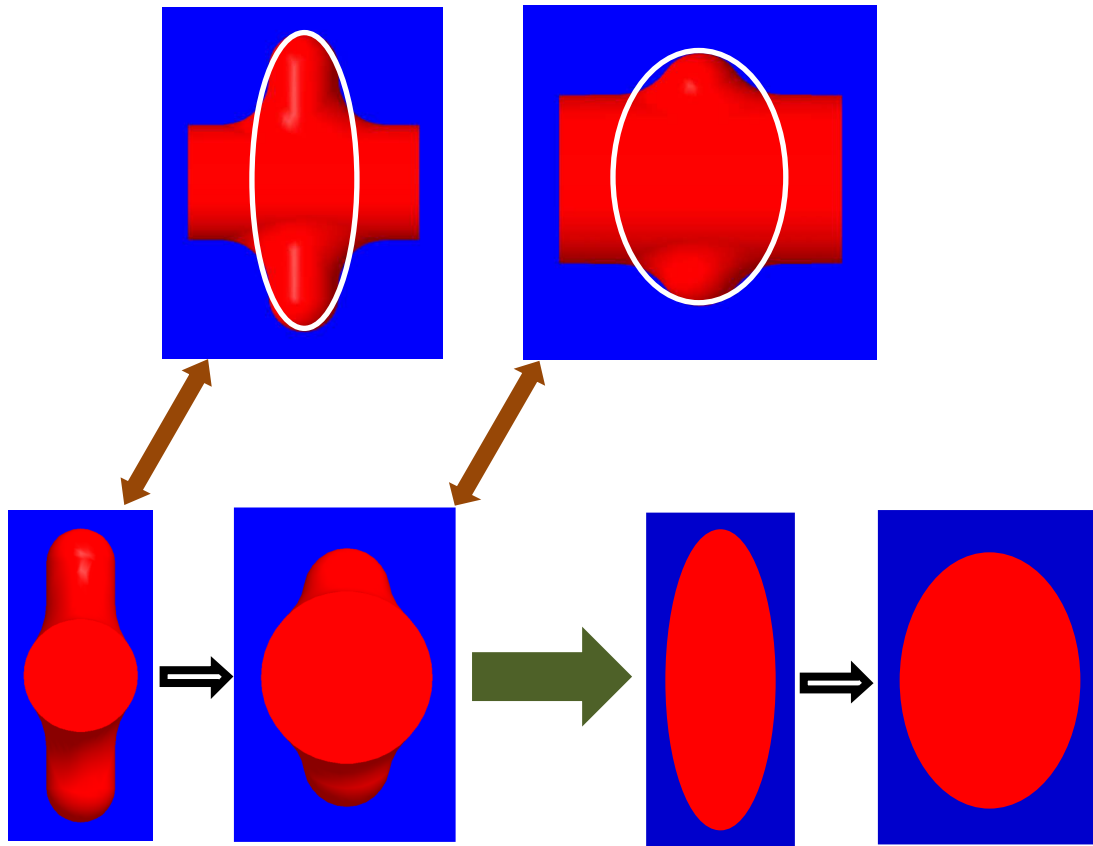
Figure. 7.5: Similarity between a coarsening co-continuous structure and a rounding ellipsoid.
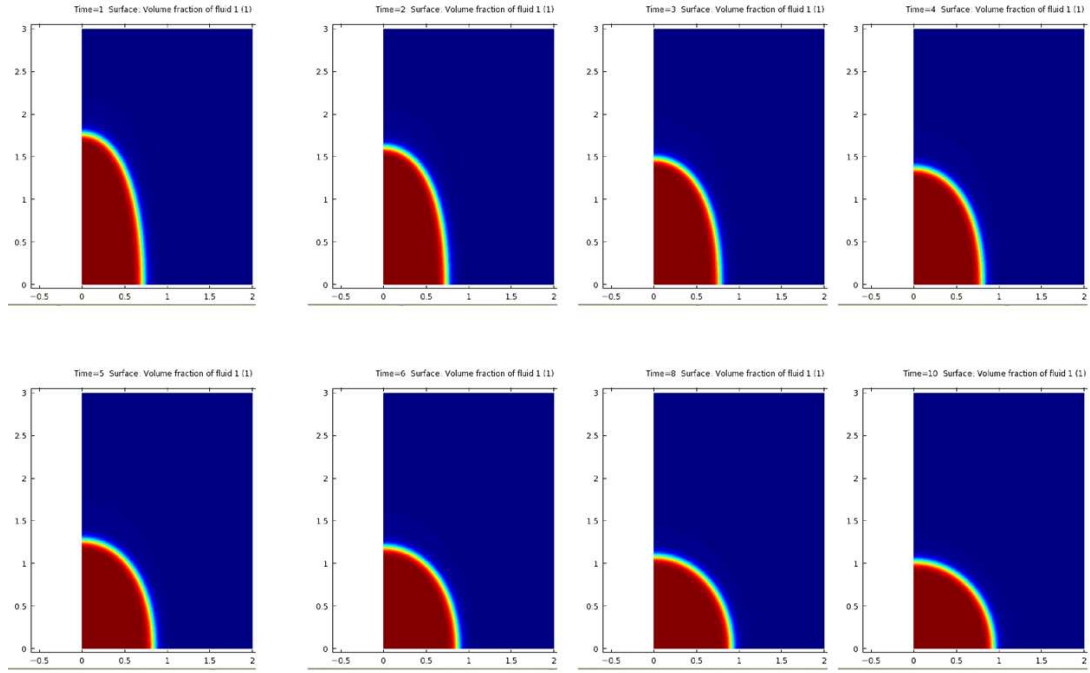
Figure 7.6: Simulated rounding process of an ellipsoid at different times. Top, from lift to right: 1, 2, 3, 4 seconds; bottom, from lift to right: 5, 6, 8, 10 seconds.
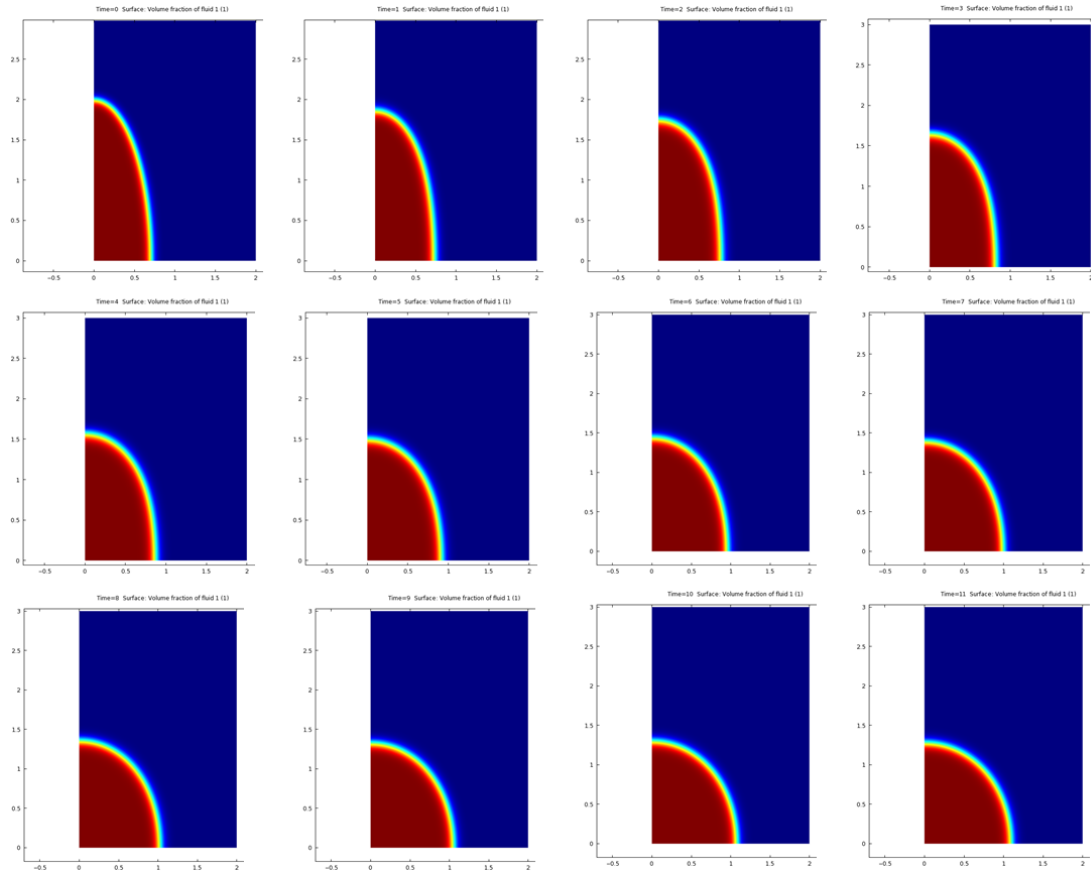
Figure 7.7: Simulated rounding process of an ellipse at different times. Top, from lift to right: 0, 1, 2, 3 seconds; middle, from lift to right: 4, 5, 6, 7 seconds; bottom, from lift to right: 8, 9, 10, 11 seconds.
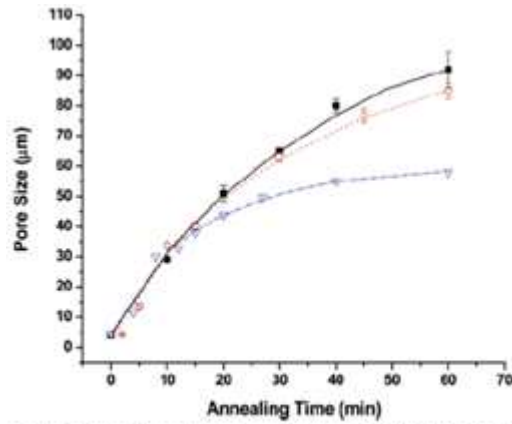
Figure 8. Plot of pore size vs annealing time of 50/50 PS/PE blends as measured with SEM[25] (▽), X-ray microtomography (○), and mercury porosimetry (■). Lines are to guide the eye and error bars are shown.
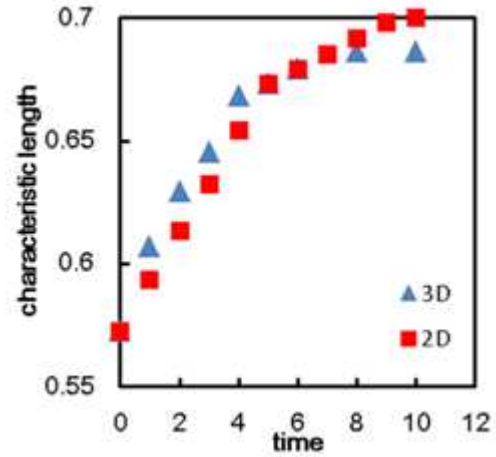
(a)   (b)

Figure 7.8: Evolution of phase characteristic length: (a) experimental results; (b) simulation results. (Reused by permission from the publisher of Pyun, 2007)

The simulated coarsening rates of these two systems were summarized in Fig. 7.8 (b). The results from simulation were then compared with experimental results reported in literature, shown in Fig. 7.8 (a). [9] The similarity among simulated curves and the experimental curves could be observed. The initial steep linear region and the later stage plateau in the experimental curves were predicted by the simulation. After the effectiveness of 2D simulation was verified, a 2D CAE strategy for controllable growth of gradient porous structures was proposed in the next step.

7.2.4 Generation of gradient porous structures

As stated in chapter 3, by applying a properly designed thermal boundary, a well defined temperature field could be generated inside a material. This temperature field later led to the formation of a gradient porous structure through an annealing process. In order to have a better understanding about the relation between applied thermal boundary and final gradient porous structure, a numerical modeling effort was presented here to provide a framework for designing a gradient porous structure from basic material properties. The three required material properties are interfacial tension coefficient, zero-shear viscosity of fluid 1, and zero-shear viscosity of fluid 2. In this study, the difference between the surface tension coefficients of the two components was employed as the interfacial tension coefficient for the binary blend system. The zero-shear viscosities of the two components were set to be equal. In addition, both materials were treated as Newtonian liquid.

After having the required material properties, one needs to design a proper modeling procedure to simulate the non-isothermal annealing process inside a co-continuous polymer blend. A proper theoretical model is needed to describe shear viscosity as a function of temperature. One possible choice for shear viscosity function is the Cross-WLF equation. This equation considers not only the temperature dependency but also the shear rate and pressure dependency of shear viscosity, shown in Eq.7.27~ Eq.7.30.

$$\eta(\overset{\bullet}{\gamma},\text{T,P}) = \frac{\eta_0(\text{T,P})}{1+(\eta_0\,\overset{\bullet}{\gamma}/\tau)^{1-n}} \qquad (7.27)$$

$$\eta_0(T,P) = D_1 \exp[-A_1(T-T^*)/(A_2+T-T^*)] \qquad (7.28)$$

$$A_2 = A_2^* + PD_3 \qquad (7.29)$$

$$T^* = D_2 + PD_3 \qquad (7.30)$$

The seven coefficients employed in the Cross-WLF equation are n, τ, D_1, D_2, D_3, A_1, A_2^*. These coefficients can be determined by fitting experimental data. As pressures in normal annealing processes are finite, the pressure dependency of shear viscosity is negligible. For this reason, the coefficient D_3 in the Cross-WLF equation, in most cases, is set to zero. After D_3 is set to zero, if the D_2 is chosen to be the glass transition temperature of a material, A_1 and A_2^* will have values close to 17.4 and 51.6 as recommended in the original work of Williams, Landel, and Ferry [17]. The rest of the coefficients can be obtained by fitting experimentally measured flow curves (shear viscosity .vs. shear rate curves).

After the construction of shear viscosity function, the next thing needs to be addressed is the prediction of temperature distribution. Since a well-defined temperature field is required for the formation of a particular gradient porous structure, the thermal boundary conditions which determine the formation of the required temperature distribution need to be precisely controlled. In this study, the steady state

temperature distribution was calculated correspond to a set of pre-determined thermal

boundary conditions. In the calculation, the thermal conductivities of both components

were set to be equal and the effect of interface was ignored. Typical results of 1D and

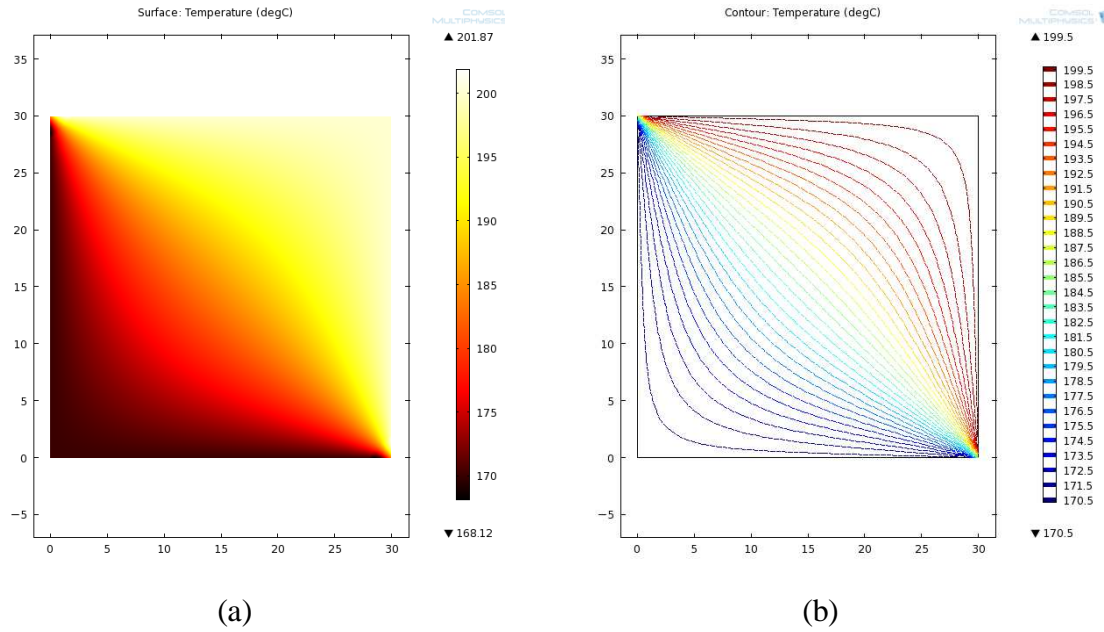2D temperature gradients were calculated and presented in Fig. 7.9 and Fig. 7.10.
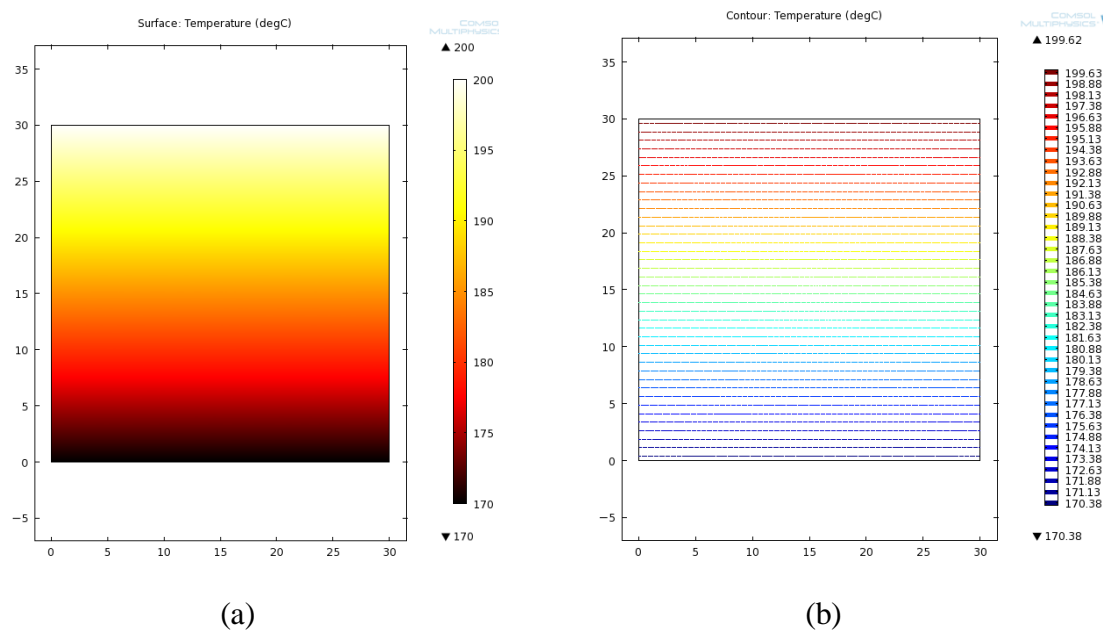
Figure. 7.9: Steady state 1D temperature gradient with top edge at 200 ℃ and bottom edge at 170 ℃: (a) temperature distribution in color scale format; (b) isothermal line plot of the temperature distribution.

Figure. 7.10: Steady state 2D temperature gradient with top & right edges at 200 °C and bottom & left edges at 170 °C: (a) temperature distribution in color scale format; (b) isothermal line plot of the temperature distribution.

For the 1D case, the temperature distribution is simple and the necessity for numerical simulation is not so obvious. However, as the complexity of the thermal boundary increases, the prediction of temperature distribution becomes more and more difficult. For instance, the temperature distribution for the 2D case already appears complex, even though the thermal boundaries are symmetric. Following this, the temperature distribution can become as complex as the one shown in Fig. 7.11.

(a)	(b)
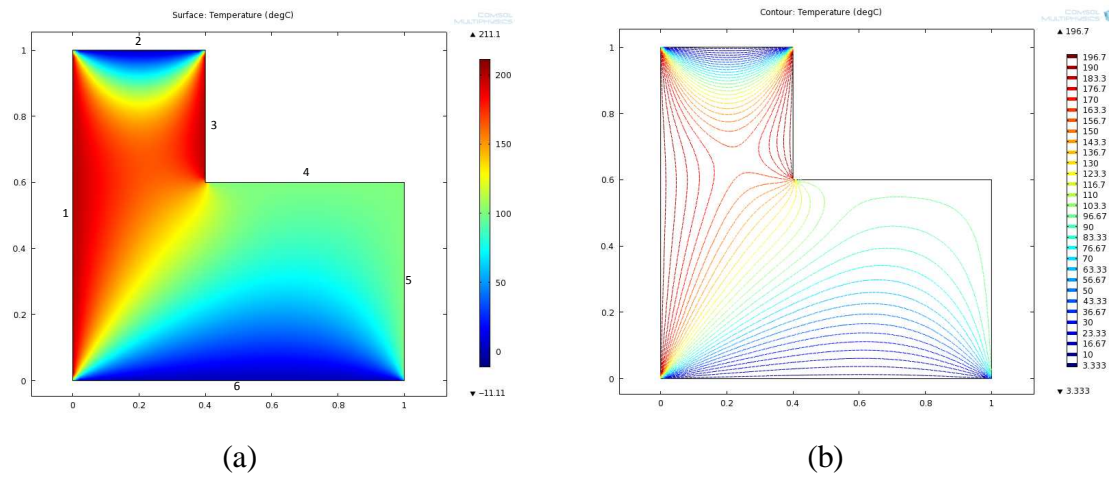
Figure. 7.11: Steady state temperature distribution with edge 1 & 3 at 200 ℃, edge 2 & 6 at 0 ℃, and edge 4 & 5 at 100 ℃: (a) temperature distribution in color scale format; (b) isothermal line plot of the temperature distribution.

The predicted temperature field can be applied as the input variable to calculate the viscosity distribution. This information can then be fed into the phase field theory to predict the phase coarsening rate distribution. As cases studies, phase structures, similar to these presented in Fig.3.6 (a) and Fig. 3.7, were generated using approximated coarsening rate distributions of x^2 and x^2+y^2 respectively, shown in Fig. 7.12 and Fig. 7.13.
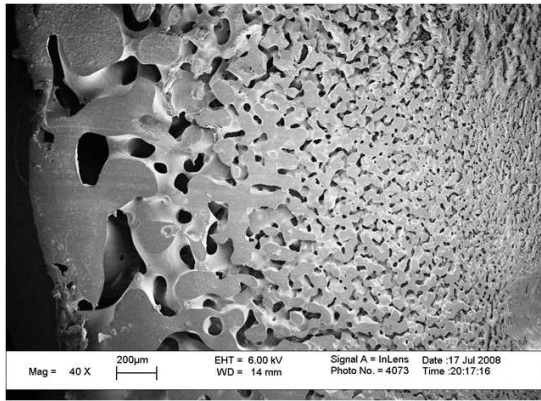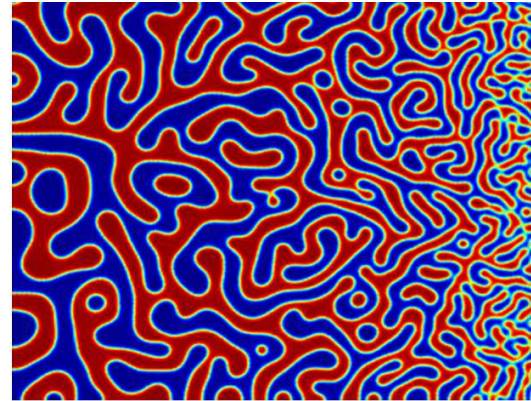
Figure. 7.12: Phase structure of a 1D gradient porous structure: (a) SEM image; (b) simulated phase morphology.
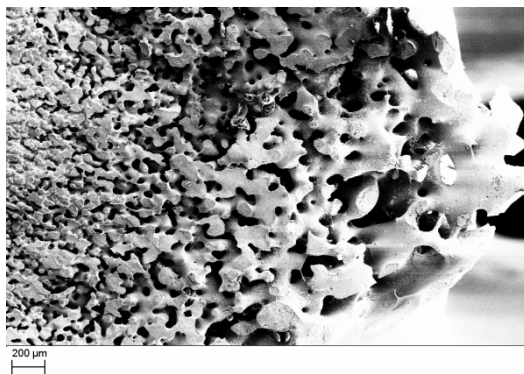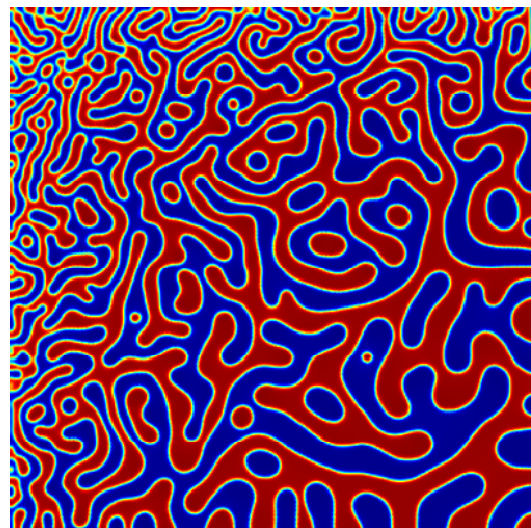
Figure. 7.13: Phase structure of a 2D gradient porous structure: (a) SEM image; (b) simulated phase morphology.

7.3 References

1. Lopez-Barron CR, Macosko CW, Characterizing Interface Shape Evolution in Immiscible Polymer Blends via 3D Image Analysis, *Langmuir*, 25(16), 9392-9404, 2009.

2. Li JM, Ma PL, Favis BD, The Role of the Blend Interface Type on Morphology in Cocontinuous Polymer Blends, Macromolecules, 35, 2005-2016, 2002.

3. Yuan ZH, Favis BD, Influence of the Efficacy of Interfacial Modification on the Coarsening of Cocontinuous PS/HDPE Blends During Quiescent Annealing, *J. Polym. Sci. Part B: Polym Phys*, 44, 711-721, 2006.

4. Pyun A, Bell JR, Won KH, Weon BM, Seol SK, Je JH, Macosko CW, Synchrotron X-ray Microtomography for 3D Imaging of Polymer Blends, *Macromolecules*, 40, 2029-2035, 2007.

5. L. P. McMaster, Adv. Chem., 1975, 142, 43–65.

6. S. Tomotika, Proc. R. Soc. London, Ser. A, 1935, 150, 322–337.

7. E. D. Siggia, Phys. Rev. A: At., Mol., Opt. Phys., 1979, 20, 595–605.

8. Lopez-Barron, C.R. and C.W. Macosko, Characterizing Interface Shape Evolution in Immiscible Polymer Blends via 3D Image Analysis. Langmuir, 2009. 25(16): p. 9392-9404.

9. Pyun, A., et al., Synchrotron X-ray microtomography for 3D imaging of polymer blends. Macromolecules, 2007. 40(6): p. 2029-2035.

10. E. Scholten, L. M. C. Sagis and E. van der Linden, J. Phys. Chem. B, 2004, 108, 12164–12169.

11. E. Scholten, L. M. C. Sagis and E. van der Linden, Macromolecules, 2005, 38, 3515–3518.

12. W. Helfrich, Z Naturforsch, 1973, 28, 693–703.

13. Lopez-Barron, C.R. and C.W. Macosko, A new model for the coarsening of cocontinuous morphologies. Soft Matter, 2010. 6(12): p. 2637-2647.

14. E. Olsson and G. Kreiss, A conservative level set method for two phase flow, J. Comput. Phys., 210, 225–246, 2005.

15. P. Yue, C. Zhou, J.J. Feng, C.F. Ollivier-Gooch, and H.H. Hu, Phase-field simulations of interfacial dynamics in viscoelastic fluids using finite elements with adaptive meshing, J. Comp. Phys., 219, 47–67, 2006.

16. User's guide of Comsol.

17. M.L. Williams, R.F. Landel, J.D. Ferry, J. Amer. Chem. Soc., 77, 3701, 1955.

CHAPTER 8

CONCLUSIONS AND RECOMMENDATIONS

In this thesis, several fabrication techniques for generating porous structures using co-continuous polymer blend were developed and the underlying mechanisms were explored.

8.1   Conclusions

8.1.1 Generation of gradient porous structures

Through designing proper thermal boundary, various gradient porous structures were generated from co-continuous polymer blends. The possibility of utilizing rheological characterization and CFD (computational fluid dynamics) to create gradient porous structures with precisely controlled pore size distributions were investigated. Qualitatively matches between experimental results and CFD results were realized in two cases studies where 1D and 2D gradient porous structures were produced. In addition to these two morphologies, a gradient porous structure with an axisymmetric pore size distribution was developed experimentally to demonstrate the versatility of this fabrication technique. Following this design protocol, one can create porous structures with more complex pore size distributions.

8.1.2 Geometrical confining effects in compression molding of porous material

From this research, it was found that the compression molding of co-continuous polymer blend not only giving the material a desired geometry but also having influence on the structure of this material. The no-slip wall effect imposed by the mold cavity gave rise to a pore size gradient perpendicular to the mold inner surface with smaller coarsening rate when the location was closer towards the mold cavity. When the size of the size of the mold feature was close to the phase size of the co-continuous polymer blend, a strong geometrical confining effect started to reveal and strongly influence the phase coarsening process. As a result, the material under confinement began to align its phase structure in direction(s) where least geometrical confinement existed. In addition to the geometrical confinement, the chemical property of the mold inner surfaces were able to serve as a localized chemical potential which selectively attract one component of the blend and resulted in an extra concentration gradient near the mold cavity. This phenomenon was later applied to produce porous devices with either a fully open pore surface or completely dense surface.

8.1.3 Composites with interconnected porous structures and high nanoparticle loading

With the purpose of improving the bioactivity of the fabricated porous material, HA (hydroxyapatite) nanoparticle was added into the PLA/PS co-continuous polymer blend to make a porous nano-composite. A special two-step fabrication technique was developed and investigated for resolving the pore blockage caused by the added HA nanoparticles. A PLA/PS/HA 40/40/20 wt% blend was prepared by one-step

feeding and mixing procedure which gave the required initial co-continuous phase morphology. The blockage caused by HA nanoparticle was tackled by applying a small-strain oscillatory movement to the prepared mixture in which HA nanoparticle uniformly distributed in both PLA and PS phases. This oscillatory movement was experimentally confirmed to be able to greatly accelerate the migration of the nanoparticle towards the PLA phase and resulted a porous structure with interconnected open pores. The migration kinetics was studied using Cox-Merz rule and Einstein diffusion theory. Consistence between experimental result and theoretical prediction was found for this nano-composite system.

8.1.4 Creation of micropatterned porous structures

A new molding technique capable of creating precise micropatterned porous structures was developed and examined. In this new technique, hot embossing and in-mold quiescent annealing were applied successively to a PLA/PS co-continuous polymer blend to not only pattern the blend into well-defined geometries but also provide the desired pore size distribution of the inner microporous structures. The effectiveness of this molding protocol was confirmed by experimental results in which devices with different micropatterns, average pore sizes, pore size distributions, and pore alignments were created. For cases where fully open surface is required, a criterion for choosing a proper molding condition was provided through a comprehensive parametric study.

8.1.5 Theoretical study

A CAE (computer assisted engineering) procedure for helping the creation of high quality gradient porous structures was investigated. To study the phase coarsening kinetics of a co-continuous polymer blend, CFD (computational fluid dynamics) was used to simulate the quiescent annealing process. On a simplified model system, the phase coarsening rate was calculated from the simulation results and compared with experimental data. Qualitative matches between these two types of results were observed. Following that, 1D and 2D gradient porous structures were generated using numerical simulation.

8.2 Recommendations

In this PhD work, the possibility of utilizing different types of boundary conditions to create novel microporous structures from co-continuous polymer blend was investigated. Moreover, CFD (computational fluid dynamics) modeling was applied to predict phase structures generated by two different thermal boundaries. In the aforementioned researching efforts, several major assumptions were made to facilitate the analysis of data related to the complex phase evolution process. In the future, a comprehensive study about the potential influences of these assumptions is needed in order to further improve these newly developed techniques. With no intention to provide detail research plans, the author listed several potential topics for future study.

First, the influence of interfacial properties to the coarsening kinetics should be explored. In current study, the interfaces between the two components inside a co-continuous polymer blend were assumed to undergo affine deformation for the whole coarsening process. Furthermore, it was assumed that slippage at the interface did not happen. However, these assumptions have not been fully verified for co-continuous blend system. Studies on related topics will help to address many fundamental issues involving co-continuous polymer blend.

Second, the influence from mold cavity deserves a focused study in the future. The geometrical confinement effect and the chemical affinity effect were investigated in this study. However, it is obvious that the existence of mold cavity changes the polymer/polymer interface to a three-phase line similar as the one in contact angle measurement. The details about the movement of this line under uneven pressures, to

the best of the author's knowledge, have not been addressed in previous literature. An in-depth study on this topic will facilitate the understanding about the deformation behavior of co-continuous polymer blend.

Last but not least, the influence of incorporated nanoparticles to the rheological properties of resulted nano-composite should be explored. The influence of nanoparticles is not difficult to understand, considering its large surface-volume ratio. The tendency for these particles to selectively stay either inside one component or at the interface is already reported in several literatures. Up to now, there is no conclusive explanation about this unusual phenomenon. A study on this topic will contribute to our understanding about this type of nano-composite and extend practical applications.
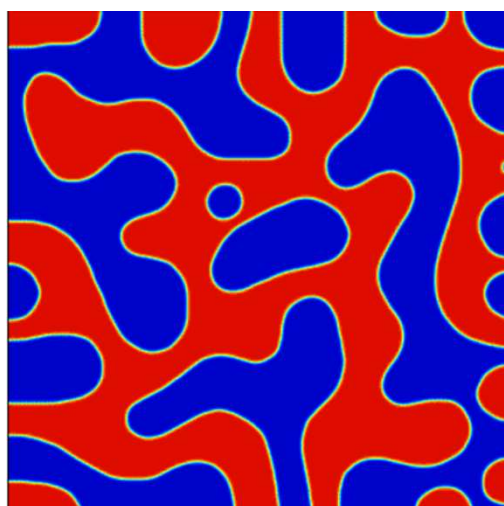
Appendix
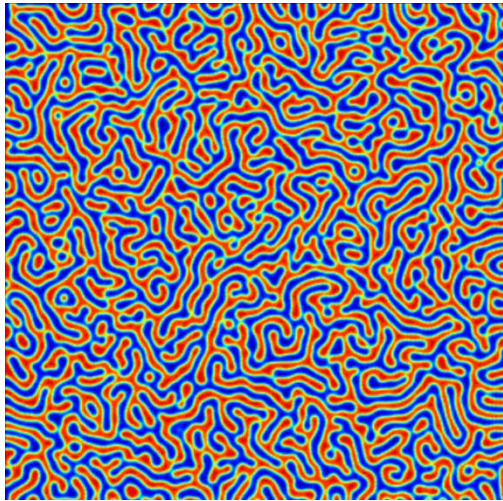
(a)

(b)

(c)

(d)

(e)

(f)

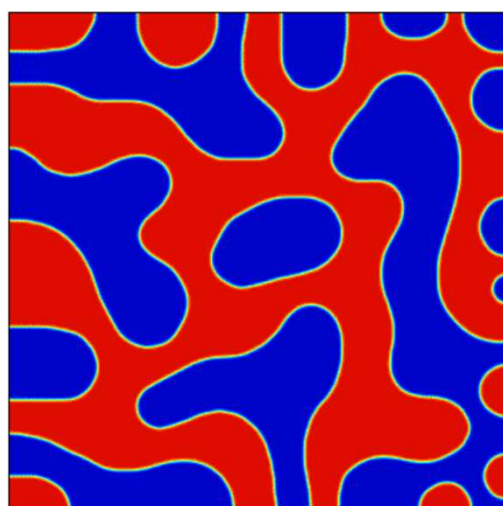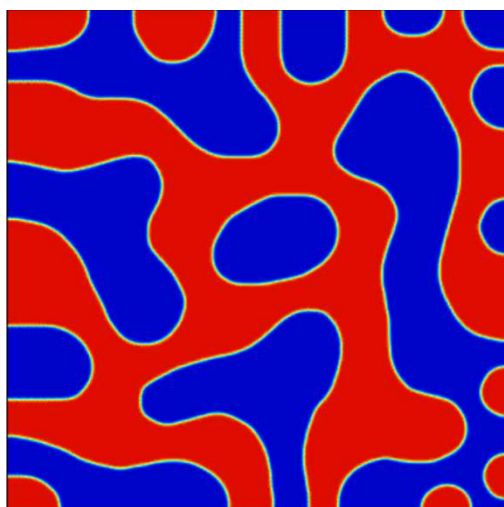(g)

(h)

(i)

(j)

(k)
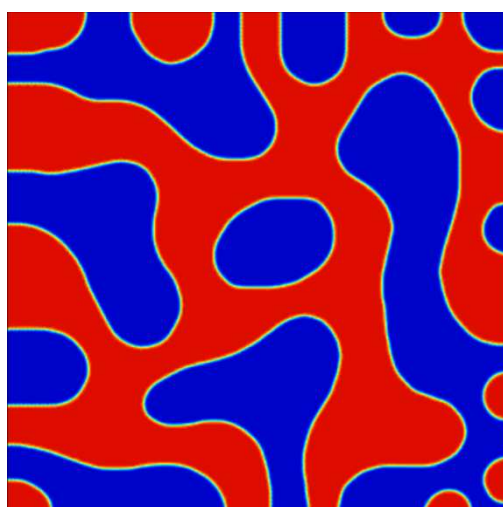

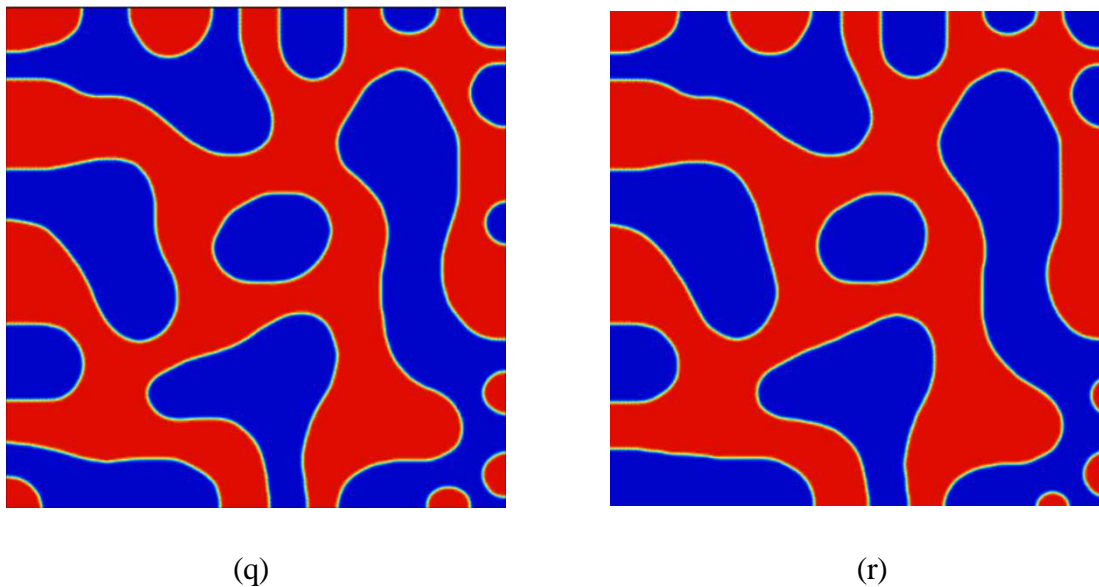(l)

(m)

(n)

(o)

(p)

(q)

(r)
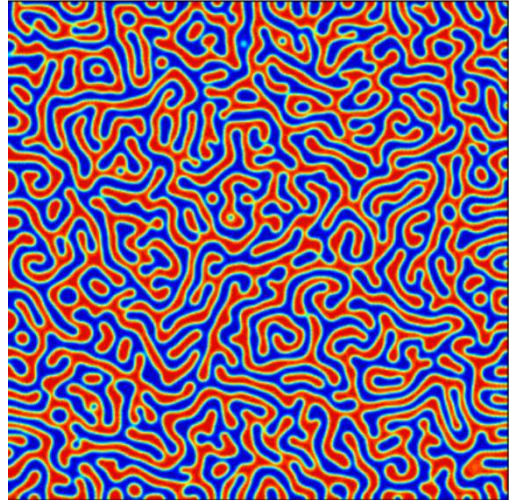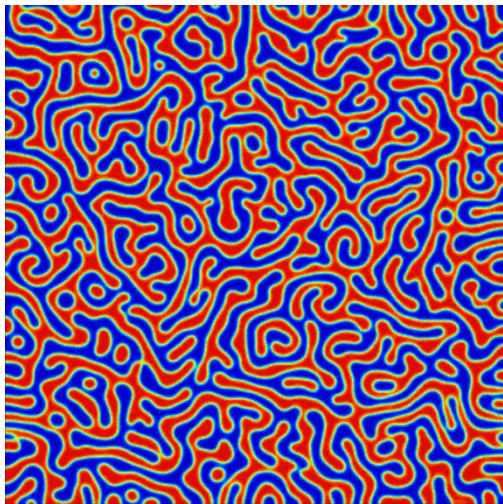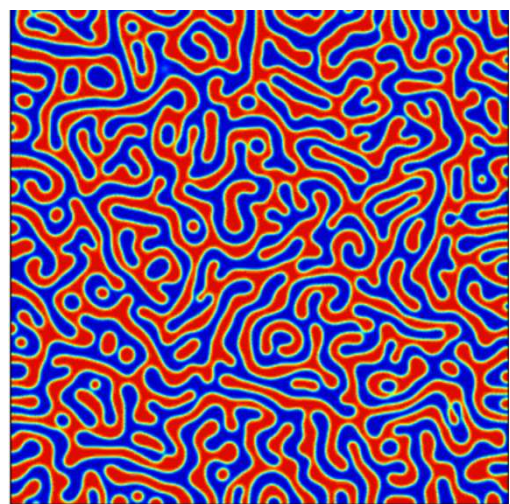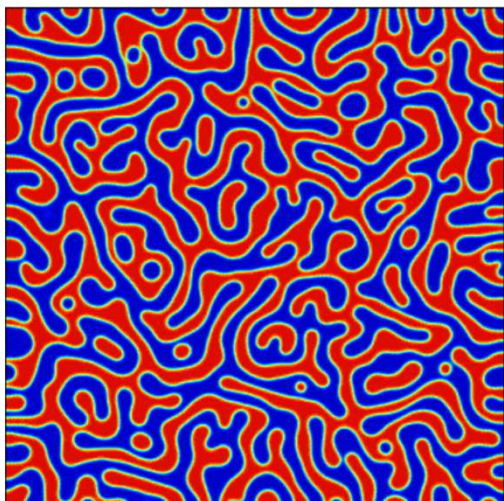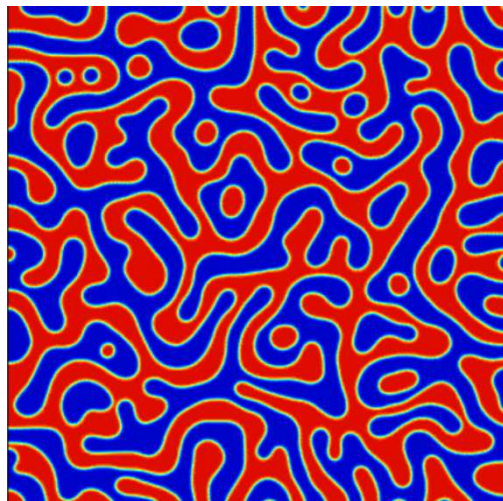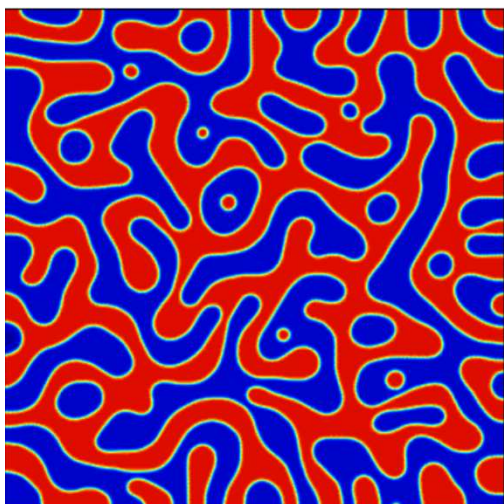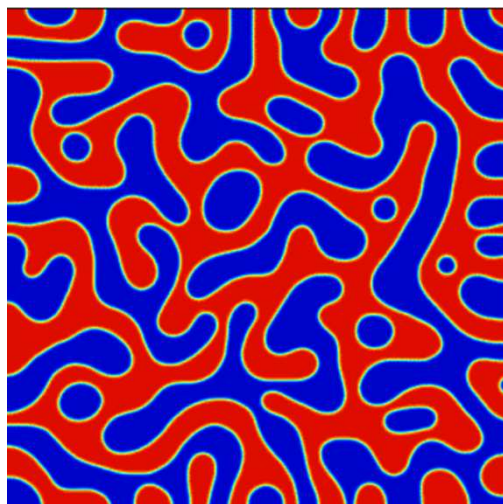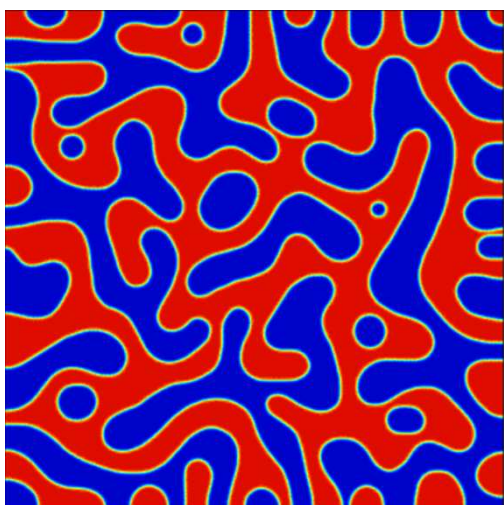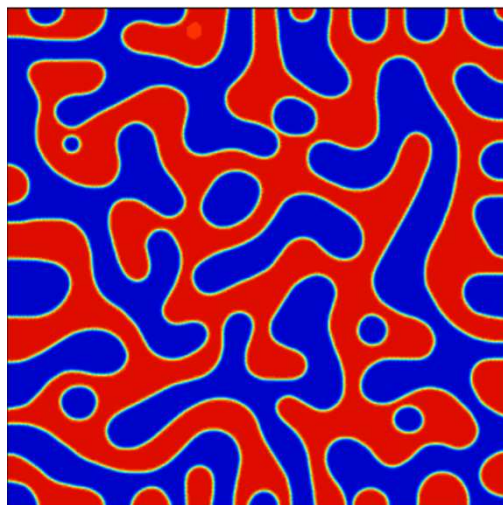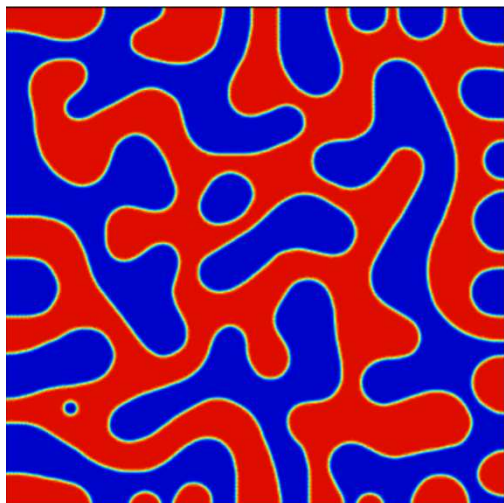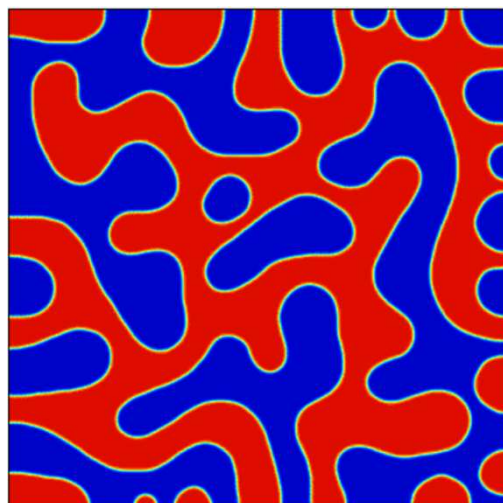
Figure. A.1: Phase morphology of a 2D co-continuous polymer blend undergoing isothermal annealing for different times. The red region is polymer A and the blue region is polymer B. The total image size is 0.5 mm * 0.5 mm. The individual annealing times are: (a) 0.5; (b) 1; (c) 1.5; (d) 2; (e) 4; (f)10; (g) 20; (h) 30; (i) 40; (j) 50; (k) 90; (l) 120; (m) 180; (n) 250; (o) 300; (p) 350; (q) 400; (r) 500 seconds.